



THESIS

STRUCTURES, DYNAMICS AND CHEMICAL REACTIONS OF INDUSTRIAL CATALYSTS (METAL OXIDES AND NANOPOROUS MATERIALS)

SOMKIAT NOKBIN

GRADUATE SCHOOL, KASETSART UNIVERSITY

2006



THESIS APPROVAL
GRADUATE SCHOOL, KASSETSART UNIVERSITY

Doctor of Philosophy (Chemistry)

DEGREE

Physical Chemistry

FIELD

Chemistry

DEPARTMENT

TITLE: Structures, Dynamics and Chemical Reactions of Industrial Catalysts
(Metal oxides and Nanoporous Materials)

NAME: Mr. Somkiat Nokbin

THIS THESIS HAS BEEN ACCEPTED BY

Jumras Limtrakul

THESIS ADVISOR

(Professor Jumras Limtrakul, Ph.D.)

Kersti Hermansson

CO-THESIS ADVISOR

(Professor Kersti Hermansson, Ph.D.)

Supa Hannongbua

COMMITTEE MEMBER

(Associate Professor Supa Hannongbua, Dr.rer.nat.)

Pensri Bunsawansong

COMMITTEE MEMBER

(Miss Pensri Bunsawansong, Ph.D.)

Yerry Mahatumaratana

DEPARTMENT HEAD

(Assistant Professor Yerry Mahatumaratana, B.Sc.)

APPROVED BY THE GRADUATE SCHOOL ON 27 March 2006

Vinai Artkongharn

DEAN

(Associate Professor Vinai Artkongharn, M.A.)

THESIS

STRUCTURES, DYNAMICS AND CHEMICAL REACTIONS OF INDUSTRIAL CATALYSTS (METAL OXIDES AND NANOPOROUS MATERIALS)

SOMKIAT NOKBIN

**A Thesis Submitted in Partial Fulfillment of
the Requirements for the Degree of
Doctor of Philosophy (Chemistry)
Graduate School, Kasetsart University
2006**

ISBN 974-16-1212-5

Somkiat Nokbin 2006: Structures, Dynamics and Chemical Reactions of Industrial Catalysts (Metal oxides and Nanoporous Materials). Doctor of Philosophy (Chemistry), Major Field: Physical Chemistry, Department of Chemistry. Thesis Advisors: Professor Jumras Limtrakul, Ph.D. and Professor Kersti Hermansson, Ph.D. 119 pages.
ISBN 974-16-1212-5

The structures, dynamics and chemical reactions of Faujasite/(H₂O)_n and Faujasite/(CH₃OH)_n systems have been studied by means of finite and embedded cluster approaches in the framework of the density functional theory. For Faujasite/(H₂O)_n system, it is found that no proton transfer occurs from zeolite to water until there are at least four water molecules in the system. Inclusion of the Madelung potential was found to increase the acidity of the Brønsted acid site, yielding the complete proton transfer from zeolite to H₂O in the presence of the third promoted water, ZO(H₃O⁺)(H₂O)₂. As for a methanol monomer system, the hydrogen bonded complex is found to be the stable structure in the finite cluster model. The protonated form, ZO(CH₃OH₂)⁺ can be found when the Madelung potential is taken into account.

The interactions of Rh/MgO(001) and Rh/CeO₂ systems have been carried out by means of the DFT periodic planewave calculations. Owing to the importance of such materials, a closer examination of their structural, chemical, electronic, and surface properties have been examined to understand their surface chemistry. The adsorption site dependence as well as the coverage dependence has been demonstrated. It is found that the most stable adsorption site is the O site for both metal oxide substrates. At the high coverage, the metal-metal interactions within the Rh overlayer give the largest contribution to the stabilization of the Rh/metal oxide interface, giving a rise of adsorption energy with the increasing surface coverage, while, naturally, the Rh-oxide interaction dominates at low coverage. In order to clarify the electronic properties of such systems, the density of states (DOS), electron density difference plot, spin density and the electron localization function (ELF) are presented.

Somkiat

Student's signature

Jumras Limtrakul

Kersti Hermansson

14 / 3 / 06

Thesis Advisor's signatures

ACKNOWLEDGMENTS

First and foremost, I would like to thank my advisor, Professor Jumras Limtrakul, for his supervision, valuable guidance, support and for being patient for all the aspects during these years. Professor Kersti Hermansson, my supervisor in Sweden, is gratefully acknowledged for her advise, encouragement and fruitful discussions on various topics.

I would also like to thank my Ph.D. committees, Associate Professor Supa Hannongbua, Dr. Pensri Bunsawansong and the representative of Graduate School , Dr. Teerasak Veerapasong, for their useful comments and suggestions to fulfill this thesis work.

Professor Michael Probst is appreciatively acknowledged for introducing me to Sweden and for being my scientific guru. Dr. Zongxian Yang and Dr. Christopher Castleton are thanked for their valuable discussions.

The financial supports from the Royal Golden Jubilee Ph.D. fellowship the Thailand Research Fund (TRF), the Development and Promotion of Science and Technology Talents Project (DPST), the Swedish Foundation for International Cooperation in Research and Higher Education, (STINT) and the Swedish Research Council (VR) are hereby acknowledged.

The Laboratory for Computational and Applied Chemistry (LCAC) as well as the Postgraduate Education and Research Program in Petroleum and Petrochemical Technology at the Department of Chemistry, Kasetsart University (MUA-ADB) and the theoretical group at Materials Chemistry department, Uppsala University are gratefully acknowledged for research facilities.

I would like to thank all of my friends and colleagues at LCAC and KU, especially Umaporn Janbang, Pipat Khongpracha and Pornsak Methavichit, for their help, friendship and company during these years. My colleagues at the theoretical group, Materials Chemistry Department, Uppsala University are also acknowledged. Moreover, Pikul Jiravanichpaisal, Atcharawon Gardchareon, Victor Stanciu, Sami Amira and Grzegorz Gajewski are thanked for their friendship during my stay in Sweden.

Finally, I would like to thank my parents, grandmothers, grandfathers and relatives for their endless love, support and encouragement.

Somkiat Nokbin

January, 2006

TABLE OF CONTENTS

	Page
TABLE OF CONTENTS	i
LIST OF TABLES	iv
LIST OF FIGURES	vi
ABBREVIATIONS	xii
INTRODUCTION	1
LITERATURE REVIEW	5
Catalysis in Zeolites and Nanostructured Materials:	
Aluminosilicate systems	5
Catalysis on surfaces: Metal oxide systems	9
METHODS OF CALCULATIONS	16
Density functional theory (DFT)	16
Models and methodologies	18
Finite cluster and Embedded cluster approaches	18
Faujasite/(H ₂ O) _n systems	20
Faujasite/(CH ₃ OH) _n systems	22
Periodic plane-wave approach	24
Rh/MgO(001) systems	24
Rh/CeO ₂ systems	27
RESULTS AND DISCUSSION	31
Chapter I. High coverage effect on proton transfer of	
Faujasite/water system	31
One and two water molecules per acid site	31
Three and four water molecules per acid site	39
Conclusions	40
Chapter II. Methanol adsorption on faujasitic petrochemical	
catalysts	41
Model dependence	41
Cluster size effects	41

TABLE OF CONTENTS (cont'd)

	Page
Effects of the Madelung potential	42
Effects of basis set	45
Mode of adsorption	45
Low coverage	46
High coverage	49
Vibrational frequency analysis	50
Conclusions	54
Chapter III. Structural and Electronic Properties of Rh/MgO(001)	
Systems	56
Bulk MgO and bulk Rh - reference systems	56
The clean MgO(001) surface - a reference system	59
The Rh/MgO(001) systems	62
Structure	62
Adsorption energy	64
Electron density difference	67
The electron localization function (ELF)	69
Density of states (DOS)	71
The spin density and the magnetization	75
Conclusions	79
Chapter IV. Interactions of Rhodium on (110) and (111) Surfaces of CeO ₂	80
Bulk system	80
Clean surfaces	82
Surface energy	82
Structural relaxation	82
Rh/CeO ₂ interface systems	85
Adsorption energy	85
Growth modes	92

TABLE OF CONTENTS (cont'd)

	Page
Electron density difference	93
The electron localization function (ELF)	95
CO/Rh/CeO ₂ (111) and NO/Rh/CeO ₂ (111): preliminary results	97
Conclusions	100
CONCLUDING REMARKS	101
LITERATURE CITED	102
CURRICULUM VITAE	116

LIST OF TABLES

Table		Page
1	Structural parameters of the Faujasite/(H ₂ O) _n systems, n = 1, 2.	32
2	Structural parameters of the Faujasite/(H ₂ O) _n systems, n = 3, 4.	33
3	Adsorption energies of water clusters on Faujasite zeolite (kcal/mol).	34
4	Structural parameters of methanol adsorption in Faujasite.	43
5	Adsorption energies of methanol cluster in Faujasite zeolite (kcal/mol).	44
6	Vibrational frequencies (cm ⁻¹) of the chemisorbed adsorption modes.	52
7	Vibrational frequencies (cm ⁻¹) of the physisorbed adsorption modes.	53
8	Interaction energies per Rh atom (in eV) and vertical Rh-surface distance (in Å) for the optimized Rh/MgO(001) system at different Rh coverages. The adhesion energy (E_{adh}) is the energy gained when the pre-formed Rh layer adheres to the MgO slab and the adsorption energy (E_{ads}) also includes the energy gained when the Rh-layer is formed from Rh atoms (E_{form}).	63
9	Total and projected spin magnetic moments (in μ_B) for the Rh/MgO(001) system for different Rh coverages at the optimized Rh-surface distances. The values for the spin magnetic moments given here were calculated with spheres of the standard Wigner-Seitz spheres with radii of 1.402, 1.058 and 0.820 Å for Rh, Mg and O, respectively.	78
10	The calculated lattice constants and the surface energies for (110) and (111) ceria surfaces. All presented values are taken from the CeO ₂ (110) <i>p</i> (1×1) and CeO ₂ (111) <i>p</i> (1×1) models.	81

LIST OF TABLES (cont'd)

Table		Page
11	The optimized Rh-surface distances and the interaction energies for Rh/CeO ₂ systems.	86
12	The optimized Rh-surface distances and the interaction energies for Rh/CeO ₂ systems as the function of coverages. All calculations performed here are simulated for the Os adsorption site.	91
13	The selected structural parameters and the corresponding adsorption energies for the CO/Rh/CeO ₂ (111) and NO/Rh/CeO ₂ (111) systems at Os for the 1/2 ML Rh coverage.	98

LIST OF FIGURES

Figure		Page
1	The illustrative Faujasite zeolite structure model: (a) a unit cell of Faujasite and (b) the 11T cluster fragment which is cut off from the Faujasite unit cell.	2
2	The bulk structures of (a) MgO, (b) CeO ₂ and (c) Rhodium systems.	3
3	The embedded cluster models created from the SCREEP approach.	19
4	Faujasite cluster model: a) 3T and b) 3T Embedded clusters.	21
5	Faujasite cluster model: a) 5T, b) 7T and c) 7T Embedded clusters.	23
6	The surface coverage definitions for the Rh/MgO(001) systems. In these figures the Rh atoms were placed on top of the surface oxygen. The square box represents the sizes of the supercell used in this study: (a) and (b), the 1x1 crystallographic unit cells are selected for 1 and 1/2 ML coverage, respectively, (c) the 2x2 crystallographic unit cell is used for 1/8 ML coverage. The P1, P2 and P3 are the selected perpendicular planes to use for illustrating the total charge density and the electron density difference plots.	25
7	The 3-dimensional supercell for Rh/MgO(001) systems for: (a) 1/8 ML, (b) 1/2 and 1 ML coverages.	26
8	The supercell used in the calculations for CeO ₂ (110) systems: (a) $p(1 \times 1)$ and (b) $p(1 \times 2)$. The corresponding top view of the topmost surface is also shown.	28
9	The supercell used in the calculations for CeO ₂ (111) systems: (a) $p(1 \times 1)$ and (b) $p(\sqrt{3} \times 1)$. The corresponding top view of the topmost surface is also shown.	29

LIST OF FIGURES (cont'd)

Figure		Page
10	The coverage definition for 1/2 and 1 ML Rh coverage on (a) 1/2 ML CeO ₂ (110) <i>p</i> (1×2), (b) 1 ML CeO ₂ (110) <i>p</i> (1×2), (c) 1/2 ML CeO ₂ (111) <i>p</i> ($\sqrt{3}\times 1$) and (d) 1 ML CeO ₂ (111) <i>p</i> ($\sqrt{3}\times 1$) systems. The filled color triangles are represented Rh atoms.	30
11	(a) Cluster and (b) Embedded cluster models of the Faujasite/H ₂ O system. All values are given in angstroms.	35
12	(a) Cluster and (b) Embedded cluster models of the Faujasite/(H ₂ O) ₂ system. All values are given in angstroms.	36
13	(a) Cluster and (b) Embedded cluster models of the Faujasite/(H ₂ O) ₃ system. All values are given in angstroms.	37
14	Modes of adsorption: a) chemisorbed, and b) physisorbed complexes. Values in parenthesis are represented the configurations obtained from bare cluster calculation.	47
15	Methanol adsorption in embedded 7T-FAU/[CH ₃ OH] ₂ system. Values in parenthesis are represented the configurations obtained from bare cluster calculation.	48
16	The density of states for the MgO bulk system; TDOS of MgO (a) and PDOS of O (b) and Mg (c).	57
17	TDOS and PDOS of Rh bulk. The <i>s</i> , <i>p</i> and <i>d</i> states of Rh are shown in (a), (b) and (c), respectively.	58
18	The structural relaxations for the clean surface of MgO(001) and the Rh/MgO(001) systems: (a) ideal clean surface, (b) optimized clean surface, (c) 1 ML Rh/MgO(001) for the O site and (d) 1 ML Rh/MgO(001) for the Mg site.	60

LIST OF FIGURES (cont'd)

Figure		Page
19	TDOS and LPDOS of the 8-layer MgO(001) slab. White and black areas represent LPDOS of O and Mg, respectively. The TDOS for bulk MgO is included for reference. “S”, “S-1”, ..., and “S-3” represent the surface layer, the sub-surface layer, ..., and the center layer of the slab, respectively.	61
20	An interaction energetic chart for the Rh/MgO(001) interface system for the O adsorption site as a function of coverages.	66
21	Electron density difference plots for the optimized interface system when Rh binds over surface O for difference coverages. Solid and dashed contour lines represent electron excess and electron loss, respectively. The contour lines start at $\pm 0.0005 \text{ e/a.u.}^3$, increasing by a factor of $10^{0.2}$ for every contour line, i.e. the contours are at $\pm 0.0005, \pm 0.0008, \pm 0.0012, \pm 0.0020, \pm 0.0031, \pm 0.0050, \dots \text{ e/a.u.}^3$	68
22	Electron density difference plots for the optimized interface system when Rh binds over Mg and the hollow site at difference coverages. Contour intervals are the same as in Figure 21.	68
23	The ELF plots for the optimized interface system when the Rh binds over O, Mg and the hollow sites at the 1/2 and 1ML coverages. The ELF contours represent values between 0 to 1 (see text) and the increment for every contour line is 0.05 e/a.u.^3 .	70
24	DOS for bulk Rh and different geometries (related to different coverages) of isolated Rh ML systems. The solid and dashed lines represent the majority and minority spin components, respectively.	72

LIST OF FIGURES (cont'd)

Figure		Page
25	TDOS and LPDOS for Rh/MgO at the O adsorption site with difference coverages of Rh. Solid and dashed lines represent the majority and minority spin components, respectively. In (c) and (i), the light color line shows the $2p$ states of surface oxygen without Rh bound to it.	73
26	TDOS for Rh/MgO at the Mg adsorption site with difference coverages of Rh. Solid and dashed lines represent the majority and minority spin components, respectively.	74
27	The relative energy as a function of the magnetization of Rh/MgO(001) at the O site for 1 ML coverage, a non magnetic state is defined by a zero energetic curve.	76
28	Total magnetization of the Rh/MgO system as a function of the interlayer distance of the Rh overlayer and surface for different adsorption sites of 1ML coverage.	77
29	The illustration of localized and itinerant magnetism as well as non-magnetic regions as a function of the $d-d$ and $d-p$ interaction strength.	77
30	The total (TDOS) and partial (PDOS) densities of states of bulk CeO ₂ . In the PDOS panels, solid and dashed curves represent PDOS of Ce and O, respectively. The Fermi energy is shown by the vertical dotted line.	80
31	Inter-planar displacement of CeO ₂ (110) of (a) $p(1\times 1)$ and (b) $p(1\times 2)$ supercells. The outward and inward displacements compared to bulk are represented by positive and negative values, respectively.	83

LIST OF FIGURES (cont'd)

Figure		Page
32	Inter-planar displacement of CeO ₂ (111): (a) $p(1\times 1)$ and (b) $p(\sqrt{3}\times 1)$ supercells. The outward and inward displacements compared to bulk are represented by positive and negative values, respectively.	84
33	Inter-planar displacement for Rh/CeO ₂ (110) $p(1\times 2)$ system. (a) O _s and (b) Ce adsorption sites. The outward and inward displacements compared to bulk are represented by positive and negative values, respectively.	87
34	Inter-planar displacement for Rh/CeO ₂ (111) $p(\sqrt{3}\times 1)$ system. (a) O _s , (b) Ce and (c) O _{ss} adsorption sites. The outward and inward displacements compared to bulk are represented by positive and negative values, respectively.	88
35	The structural relaxation for Rh/CeO ₂ (111) $p(\sqrt{3}\times 1)$ system. (a) O _s , (b) Ce and (c) O _{ss} adsorption sites.	90
36	Electron density difference plots for the optimized interface system for Rh/CeO ₂ (111) at different coverages and adsorption sites: (a) 1/2 ML O _s , (b) 1 ML O _s , (c) 1 ML Ce and (d) 1 ML O _{ss} . Solid and dashed contour lines represent electron excess and electron loss, respectively. The contour lines start at ± 0.0005 e/a.u. ³ , increasing by a factor of $10^{0.2}$ for every contour line. In each figure, the total charge density is also plotted and shown in the left panel.	94

LIST OF FIGURES (cont'd)

Figure		Page
37	The electron localization function (ELF) plots for the optimized interface system for 1 ML coverage of Rh/CeO ₂ (111) at different adsorption sites: (a) atomic species in the selected cutting plane for the (b) O _s , (c) Ce and (d) O _{ss} adsorption sites. The ELF contours represent values between 0 to 1 (see text, page 69, for ELF definition) and the increment for every contour line is 0.1 e/a.u. ³ .	96
38	The optimized structural geometries for (a) C-bound, (b) O-bound models of CO/Rh/CeO ₂ (111), (c) N-bound and (d) O-bound models of NO/Rh/CeO ₂ (111) systems. All values are given in Å.	99

LIST OF ABBREVIATION

B3LYP	=	Becke's three parameter hybrid functional using the LYP correlation functional
BSSE	=	Basis set superposition error
DFT	=	Density functional theory
DOS	=	Density of states
ELF	=	Electron localization function
FAU	=	Faujasite
FLAPW	=	Full potential linearized augmented-plane-wave
FP-LMTO	=	Full potential linear muffin-tin orbital
GGA	=	Generalized gradient approximation
HF	=	Hartree Fock
IP	=	Ion-pair
LDA	=	Local density approximation
LPDOS	=	Layer-projected density of states
NC	=	Neutral complex
PAW	=	Projector augmented-wave method
PDC	=	Potential derived charges
PDOS	=	Partial density of states
SCREEP	=	Surface Charge Representation of the Electrostatic Embedding Potential
T	=	Tetrahedral
TDOS	=	Total density of states
TWC	=	Three-way-catalyst

STRUCTURES, DYNAMICS AND CHEMICAL REACTIONS OF INDUSTRIAL CATALYSTS (METAL OXIDES AND NANOPOROUS MATERIALS)

INTRODUCTION

Catalysis is one of the key factors in many technologies utilized in modern industry nowadays. Basically, catalysts provide a different pathway for the reaction which has a lower activation energy than before. If a reaction has a low activation energy, its rate tends to be higher. Catalysts can be classified as *homogeneous catalysts* and *heterogeneous catalysts*. Homogeneous catalysts are catalysts that share the same state as the reacting substances while heterogeneous catalysis occurs when the catalyst is in a different state from the reactants.

In this thesis work, two types of heterogeneous catalysis systems were investigated as noted by the “*Catalysis in Zeolites and Nanostructured Materials*” and the “*Catalysis on surfaces*”. The former deals with the aluminosilicate and metallosilicate systems whereas the latter is related to metal oxide systems. The very brief details of such systems are stated below.

Zeolites play vital roles as catalysts and adsorbents, in a large number of major industrial processes due to the combination of their acid-base property and shape selectivity. One of most particular interests in this active research is the adsorption structure of methanol and water with the question of whether these probe molecules are protonated or not at acid zeolite catalysts. In this thesis, the interactions of water and methanol molecules with the specific zeolite, namely Faujasite (Figure 1a), were investigated.

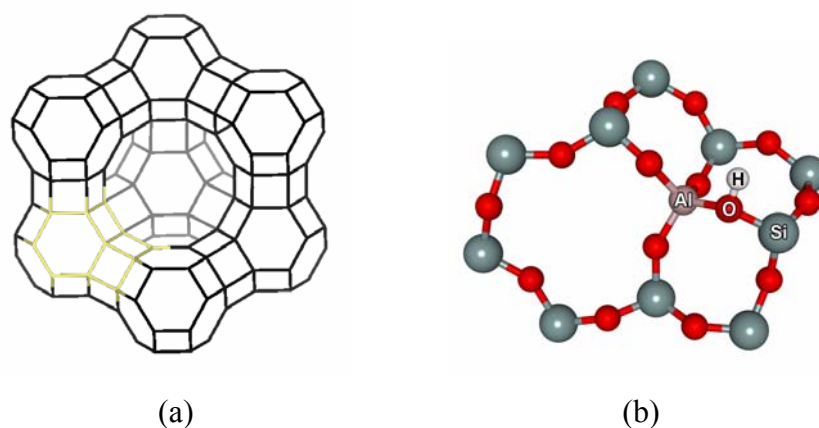
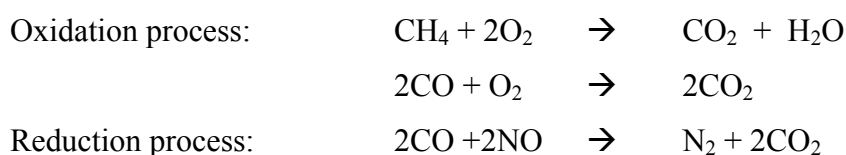


Figure 1 The illustrative Faujasite zeolite structure model: (a) a unit cell of Faujasite and (b) the 11T cluster fragment which is cut off from the Faujasite unit cell.

Beside the zeolite catalysts, metal oxides – in the form of crystals, nanomaterials, thin films or surfaces – also play a vital role in many technological applications. Nowadays, most of the catalytic converter technology employs three-way-catalyst (TWC) to catalyze the simultaneous conversions of hydrocarbons, CO and NO_x presented in the exhaust into H₂O, CO₂ and N₂. Such conversions are dealt with oxidation and reduction processes that can be seen as



It has been found that the reduction process of TWCs is relevant by the Rh/CeO₂ support because one of the principle steps in the catalytic reduction of NO_x over Rh is the dissociation of the N–O bond. The dissociation of NO is enhanced when the Rh is supported on reduced CeO_x. Unfortunately, most of the available results have been obtained experimentally so far and the mechanism of such reactions is unclear, however.

Since the activity and reactivity of metal-metal oxide catalysts depend upon the nature of both the metal and the metal oxide support and on their interplay. The studies of different metal/metal-oxides interaction are abundant in the literature and among them, MgO seems to play a very important role as a supported metal-oxide in many heterogeneous catalysts due to the simplicity of structure and computational expense. The various metal/MgO interface systems have been studied intensively so far, for example, Ag, Au, Cu, Pd, Pt Ru and Rh (Li and Freeman, 1991; Huang *et al.*, 1993; Didier and Jupille, 1994). Because Rh itself is not only an active catalyst in many catalytic processes, it is also an active catalyst when combined with various metal oxide supports. Hence, the combination interface systems of Rh/MgO(001) and Rh/CeO₂ are very interesting. In order to understand the reactions of metal-metal oxide systems, the interaction of Rh/MgO(001) as well as that of Rh/CeO₂ interface systems were theoretically investigated here in terms of interaction energies and electronic properties. The examples of bulk structures for MgO, CeO₂ and Rhodium systems are depicted in Figure 2.

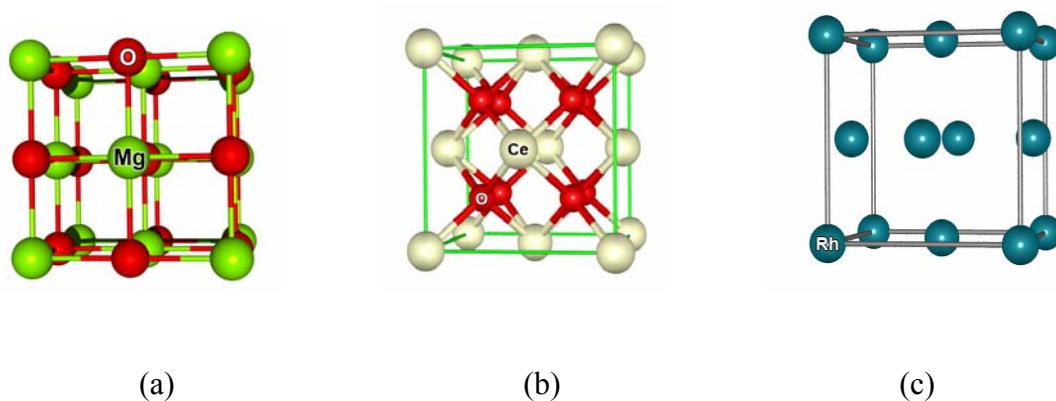


Figure 2 The bulk structures of (a) MgO, (b) CeO₂ and (c) Rhodium systems.

Finally, the systems studied with the corresponding objectives will be reported throughout this thesis are summarized below:

1. Catalysis in Zeolites and Nanostructured Materials: Aluminosilicate systems

- Faujasite/(H₂O)_n systems
- Faujasite/(CH₃OH)_n systems

The aims of these topics studied are

1. To investigate the important consequences of adsorbed probe molecules at low and high coverages.
2. To investigate modes of adsorption as well as the proton transfer in the system.
3. To obtain structures and reaction mechanism of high coverages in zeolite catalyst.

2. Catalysis on surfaces: Metal oxide systems

- Rh/MgO(001) systems
- Rh/CeO₂ systems

The corresponding objectives of these topics studied are

1. To study the catalytic functionality of the metal-metal oxide systems.
2. To investigate the structural and energetic properties as functions of “adsorption site dependence” as well as “coverage dependence”.
3. To examine the electronic properties, e.g., the electron density difference, the density of states (DOS), the electron localization function (ELF) and spin magnetic moment.

LITERATURE REVIEW

Catalysis in Zeolites and Nanostructured Materials:

Aluminosilicate systems

The adsorption processes of a water cluster in various types of zeolites have been intensively studied so far. The adsorption of an isolated water molecule in the zeolite system has been reported in the neutral form. This result was confirmed by the IR spectroscopy (Jentys *et al.*, 1989). Moreover, the same authors also reported that the hydroxonium ions could be observed when at least three water molecules existed in the system. Soon after, the protonated form of H_5O_2^+ and $\text{H}^+(\text{H}_2\text{O})_n$, at two or more water molecules per site were also reported by IR (Marchese *et al.*, 1993; Zecchina *et al.*, 1996a; Kondo *et al.*, 1997). The protonated and hydrogen-bonded species were reported when water interacts with Brønsted acid sites in a small zeolite structure, HSAPO-34 (Smith *et al.*, 1996). An H_3O^+ ion is found in the eight-ring channel of the zeolite and a second water molecule is hydrogen-bonded to an acid site on the six-ring. However, the study of the water adsorption in H-ZSM-5, at different concentrations, was reported that the first water molecule is attached to the acid site via two hydrogen-bonded interactions and hydroxonium ions are not found in H-ZSM-5 (Jobic *et al.*, 1996).

As for theoretical results, the interactions of water at zeolite Brønsted acid sites using the embedding technique, 3T cluster including potential derived charges (PDC), (Greatbanks, *et al.*, 1996) reported that the hydrogen-bonded complex was predicted to be the stable structure. The adsorption of one and two water molecules on 5T cluster models of Brønsted acid sites of zeolite catalysts has been investigated by ab initio quantum chemical methods (Krossner *et al.*, 1996). For the water monomer system, two possible structures – the neutral complex and the hydroxonium ion – can be observed. Only the neutral structure was predicted to be the stable structure whereas the ion pair complex was considered to be a transition structure. However, the energy difference between both structures is only a few kJ/mol. As for the water dimer system, both the neutral and the ion pair structures were proved to be local

minima on the potential energy surface, and the ion pair structure becomes the more stable one. These results agreed well with the calculation using the 3T cluster model (Zygmunt *et al.*, 1996). Afterward, the structures and the potential energy surface of the faujasitic zeolite/water system have been investigated (Limtrakul *et al.*, 1997). The hydrogen-bonded system was also stated here. Subsequently, the ab initio simulations of water adsorbed in the HSAPO-34 were reported (Termath *et al.*, 1996) that both H₂O and H₃O⁺ are presented when this solid acid is loaded with water. It was suggested that the acid-base reaction requires at least three water molecules per two nearby acidic sites in the micropores of the solid and leads to a protonated water cluster, H₃O⁺(H₂O)₂. Recently, the interactions of water in the H-ZSM-5 system using a 5T cluster model were investigated by means of DFT calculation (Rice *et al.*, 1998). It was found that water adsorbs by direct interaction of the O atom with the cation and hydrogen bonding of one of the two H atoms with an oxygen atom in the zeolite framework and no proton transfer can be observed.

One of the most important and widely studied petrochemical processes involving zeolite catalysts is the methanol to gasoline (MTG) conversion (Meisel *et al.*, 1976). Although considerable effort has been devoted to the study of the MTG process, the mechanistic details of the process are still not clearly known. Experimental studies (Munson, *et al.*, 1991; Sulikowski and Klinowski, 1992; Munson *et al.*, 1992) have indicated that methanol is dehydrated to dimethyl ether (DME), then a mixture of methanol and dimethyl ether is converted to olefins, aliphatics, and aromatics. From these basic steps, different reaction pathways have been proposed in the research studies (Kubelkova *et al.*, 1990; Bandiera and Naccache, 1991; Schiffino and Merrill, 1993). The pathway involving the simultaneous adsorption of two methanol molecules is believed to be the preferred route for producing dimethylether (Blaszowski and van Santen, 1997). The systems of methanol adsorption in zeolite have been studied experimentally [using IR (Kubelkova *et al.*, 1990; Forester and Howe, 1987; Mirth *et al.*, 1990; Zecchina *et al.*, 1996b; Kotrla *et al.*, 1998; Anderson *et al.*, 1991) and NMR (Munson *et al.*, 1992; Anderson *et al.*, 1991; Anderson and Klinowski, 1990; Bronnimann and Maciel, 1986; Bosacek, 1993) techniques] and theoretically (Greatbanks *et al.*, 1996; Haase

and J. Sauer, 1995; Limtrakul, 1995; Nusterer *et al.*, 1996; Shah *et al.*, 1996a; Shah *et al.*, 1996b; Shah *et al.*, 1997; Gale *et al.*, 1993; Gale, 1996; Blaszkowski and van Santen, 1995; Stich *et al.*, 1998; Mihaleva *et al.*, 2001; Haase *et al.*, 1997). However, considerable research effort has been carried out to experimentally and theoretically study the adsorption of methanol, but it is still being debated as to whether the adsorption complex is a physisorbed, $\text{CH}_3\text{OH}\cdots\text{H-Zeolite}$, or a chemisorbed, $[\text{CH}_3\text{OH}_2]^+\cdots[\text{Zeolite}]^-$ structure.

Most of the theoretical studies using small cluster fragments to represent the acid site depicted that the acidic proton transfer to the adsorbed methanol molecule can occur if symmetry constraints are employed. Therefore, physisorbed methanol complexes were found to be stable structures, whereas chemisorbed species were predicted to be a transition state for the hydrogen exchanged reaction. Inclusion of the lattice framework effects to the zeolite model has provided significantly different results. The electrostatic potential from the zeolite framework, represented by the PDC lattice point charges, was found to enhance the probability of proton transfer to the methanol in the embedded 3T cluster system and suggested that increasing the cluster size would increase the proton-donating ability of proton-zeolite (Greatbanks *et al.*, 1996).

Using the periodic calculation, it was reported that the chemisorbed methanol complex was more energetically stable than the physisorbed complex in chabazite zeolite (Shah *et al.*, 1996a). The stability of equilibrium methanol complexes in small zeolites, such as chabazite, depends on the position of the adsorbed site in the zeolite framework. If the methanol molecule is adsorbed over the Al site, the chemisorbed complex is the only stable structure observed. On the other hand if the adsorption takes place at the adjacent Si site, the physisorbed hydrogen-bonded complex is observed in the zeolite system. Consequently, the periodic MD calculation reported that both physisorbed and chemisorbed methanol complexes were found to be the minimum structures in the potential energy surface (PES) (Haase *et al.*, 1997). The former was more energetically favorable than the latter by up to 18 kJ/mol. Recently, the observation of both the physisorbed and chemisorbed methanol complexes on an

8T ring cluster of chabazite as the minimum states in the PES was reported (Mihaleva *et al.*, 2001). The physisorbed complex was predicted to be more stable by about 10 kJ/mol. It was suggested that the 8T ring cluster of chabazite was an adequate model for studying the methanol adsorption in the small unit cell chabazite zeolite since their results compared well with the previous theoretical periodic studies (Shah *et al.*, 1997; Haase *et al.*, 1997).

The theoretical studies of the dimethylether synthesis processes indicated that the adsorption of two methanol molecules reduced the activation energy for methyl oxonium ion mechanism in comparison to the single methanol system (Sinclair and Catlow, 1996). The second methanol molecule was suggested to increase the probability of proton transfer in the methanol adsorption system (Gale, 1996; Limtrakul, 1995). Systems of two methanol molecules per zeolitic acid site have been studied using 3T (Limtrakul, 1995; Gale *et al.*, 1993), 4T (Gale, 1996) and 5T (Blaszowski and van Santen, 1995) model fragments, but showed no evidence of proton transfer. However, the recent results obtained from periodic calculation with rather small unit cell zeolites like sodalite (Nusterer *et al.*, 1996), chabazite (Shah *et al.*, 1997), and ferrierite (Stich *et al.*, 1998) were found that chemisorbed methanol can exist. One of the methanol molecules became a methoxonium cation having strong interactions with the zeolite framework and with the second methanol molecule.

Catalysis on surfaces: Metal oxide systems

The structure of a Rh/MgO catalyst was investigated by EXAFS (Extended X-ray absorption fine structure spectroscopy) (Emrich *et al.*, 1985). It was found that rhodium bound to the MgO support through a Rh...O interaction with the corresponding bond distance 1.95 Å. It has also been reported that the epitaxial growth of Rh thin films on MgO(100) was found to have good thermal stability at high temperature (Delplancke *et al.*, 1986). The X-ray photoelectron spectroscopy (XPS) (Baltanas *et al.*, 1987) was used to characterize the ionic state of Rh atoms and it was found that rhodium was reduced from Rh³⁺ to Rh after reduction at 473 K.

As for theoretical study, to the best of our knowledge, only a small number of Rh/MgO studies have been published in the literature (Wu and Freeman, 1995; Stirling *et al.*, 1997; Bogicevic and Jennison, 2002; Giordano *et al.*, 2003; Judai *et al.*, 2003). The investigation of the interactions of Pd, Rh and Ru monolayers on MgO(001), using full potential linearized augmented-plane-wave (FLAPW) periodic calculation, was explored (Wu and Freeman, 1995). The monolayer of such metal atoms were placed on top of every surface oxygen for each side of a five-layer MgO slab model (using the definition that full coverage, i.e. 1 ML, is when either each cation or each anion is covered by one metal atom). They found adhesion energy of 0.84 eV and an optimized Rh-O distance of 2.34 Å. Moreover, Rh and Ru monolayers were found to be able to preserve large spin magnetic moments on MgO(001). The reactivity of Rh and Pd atoms on MgO(001) and their reactivity with NO and NO₂ were reported (Stirling *et al.*, 1997). Here, 1/8 ML coverage investigated whether the metal atoms were either covered on top of the surface Mg or O atoms only on one side of the one-layer MgO slab. They found that Rh preferred to bind to the O atom rather than to Mg, with the optimized Rh-O distance 2.1 Å and the corresponding interaction energy of 1.8 eV. The interaction of either NO or NO₂ on Rh/MgO systems was also investigated and discussed. Very recently, the effect of oxide vacancies on MgO(100) was investigated (Bogicevic *et al.*, 2002) when one of either transition metals were adsorbed on the surface, one such of those metal atoms is Rh. The 1/18 ML coverage was investigated by means of periodic plane-wave

calculations with the GGA (generalized gradient approximation) treatment of the exchange-correlation functional. The metal atoms were placed only one side of a five-layer MgO slab and the adsorption energy and the optimized distance for Rh on top of O were reported to be 1.93 eV and 2.01 Å, respectively. Lately, the interaction of CO adsorption on Rh/MgO, Pd/MgO and Ag/MgO systems (Giordano *et al.*, 2003; Judai *et al.*, 2003) were explored by means of DFT embedded study. For the Rh/MgO interface (without CO), the corresponding Rh...O bond length and adsorption energy were reported to be 2.26 Å and 0.97 eV, respectively and they also found a small charge transfer between metal atoms and MgO substrate which agreed well with the periodic calculation of Ag/MgO (Li *et al.*, 1993).

The more complicated structure metal oxide, namely CeO₂, has also been intensively reported so far. Some selected literatures related to this thesis work are stated here. The optical reflectivity of CeO₂ single crystals was reported (Marabelli and Wachter, 1987). It was measured at 0.001-12 eV at 300 K and analyzed in terms of a Kramers-Kronig transformation. Static and optic dielectric constants, transverse optical- and longitudinal optical-phonon frequencies, the effective charge, and the degree of covalency were obtained. It can be asserted that CeO₂ is not of intermediate valence, but it is a covalent insulator.

The mechanical, thermodynamic and electronic properties for the ground state of bulk CeO₂ were investigated using the Restricted Hartree-Fock periodic method (Hill and Catlow, 1993). The lattice parameter was calculated to be 5.385 Å, and the bulk modulus 35.7×10^{11} dyne cm⁻² for the lowest energy inflation. A small charge transfer from the cation to the anions was calculated as 2.3% per unit cell. The electronic band structure was dominated by metal an *sp* character in the lower part of the valence band, and by an O *2p* character in the upper part. Partially covalent bonding was evident between cations, and also between cations and anions. The anion-anion interaction is found to be highly ionic.

Computer simulation techniques are used to model the surfaces of ceria (Sayle *et al.*, 1994), paying special attention to the effects of surface structures and energetics on catalytic activity. Three surfaces of CeO₂ have been investigated for both their structure and relative stability. The results show that the three low energy surfaces are the (111), (110) and (310) with the first of these three being the most stable. Defects including oxygen vacancies and reduced cerium ions were found to be more stable at the surfaces than in the bulk of the crystal. Finally, the ready formation of oxygen vacancies on the (110) and (310) surfaces of CeO₂ was shown, significantly promotes the oxidation of carbon monoxide.

The quantum mechanical (QM) calculations, at a periodic Hartee-Fock (HF) level, on the bulk and surface properties of cubic CeO₂ and ZrO₂ were studied (Gennard *et al.*, 1999). The M-O bonding features, and established the high degree of ionicity of both materials, which is greater for CeO₂ than ZrO₂ were reported. The calculated values for the C11, C12, and C44 elastic constants are in close agreement with experiment; an extended oxygen basis set, containing *d*-orbital polarization functions, is essential to model accurately the symmetry lowering during the C44 distortion. In the surface studies, the surface energies of the {011} and {111} faces of both ceria and zirconia were calculated. QM results are compared with interatomic potential-based (IP) methods to assess the accuracy of the latter. It was found that IP methods provide a correct estimate of the surface relaxations and the correct order of stability of the two faces examined, with the energy difference between the {011} and the {111} surfaces being approximately 1 J/m², as in the QM study. However, IP methods do not always discriminate adequately between the properties of the two materials. The geometric and electronic relaxations in the {111} surface are confined to the outermost oxygen ions, while in the {011} slabs they are more important and extend to the subsurface layers in a columnar way. The unsaturation of the surface ions in the {011} face may have important implications for the catalytic activity of the materials.

The electronic, structural, bonding, optical, and magnetic properties of the most important cerium oxides, CeO_2 and Ce_2O_3 were explored by means of the full-potential linear muffin-tin orbital method (FP-LMTO) in the framework of the density functional theory using the local density and generalized gradient approximations (Skorodumova *et al.*, 2001). Due to the significant roles in the interaction, the $4f$ states of the Ce atoms are treated by two models, as fully localized corelike states and as valence-band-like states. The former model is realized by considering the Ce $4f$ electron as a part of the inner core, while the $4f$ wave functions were included as part of the valence band in the latter model. Better agreements with experimentally known parameters for Ce_2O_3 within the core-state model and within the valence-band model for CeO_2 are obtained. In the case of CeO_2 the calculated density of states, optical transitions, and electron localization function indicate that the unoccupied $4f$ states of Ce can be considered as essentially equivalent to an empty atomiclike $4f$ level. In this study, the natural bonding characters in CeO_2 and Ce_2O_3 were described as polarized ionic.

The periodic density functional theory calculations within the GGA Hamiltonian for monolayers of Pd and Pt supported on the $\{111\}$ surfaces of cubic- ZrO_2 and CeO_2 were presented (Alfredsson and Catlow, 2002). It is found that the adsorption energies for the Pd-layer on both the zirconia and ceria supports are *ca.* 200 kJ mol^{-1} , while the corresponding adsorption energies for the Pt-layers are *ca.* 400 kJ mol^{-1} . The predicted Pt-Pt interactions are three times stronger ($\sim 300 \text{ kJ mol}^{-1}$) than the corresponding Pd-Pd interactions, explaining the different cluster shapes and metal growth modes observed experimentally. The electronic structure of the support determines the geometrical structure of the interface: a tilting of *ca.* 20° compared to the underlying ZrO_2 substrate is identified, which is not observed for the CeO_2 substrate. Furthermore, the bonding character between the metal ad-layers and the oxide supports is dominated by electrostatic forces, owing to the polarization of the metal ad-layers; yet a weak hybridization between the outermost oxygen ions and the metal ad-layers is also present. The CeO_2 interfaces investigated show metallic properties as a result of metal induced gap states originating from the metal ad-layers, while the ZrO_2 interfaces show a small band gap of *ca.* 0.1 eV .

Evidences for coverage of rhodium metal particles by CeO_x species in high surface Rh/CeO₂ catalysts reduced at 673 and 773 K were reported (Belzunegui and Sanz, 2003). From ¹H NMR data, the total elimination of metal hydrogen adsorption, produced in catalysts reduced at 773 K, results from the electronic perturbation and the partial decoration of metal particles with CeO₂ overlayers. Oxidation of Rh/CeO₂ catalyst produces the elimination of the metal electronic perturbation in the range of 273-473 K, but the metal coverage is only eliminated after oxidation at 673 K. In Rh/CeO₂ catalysts, electronic and coverage effects are difficult to differentiate, requiring partial oxidation of Rh/CeO₂ catalysts to detect the metal decoration. The comparison of the intensity of the NMR line B of reduced samples after oxidations at 473 and 673 K allowed an estimation of the metal coverage extent. The coverage of the metal particles depends on the reducibility of the support, increasing with the temperature and time of reduction.

The surface energies and electronic structure of (111), (110) and (100) surfaces of CeO₂ were examined using the density functional (DFT) plane-wave method (Skorodumova *et al.*, 2004). The PAW method within both the LDA and GGA were selected to perform the calculations. Moreover, the molecular dynamics (MD) simulations at 10 K was also investigated to compare the results with the DFT plane-wave calculations. Among of the three surfaces studied, the (111) surface was found to be the most stable structure compared to the others. The calculated surface energy is 1.0 J/m² (LDA) and 0.7 J/m² (GGA) which are lower than the previous surface energy reported in literature, including the MD results (1.4 J/m²) in this study. For the (110) surface, the corresponding surface energies (LDA, GGA and MD) are 40% - 60% higher than for the (111). The structural relaxation for the (110) is reported larger than for the (111), these obtained results show excellent agreement among LDA, GGA and MD calculations. The electronic density of states shows a larger difference between the surface and the bulk for the (110) than for the (111), for example, a decrease of the band gap between the valence band and the empty Ce 4*f* band in the (110) surface region compared to the bulk.

The adsorption of CO on (111), (110) surfaces of ceria was reported (Yang *et al.*, 2004a) by using PAW and GGA methods. The different features of CO adsorption (weak and strong adsorption interactions) on (111) and (110) surfaces were investigated. Only weak adsorptions are found on the (111) surface whereas both weak and strong adsorption exist on (110) surface. The covalent bonding was involved for the strong adsorption while the electrostatic interactions were determined in the case of weak adsorption. The strongly adsorbed CO on (110) surface forms carbonate species as found in the IR experiments.

The atomic and electronic structure of (111), (110) and (100) surface of ceria (CeO_2) were studied (Yang *et al.*, 2004b) using the DFT within the GGA. The unreduced and reduced surfaces (with oxygen vacancies) were investigated. It was found that the (111) surface is the most stable among the considered surfaces, followed by (110) and (100) surfaces, in agreement with the experimental data and previous theoretical results. Different features of surface relaxation are found. The (111) shows a very small relaxation whereas the larger relaxations are found for the (110) and (100) surfaces. In the case of reduced systems, the (111) and (110) surfaces were selected to study the oxygen vacancy. The formation of oxygen vacancy is closely related to the surface structure and occur more easily for the (110) than for the (111). The preferred vacancy location is in the surface layer of the (110) and in the subsurface layer of the (111). The O vacancies of both surfaces are more easily formed than in the bulk system. More localization of charges due to the O vacancy is found in the first three layers of the surface.

Recently, the structure and electronic properties for bulk and low index surfaces (111), (110), and (100) of ceria were investigated by means of the periodic DFT calculations (Nolan *et al.*, 2005). The surface energies were found to increase in the order $(111) > (110) > (100)$, while the magnitude of the surface relaxations follows the inverse order. The electronic density of states and electron density were utilized to clarify the electronic properties of bulk and surface systems. The bonding character in pure ceria is partially covalent and the presence of localized Ce 4*f* states above the Fermi level is confirmed by the electronic states analysis. The small change

of charges in the surface atoms is found due to the changes in O $2p$ and Ce $5d$ states. The investigation of an oxygen vacancy on the (100) surface shows the problematic errors in explaining the strong localized system. The DFT+U method, thus, was introduced to study the oxygen vacancy (100) surface and reported the appearance of new gap states between the valence band and the empty Ce $4f$ band. These states are localized on the Ce^{III} ions neighboring the oxygen vacancy. The vacancy is bound by two Ce^{III} ions which are reduced from Ce^{IV}. The remaining Ce ions are in the Ce^{IV} states. The localization of Ce $4f$ electrons modifies the predicted structure of the defective surface.

METHODS OF CALCULATIONS

Density functional theory (DFT)

In this section, a very brief description of computational chemistry methods is presented to provide an overview of the quantum mechanical technique utilized in this thesis. An in-depth detail of the computational methods can be found in the relevant text books. The Density functional theory (DFT) is selected as the method used throughout this thesis. The description details of the DFT are summarized here.

Density functional theory (DFT) is one of the most widely used techniques for computational chemistry nowadays. Its advantages include less demanding computational effort, less computational time and better agreement with the experimental values than that of the Hartree-Fock procedures.

The central focus of DFT is the electron density, ρ , rather than the wavefunction ψ . The energy part of the molecules is a function of the electron density, $E[\rho]$ and the electron density is itself a function of position, $\rho(\mathbf{r})$. The exact ground-state energy of an n-electrons molecule is

$$E[\rho] = T[\rho] + E_{ne}[\rho] + E_{ee}[\rho] + E_{xc}[\rho] \quad (1)$$

where $T[\rho]$ is the total electron kinetic energy, $E_{ne}[\rho]$ the electron-nucleus potential energy, $E_{ee}[\rho]$ the electron-electron potential energy, and $E_{xc}[\rho]$ the **exchange-correlation energy**, which takes into account all the effects due to all interactions among electrons in the system. The orbitals used to construct the electron density from

$$\rho(\mathbf{r}) = \sum_{i=1}^n |\psi_i(\mathbf{r})|^2 \quad (2)$$

are calculated from the *Kohn-Sham equations*, which are found by applying the variational principle to the electron energy, and are like the Hartree-Fock equations except for a term V_{XC} , which is called the exchange-correlation potential:

$$\left\{ -\frac{\hbar^2}{2m_e} \nabla_1^2 - \sum_{j=1}^N \frac{Z_j e^2}{4\pi\epsilon_0 r_{j1}} + \int \frac{\rho(r_2) e^2}{4\pi\epsilon_0 r_{12}} dr_2 + V_{XC}(r_1) \right\} \psi_i(r_1) = \epsilon_i \psi_i(r_1) \quad (3)$$

The exchange-correlation potential is the ‘functional derivative’ of the exchange-correlation energy:

$$V_{XC}[\rho] = \frac{\delta E_{XC}}{\delta \rho} \quad (4)$$

The Kohn-Sham equations are solved iteratively and self-consistently. First the electron density is guessed. For this step it is common to use a superposition of atomic electron densities. Then the exchange-correlation potential is calculated by assuming an approximate form of the dependence of the exchange-correlation energy on the electron density and evaluating the functional derivative in equation (4).

The major problem of DFT is that an exact term for $E_{XC}[\rho]$ is not known and approximate functionals must be used. Thus, many types of functionals are available; the simplest approximation is the *local-density approximation (LDA)*, which is dependent only on the electron density. The *Generalized Gradient Approximation (GGA)* functionals include the gradient of the electron density as well as the electron density. The *Hybrid functional* has also been proposed. The B3LYP functional is one such functional that is the most widely used nowadays. DFT can be implemented either with an atom-centered localized basis set or with a plane-wave basis set. Such basis sets are also used in this thesis works as will be stated in the “Models and Methodologies” section.

Models and methodologies

Two types of computational approaches were used in this dissertation as listed below:

1. Finite cluster and Embedded cluster approaches

All calculations were performed within the framework of DFT using GAUSSIAN 98 (Frisch *et al.*, 1998). The nonlocal hybrid B3YLP (Becke, 1993) density functional method with different atom-centred localized basis sets were used. The details of the basis set used for such systems studied were shown in the forthcoming sections. The finite cluster and embedded cluster approaches are selected to investigate the interactions for “Faujasite/(H₂O)_n systems” and “Faujasite/(CH₃OH)_n systems”. The “*finite cluster models*” are taken from the active part of the zeolite framework and this part is treated with the quantum mechanical method. The more realistic model, namely, “*embedded cluster models*” is presented by the extended framework of zeolite. Two types of point charges are taken into account for the environment effect derived from the “Surface Charge Representation of the Electrostatic Embedding Potential, (SCREEP)” method (Stefanovich and Troung, 1998) (see Figure 3).

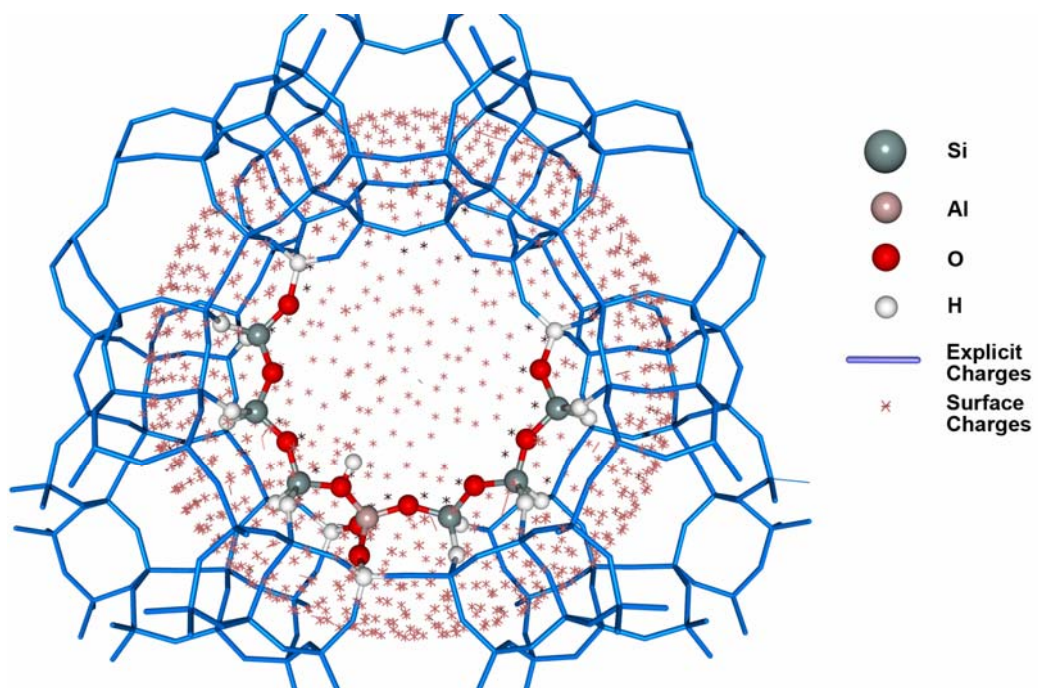


Figure 3 The embedded cluster models created from the SCREEP approach

1.1 Faujasite/(H₂O)_n systems

Cluster and embedded cluster models were used to determine the structure of water molecules adsorption of zeolites [H₃SiOHAl(OH)₂OSiH₃]/[H₂O]_n ; n = 1-4 and their possible ion-pair species. The cluster is selected to model specially to faujasite zeolite (3T cluster, see Figure 4) with the symmetry C1. In models employed, the dangling bonds of “surface” oxygen atoms are terminated by H atom and Si-H bonds are aligned with the corresponding Si-O bonds of the structure of Faujasite zeolite.

In the embedded cluster model, the static Madelung potential due to atoms outside of the quantum cluster was represented by partial atomic charges located at the zeolite lattice sites. Charges close to the quantum cluster are treated explicitly while the Madelung potential from the remaining charges from an infinite lattice is represented by a set of surface charges that were derived from the Surface Charge Representation of External Electrostatic Potential (SCREEP) method. In this study, the total Madelung potential is represented by 1,137 explicit charges and 146 surface charges. With this small number of point charges, additional computational cost is often less than 5% compared to bare cluster calculations.

Geometry optimizations were investigated with the density functional theory at the B3LYP/6-31G(d,p) level of theory using the GAUSSIAN 98 program code (Frisch *et al.*, 1998).

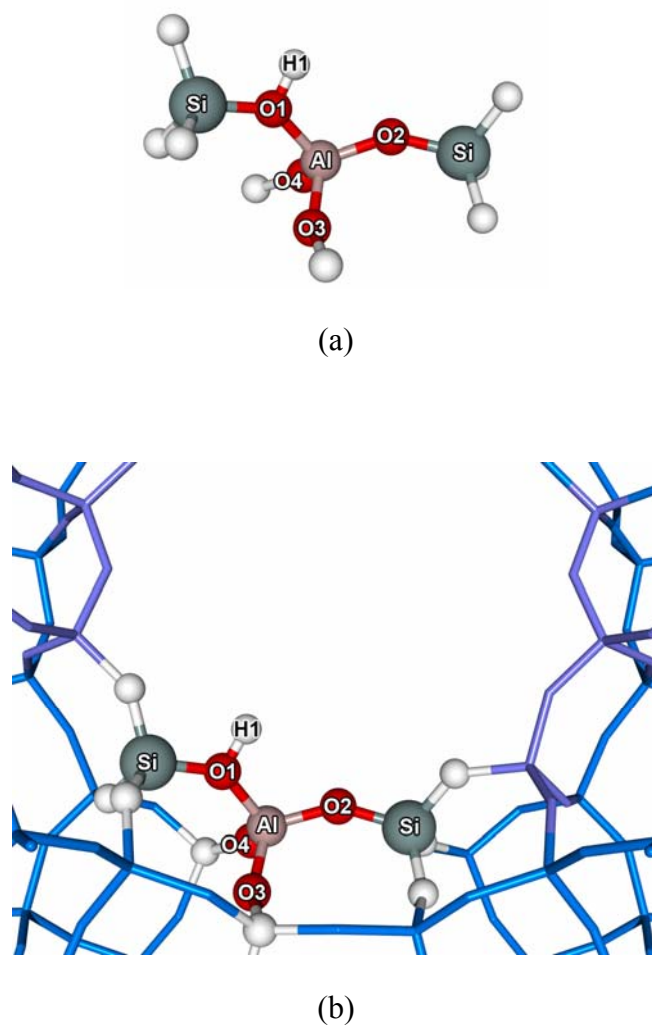


Figure 4 Faujasite cluster model: a) 3T and b) 3T Embedded clusters

1.2 Faujasite/(CH₃OH)_n systems

Quantum cluster and embedded cluster approaches were used to study the interactions of methanol molecules with Faujasite zeolite. Two different clusters, 5T and 7T, were selected from the Faujasite zeolite lattice at the site of interest (see Figure 5). In the model employed, the dangling bonds of surface oxygen atoms were aligned with the corresponding Si-O bonds of the structure of Faujasite zeolite and terminated with H atoms fixed while the remaining atoms were allowed to relax. In the embedded cluster model, the electrostatic potential from the zeolite framework is represented by the explicit charges and surface charges derived from the Surface Charge Representation of External Electrostatic Potential (SCREEP) (Stefanovich and Truong, 1998). In this study, the total Madelung potential is represented by 441 explicit charges and 1,310 surface charges. With this small number of point charges, additional computational cost is often less than 5% when compared to bare cluster calculations.

All calculations were performed using the nonlocal hybrid B3LYP (Becke, 1993) density functional method with 6-31G(d,p) and B3LYP/6-311+G(3df,2p)//B3LYP/6-31G(d,p) basis sets with GAUSSIAN 98 program code (Frisch *et al.*, 1998). The basis set superposition error (BSSE) has also been carried out with counterpoise correction (Boys and Bernardi, 1970). Additionally, the harmonic frequency calculations were also reported for the selected chemisorbed model.

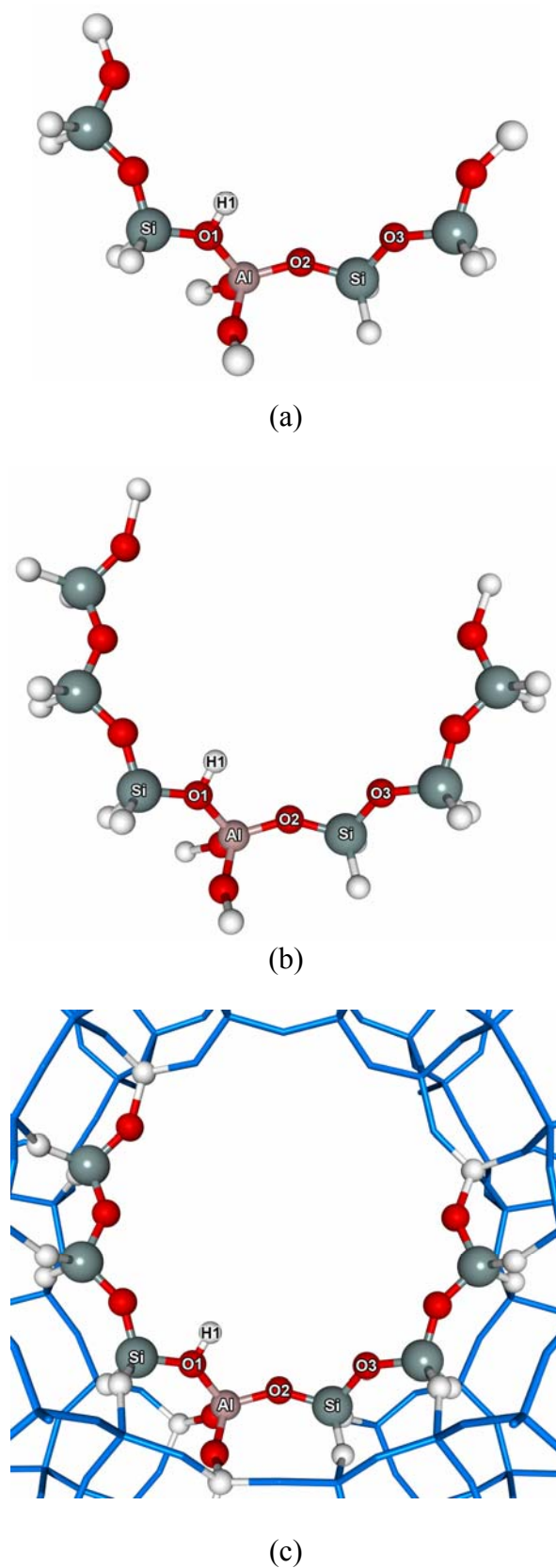


Figure 5 Faujasite cluster model: a) 5T, b) 7T and c) 7T Embedded clusters.

2. Periodic plane-wave approach

Periodic density functional theory (DFT) calculations were performed using the Vienna Ab initio Simulations package, VASP (Kresse and Hafner, 1993; Kresse and Furthmüller, 1996) in which the electron density is expanded in a plane-wave basis set. The projector augmented-wave method (PAW) (Blöchl, 1994; Kresse and Joubert, 1999) as implemented in VASP with the frozen-core approximation combines the accuracy of augmented plane-wave methods with the flexibility of the pseudopotential approach was used. The exchange and correlation generalized gradient correction (GGA) (Perdew *et al.*, 1992) were applied.

A 2-dimensional periodic (in x and y) slab model was mimicked using the 3-dimensionally periodic VASP code. A Rh layer was placed epitaxially on one side of the oxide slab (MgO, CeO₂) and a vacuum-layer with a thickness of 15 Å was found to be sufficient for the surface calculations. The periodic supercell for MgO(001) and CeO₂ systems are illustrated in the next sections.

2.1 Rh/MgO(001) systems

Calculations were performed for bulk MgO and bulk Rh (primarily as reference systems) as well as for a number of Rh/MgO(001) systems, with different coverages and different adsorption sites.

In this studied system, both spin-polarized and non-spin polarized calculations are reported. A cut-off energy of 500 eV was used in all cases. The electronic configurations of the atomic species employed in our calculations are Rh(4*p*, 5*s*, 4*d*), Mg(2*p*, 3*s*) and O(2*s*, 2*p*). The Brillouin zone integrations were performed using the Monkhorst-Pack (MP) algorithm (Monkhorst and Pack, 1976) with a Gaussian smearing factor with $\sigma = 0.1$ eV and k-mesh points of 6x6x6 and 6x6x1 for bulk and surface calculations, respectively. All structures were optimized until the forces on all unconstrained atoms were less than 0.01 eV/Å.

Three different coverages (1/8, 1/2 and 1 ML) at three different sites (on top of O, Mg and the hollow) were explored (see Figure 6). For 1/2 and 1 ML coverages, the 2-dimensionally periodic computational box consisted of 1x1 crystallographic unit cells in the x and y directions was chosen and 8 MgO layers along z . For the lowest coverage (1/8 ML), a 2x2 supercell of 4 layers was used. The 3-dimensional supercell in such cases studied is shown in Figure 7. For all systems, all atoms were allowed to fully relax in all directions under the condition that the cubic unit cell was kept fixed at the optimized bulk lattice parameter of 4.25 Å [the experimental value is 4.21 Å (Wyckoff, 1964)].

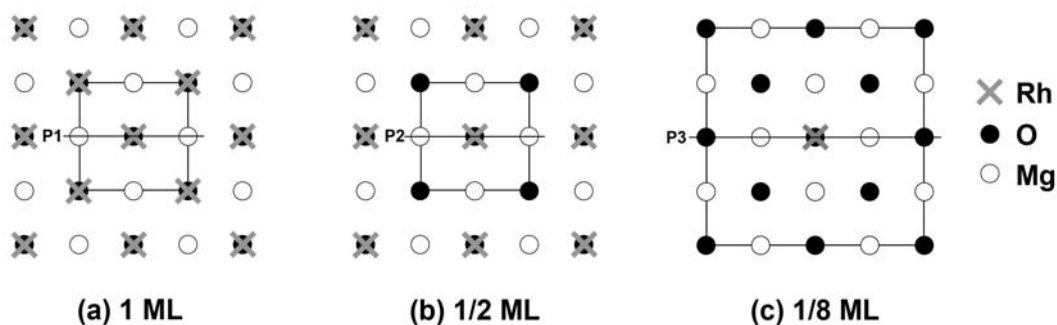


Figure 6 The surface coverage definitions for the Rh/MgO(001) systems. In these figures the Rh atoms were placed on top of the surface oxygen. The square box represents the sizes of the supercell used in this study: (a) and (b), the 1x1 crystallographic unit cells are selected for 1 and 1/2 ML coverage, respectively, (c) the 2x2 crystallographic unit cell is used for 1/8 ML coverage. The P1, P2 and P3 are the selected perpendicular planes to use for illustrating the total charge density and the electron density difference plots.

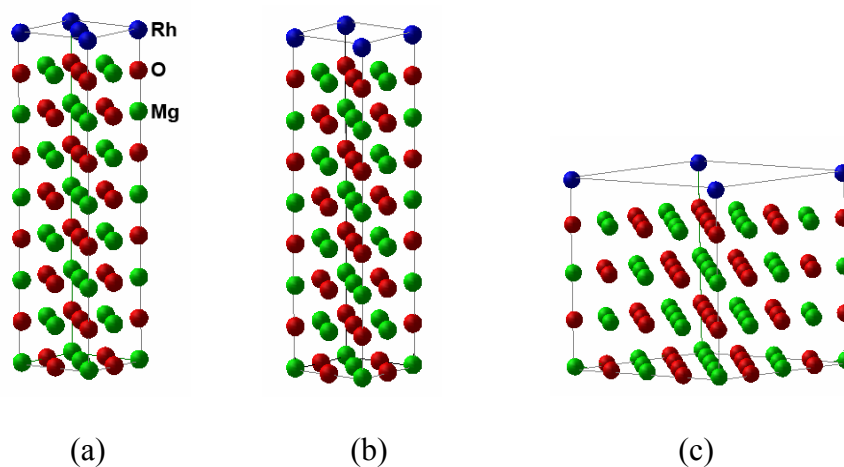


Figure 7 The 3-dimensional supercell for Rh/MgO(001) systems for: (a) 1 ML, (b) 1/2 ML and (c) 1/8 ML coverages.

Three energetic properties — adsorption energy, adhesion energy, and formation-of-layer energy — are reported. Moreover, the electronic properties such as density of states (DOS), electron density difference plot, total spin density and the electron localization function (ELF) are presented to clarify how the metal and the oxide systems affect each other via the metal-oxide bonds.

2.2 Rh/CeO₂ systems

All calculations have been performed using the VASP package. A cut off energy of 408 eV was used in all cases and the electronic configurations of the atomic species employed in our calculations are Rh(4*p*, 5*s*, 4*d*), Ce(5*s*, 5*p*, 5*d*, 4*f*, 6*s*) and O(2*s*, 2*p*). For this system, non-spin polarized calculations are reported. The Brillouin zone integrations were performed using the Monkhorst-Pack (MP) algorithm with a Gaussian smearing factor with $\sigma = 0.1$ eV.

2.2.1 Model system geometries

a. Bulk system

The MP k-mesh points of (8×8×8) were used for bulk systems. The calculated lattice parameter is 5.47 Å, in agreement with both the experimental report 5.41 Å (Eyring, 1979) and the theoretical calculations in the literature [5.47 Å (Skorodumova *et al.*, 2001; Nolan *et al.*, 2005), 5.385 Å (Hill and Catlow, 1993)]

b. Surface systems

In this study, both of “the adsorption site dependence” and “the coverage dependence” were investigated. The adsorption site dependence was initially investigated to predict the preferable adsorption site. Afterward, the coverage dependence was studied at the most stable adsorption site.

1) The adsorption site dependence

The *p*(1×1) lateral cells consisting of 9 and 21 layers of periodic ceria slab were selected as models for the (110) and (111) surface systems, respectively (see Figure 8). These models are noted as CeO₂(110)*p*(1×1) and CeO₂(111)*p*(1×1). In case of the (111) orientation, the oxygen terminated model was used to prevent non-zero dipole moment perpendicular to the surface. Two adsorption

sites, namely, the surface oxygen (O_s) and the surface cerium (Ce) sites, were explored for (110) orientation and three adsorption sites for (111) surfaces, i.e., the surface oxygen (O_s), the subsurface cerium (Ce) and the subsurface oxygen (O_{ss}), were investigated. The MP k-mesh points of $(8 \times 10 \times 1)$ and $(10 \times 10 \times 1)$ were used for $\text{CeO}_2(110)p(1 \times 1)$ and $\text{CeO}_2(111)p(1 \times 1)$, respectively. The slab models were allowed to fully relax in all directions under the condition that the dimensions and shape of the unit cell were kept fixed at the calculated lattice parameter value, here 5.47 Å (the experimental value is 5.41 Å). The vacuum layer thickness of 15 Å was found to be sufficient to minimize the surface-surface interaction. All structures were optimized until the forces on all unconstrained atoms were less than 0.01 eV/Å. To study the adsorption site dependence, 1 ML coverage of Rh monolayer was placed epitaxially on top of one side of the ceria slab. The 1 ML coverage was defined by the fully loaded Rh atom which binds directly on top of every atom in each adsorption site as shown in Figure 10.

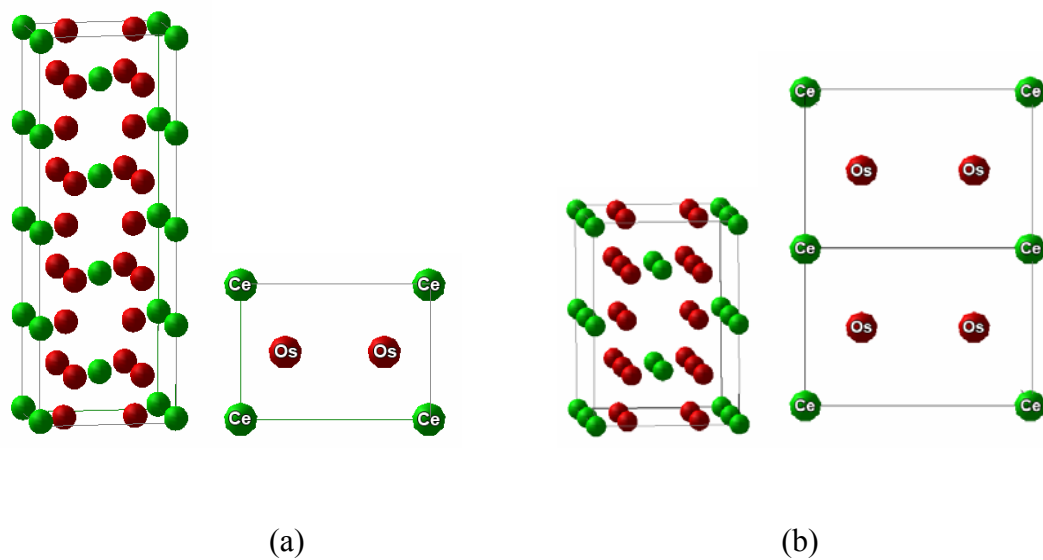


Figure 8 The supercell used in the calculations for $\text{CeO}_2(110)$ systems: (a) $p(1 \times 1)$ and (b) $p(1 \times 2)$. The corresponding top view of the topmost surface is also shown.

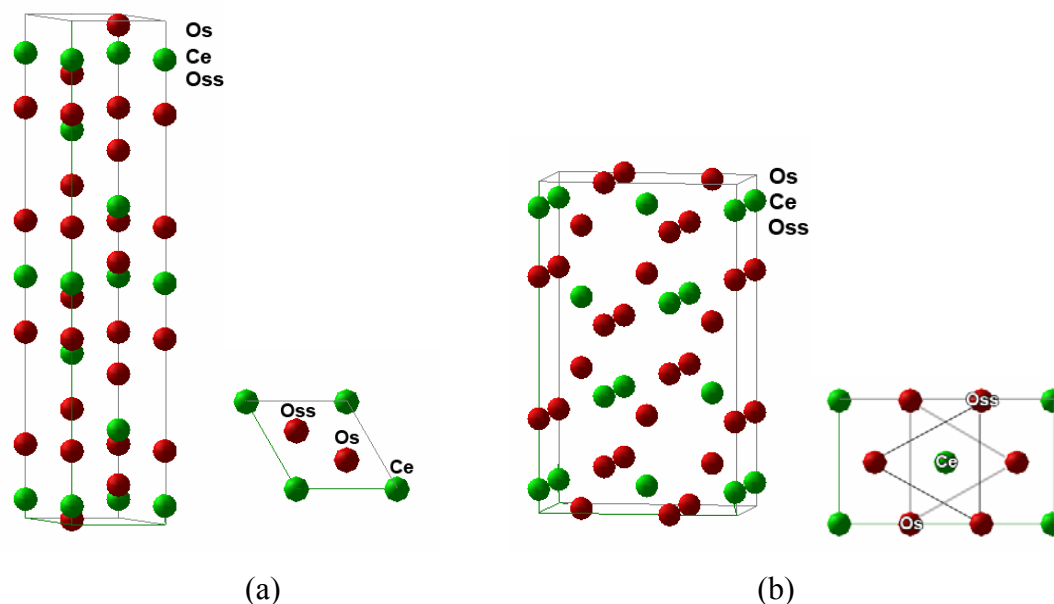


Figure 9 The supercell used in the calculations for CeO₂(111) systems: (a) $p(1\times 1)$ and (b) $p(\sqrt{3}\times 1)$. The corresponding top view of the topmost surface is also shown.

2) The coverage dependence

As for the coverage dependent study, the larger surface areas of models are required. Thus, the $p(1\times 2)$ and $p(\sqrt{3}\times 1)$ lateral cells, consisting of 5 and 12 atomic layers were selected to simulate the (110) and (111) surface systems, respectively. These models were named as CeO₂(110) $p(1\times 2)$ and CeO₂(111) $p(\sqrt{3}\times 1)$. Two and six atomic layers at the bottom of slab models — for (110) and (111) orientations, respectively — were kept fixed to mimic the bulk structure. The remaining unconstrained atomic layers were allowed to fully relax in all directions while the dimensions and shape of the unit cell were kept fixed at the calculated lattice parameter. The vacuum layer thickness of 15 Å was also selected in the systems studied. The corresponding MP k-mesh points of $(8\times 6\times 1)$ and $(6\times 10\times 1)$ were used for CeO₂(110) $p(1\times 2)$ and CeO₂(111) $p(\sqrt{3}\times 1)$, respectively. Since the surface oxygen was predicted to be the most stable adsorption site for both the (110)

and (111), the surface oxygen was selected to simulate for the coverage dependent systems. Two different coverages (1/2 ML and 1ML) of Rh overlayer were explored for both the (110) and (111) surfaces. To ensure the correctness of the models utilized here, we have also explored the adsorption site dependence using these models [CeO₂(110)*p*(1×2) and CeO₂(111)*p*(√3×1)]. It was found that there is a small difference of Rh/CeO₂ interactions between the CeO₂(110)*p*(1×2) and CeO₂(110)*p*(1×1) as well as CeO₂(111)*p*(√3×1) and CeO₂(111)*p*(1×1), as can be seen soon after in the result section.

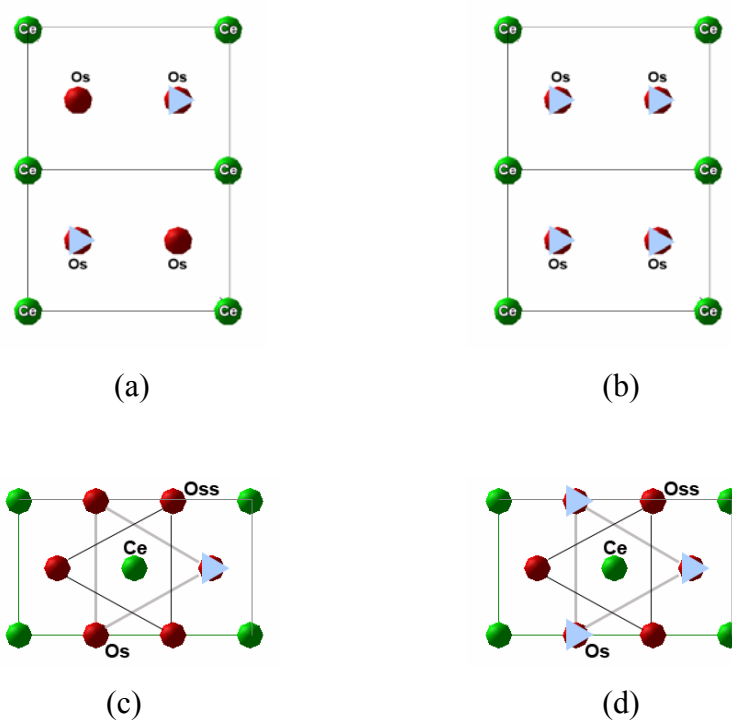


Figure 10 The coverage definition for 1/2 and 1 ML Rh coverage on (a) 1/2 ML CeO₂(110)*p*(1×2), (b) 1 ML CeO₂(110)*p*(1×2), (c) 1/2 ML CeO₂(111)*p*(√3×1) and (d) 1 ML CeO₂(111)*p*(√3×1) systems. The filled color triangles represent Rh atoms.

RESULTS AND DISCUSSION

Chapter I. High coverage effect on proton transfer of faujasite/water system

A series of model clusters of FAU/(H₂O)_n; n = 1, 2, 3, and 4 are investigated using cluster and embedded cluster approaches. The fully optimized geometry structures for all systems are documented in Tables 1-2. The corresponding adsorption energies evaluated by employing different models are given in Table 3.

1. One and two water molecules per acid site

Two representative cluster models of water adsorption on Faujasite zeolites are investigated. In one of these, the hydrogen-bonded structures are stabilized on the Brønsted site. The other is a type of protonated model, in which hydronium ion forms two hydrogen bonds toward the unprotonated zeolite framework. All investigated models yielded only one minimum as hydrogen-bonded physisorbed water complexes, regardless of whether the initial framework structure had H₂O or H₃O⁺. Similar findings to our results have just recently been reported by Sauer et. al. FT-IR (Wakabayashi *et al.*, 1996; Lee *et al.*, 1999) and ab initio (Krossner and Sauer, 1996) studies of water adsorption on zeolite support the direct clear evidence for the hydrogen bonded adsorption of water. Comparing the results between cluster and embedded cluster models, the Madelung potential has the effect of lengthening the O1-H1 bond distance (Brønsted acid site), and hence enhances the acidity of the Brønsted acid site (see Table 1).

Table 1 Structural parameters of the Faujasite/(H₂O)_n systems, n = 1, 2.

Bond (Å) and angle (degree)	FAU/H ₂ O		FAU/(H ₂ O) ₂	
	Bare cluster	Embedded cluster	Bare cluster	Embedded cluster
	neutral	neutral	neutral	neutral
Al-O1	1.952	1.907	1.941	1.890
Al-O2	1.796	1.776	1.793	1.771
Al-O3	1.740	1.744	1.746	1.742
Al-O4	1.724	1.777	1.726	1.781
<Al-O>	1.803	1.801	1.801	1.796
O1-O5	2.523	2.507	2.521	2.494
O1-H1	1.033	1.045	1.043	1.064
O5-H1	1.503	1.468	1.484	1.432
O2-H2	1.689	1.855	-	-
O2-H3	-	-	1.729	1.953
O5-H5	0.967	0.968	0.998	0.968
O5-H2	0.996	0.982	0.967	0.999
O5-O6	-	-	2.634	2.603
O6-H3	-	-	0.986	0.975
O6-H4	-	-	0.965	0.966
∠O1-H1-O5	168.5	172.1	171.9	175.1
∠O2-Al-O1	89.9	93.4	90.2	93.9
∠O5-H5-O7	-	-	-	-
∠O5-H2-O6	-	-	158.8	154.3

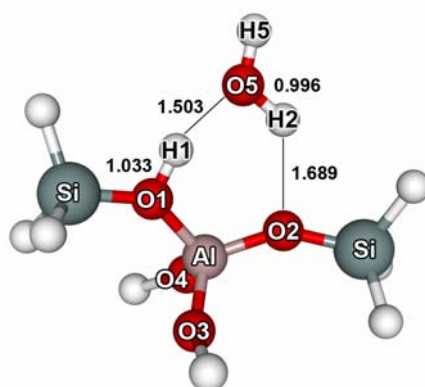
Table 2 Structural parameters of the Faujasite/(H₂O)_n systems, n = 3, 4.

Bond (Å) and angle (degree)	FAU/(H ₂ O) ₃		FAU/(H ₂ O) ₄
	Bare cluster	Embedded cluster	Bare cluster
	neutral	ion-pair	ion-pair
Al-O1	1.937	1.838	1.809
Al-O2	1.794	1.803	1.864
Al-O3	1.748	1.769	1.740
Al-O4	1.736	1.797	1.755
<Al-O>	1.804	1.802	1.792
O1-O5	2.468	2.512	2.726
O1-H1	1.090	1.446	1.813
O5-H1	1.381	1.067	0.987
O2-H3	1.776	1.844	1.417
O5-H5	0.982	0.999	0.984
O5-H2	0.993	1.026	1.441
O5-O6	2.653	2.542	2.480
O6-H3	0.987	0.983	1.069
O6-H4	0.966	0.972	0.996
O7-O5	2.790	2.692	2.759
O6-O8	-	-	2.680
∠O1-H1-O5	173.8	176.2	152.3
∠O2-Al-O1	90.4	95.3	92.9
∠O5-H5-O7	170.1	175.0	166.9
∠O5-H2-O6	160.7	167.2	166.1
∠O6-H4-O8	-	-	172.2

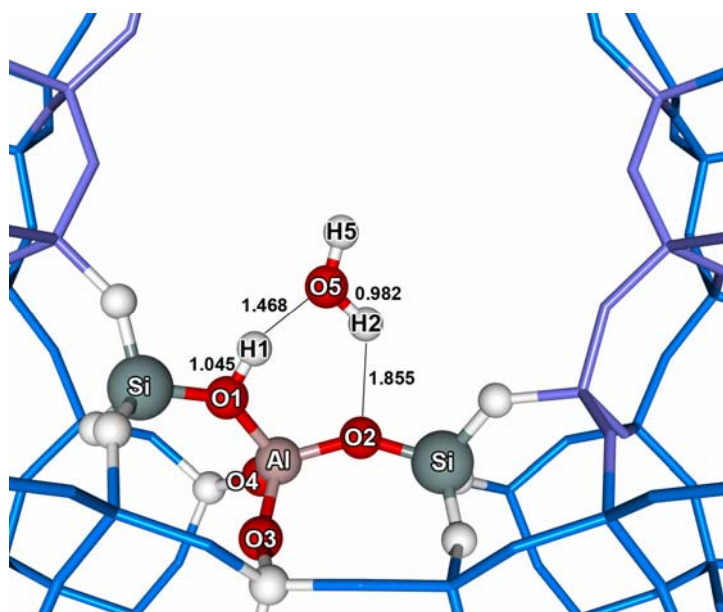
Table 3 Adsorption energies of water clusters on Faujasite zeolite (kcal/mol).

FAU/ (H ₂ O) _n	Bare Cluster				Embedded Cluster			
	NC ^a	IP ^b	B3LYP/6-311+G(d,p) //B3LYP/6-31G(d,p)	NC ^a	IP ^b	B3LYP/6-31G(d,p)	NC ^a	IP ^b
1	-20.92	-	-15.99	-22.41	-	-17.42	-	-
2	-17.02	-	-11.72	-17.52	-	-12.12	-	-
3	-14.14	-	-9.85	-	-19.57	-	-15.02	-
4	-	-13.92	-9.14	-	-	-	-	-

^aNC = neutral complex^bIP = ion-pair complex

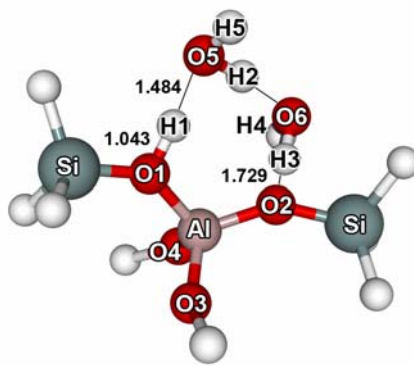


(a)

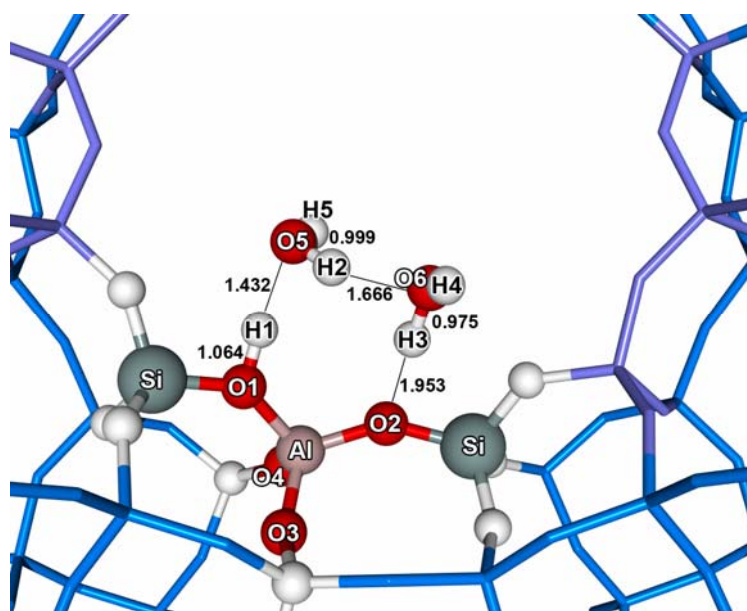


(b)

Figure 11 (a) Cluster and (b) Embedded cluster models of the Faujasite/H₂O system. All values are given in angstroms.

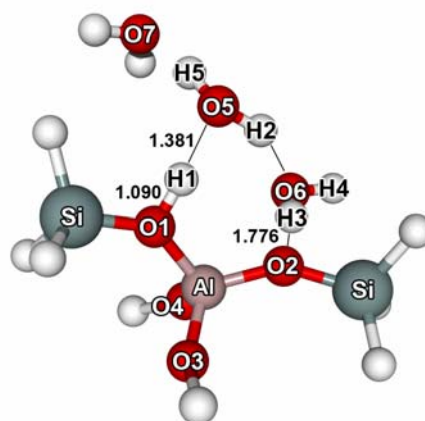


(a)

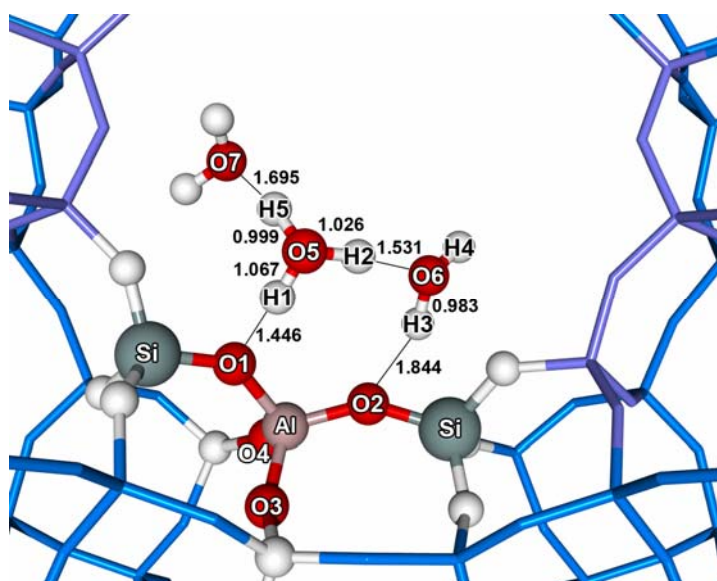


(b)

Figure 12 (a) Cluster and (b) Embedded cluster models of the Faujasite/(H₂O)₂ system. All values are given in angstroms.



(a)



(b)

Figure 13 (a) Cluster and (b) Embedded cluster models of the Faujasite/(H₂O)₃ system. All values are given in angstroms.

The changes in the structural parameters of the zeolite upon complexation with water are minute but impressive. The results are in accordance with Gutmann's rules (Gutmann, 1978), i.e. a lengthening of the bridging O-H bond, a shortening of Al-O adjacent to this bond and a lengthening of Al-O (not adjacent to it). Similar trends are also observed for two water molecules per acid site. The O-H distance in the optimized structure of zeolite/H₂O and zeolite/(H₂O)₂ adducts (Figures 11-12) are evaluated to be 1.033 (1.045) and 1.043 (1.064) Å, respectively. The lengthened O-H distance of the latter model reflects an increase of the binding energy (see Table 3) [-15.99 (-17.42) versus -23.44 (-24.24) kcal/mol; values in parenthesis are those obtained from the embedded cluster calculations]. For cluster models, our findings agree closely with those previously reported. (Zygmunt *et al.*, 1996; Gale, 1996; Rice *et al.*, 1998) on the basis of DFT calculations carried out with a 3T, 4T, or a 5T cluster, respectively.

The calculated adsorption energies and those estimated from the experimental values are different for the case of one adsorbed H₂O molecule but not for the adsorption of a second H₂O molecule. Since the uncertainties in the experimental adsorption energy values are not known (Rice *et al.*, 1998), it is difficult to discuss this further.

Attempts have been made to observe the Z/[H₃O]⁺[H₂O], an initial structure in which a hydronium ion is optimized. The OH bond of H₃O⁺ and the hydrogen bond angle (O-H...O) in the complex is constrained at the optimized H₃O⁺ and 180° respectively. However, during the optimization, the proton of H₃O⁺ is transferred to the zeolite, and the final equilibrium complex H-Z/[H₂O][H₂O] is obtained. The findings obtained from quantum cluster and embedded cluster models are consistent with the literature (Gale, 1996; Rice *et al.*, 1998) that no evidence of proton transfer is observed with either one or two H₂O molecules adsorbed on the zeolitic cluster models. The experimentally observed reduction of adsorption energy per molecule when passing from one to two molecules per site of about 4.06 kcal/mol compares well with our predicted embedded value of 5.3 kcal/mol. We note that differences in

cluster size, method of cluster termination, the presence or absence of structural constraints may contribute to the observed differences in the geometry.

2. Three and four water molecules per acid site

The results derived from the quantum cluster method indicate that the zeolitic proton remains non-transferred in the FAU/(H₂O)_n n = 1-3 until at least four water molecules are solvated around the Brønsted acid site.

For the embedded cluster method, the protonation seems certain when three water molecules are adsorbed on zeolite. It should be noted that there are many deviations between the isolated H₃O⁺ structure and those for H₃O⁺ in the zeolite/water complex. This observation is due mainly to the fact that the hydronium ion is stabilized by interacting with solvating water molecules and the anionic zeolite framework. The acid hydrogen sits 1.446 Å from the zeolitic framework oxygen and 1.067 Å from the oxygen of the H₃O⁺ ion. The oxygen of the hydronium ion is located at 2.512 Å from the acid site oxygen O(1). This calculated H₃O⁺...Oz distance can be compared well with the experimental observation of 2.51 Å for a weaker acid catalyst, silicoaluminosilicate (SAPO) (Smith *et al.*, 1996). The corresponding embedded adsorption energy of the high coverages of adsorption molecule of zeolite, ZO(H₃O⁺)(H₂O)₂ is calculated to be -14.2 kcal/mol at B3LYP/6-31G++(2d,2p) level of theory and compares well with experimental observation.

3. Conclusions

The influence of high coverages of adsorbing molecules on zeolites has been investigated by means of both the density functional theory quantum cluster and the embedded cluster methods. For cluster models, equilibrium structures determined for the adsorbing molecules successively added from one to four molecules per acid site. While $[\text{H}_3\text{SiOAl}(\text{OH})_2\text{SiH}_3]/[\text{H}_2\text{O}]$ and $[\text{H}_3\text{SiOAl}(\text{OH})_2\text{SiH}_3]/[\text{H}_2\text{O}]_2$ are a hydrogen-bonded complex, cluster of $[\text{H}_3\text{SiOAl}(\text{OH})_2\text{SiH}_3]/[\text{H}_2\text{O}]_4$ they contain both types of ion-pair and neutral complexes. The ion-pair complex results from a prompt and complete proton transfer from zeolite to adsorbate that takes place in the high coverages. It is shown that for the zeolite/ $(\text{H}_2\text{O})_3$ complex, a complete proton transfer, $\text{ZO}(\text{H}_3\text{O}^+)(\text{H}_2\text{O})_2$, can be observed when the zeolite lattice potential is taken in to account.

Chapter II. Methanol adsorption on faujasitic petrochemical catalysts

1. Model dependence

1.1 Cluster size effects

The effects of cluster size of the zeolite by using two different cluster sizes, 5T and 7T models, were investigated. The adsorption of a single methanol molecule was studied by means of the bare-quantum cluster approach. Attempts were made to search for the minimum structures using different initial configurations, 5T/[CH₃OH], 5T/[CH₃OH₂]⁺, 7T/CH₃OH, 7T/[CH₃OH₂]⁺. All these cluster models yielded only one minimum as a hydrogen-bonded physisorbed methanol complex regardless of the initial framework structure. The physisorbed complexes were stabilized by two hydrogen-bond interactions, one bound with the acid site proton and another weaker one bound with the adjacent framework oxygen. For 5T model, the corresponding strong hydrogen-bonded (H1-O4) and weaker hydrogen-bonded distances (H2-O2) were calculated to be 1.444 and 1.854 Å, respectively.

As the quantum cluster size increased from 5T to the 7T model, the acidic OH bond distance was increased by 0.017 Å. The cluster size also had the effect of shortening H1-O4 and the H2-O2 distances to 1.402 and 1.829 Å, respectively (cf. Table 4). The stronger hydrogen-bonded interactions of 7T model increased the adsorption energies from -17.17 to -20.48 kcal/mol as compared with the value of the 5T cluster calculation (see Table 5). Our results compare favorably with other theoretical cluster calculations (Greatbanks *et al.*, 1996; Haase and Sauer, 1995; Gale, 1993; Gale, 1996; Blaszkowski and van Santen, 1995), with reported values ranging from -13.81 to -19.76 kcal/mol, depending on the calculation methods and model cluster sizes. Experimental values of the heat of adsorption of methanol in HZSM-5 zeolites are -15.0 (Messow *et al.*, 1984) and -27.38 kcal/mol (reference therein Haase and Sauer, 1995). However, since the uncertainties in the experimental adsorption energy values are not known, it is difficult to further discuss this. We note

that cluster size, method of cluster termination, the presence or absence of structural constraints may contribute to the differences on adsorption energy.

1.2 Effects of the Madelung potential

The effect of the extended zeolite lattice framework is focused in this part of the studies. The zeolite framework effects were represented by including the terms of the Madelung potential. In many recent methanol adsorption studies, most of the cluster models contain only three tetrahedral atoms (3T) and one Si atom which were substituted by one Al atom. All 3T models can describe the adsorption that takes place in each local site, but cannot distinguish the species of a particular zeolite. In our model, the Madelung potential enhanced the acid strength of the zeolitic proton by lengthening the OH bond distance and can differentiate the particular types of zeolite (Limtrakul *et al.*, 2001). Our results obtained from 7T bare cluster models yielded only one minimum as hydrogen-bonded physisorbed methanol complex that is similar to other theoretical calculations. In the embedded cluster approach, however, the methoxonium cation was observed and predicted to be a minimum structure. The chemisorbed methanol has asymmetric OH bond distances of 1.061 and 1.018 Å for the O4-H1 and O4-H2, respectively. These values compared qualitatively well with the values obtained from chabazite systems using the full periodic calculations [1.101 and 1.058 Å (Haase *et al.*, 1997)] and the 8T cluster fragments calculation [1.110 and 1.052 Å (Mihaleva *et al.*, 2001)].

Table 4 Structural parameters of methanol adsorption in Faujasite.

Bond (Å) and angle (degree)	FAU/CH ₃ OH						FAU/(CH ₃ OH) ₂					
	5T			7T			5T			7T		
	Bare cluster		Bare cluster	Embedded cluster		Embedded cluster	Bare cluster		Bare cluster	Embedded cluster		Embedded cluster
	N.C.	I.P.	N.C.	I.P.	N.C.	I.P.	N.C.	I.P.	N.C.	I.P.	N.C.	I.P.
O1-H1	1.054	1.071	1.092	1.429	1.137	1.269	1.438	1.137	1.269	1.137	1.438	
H1-O4	1.444	1.402	1.354	1.061	1.282	1.143	1.051	1.282	1.143	1.282	1.051	
O1-O4	2.471	2.448	2.446	2.434	2.419	2.412	2.485	2.419	2.412	2.419	2.485	
O4-H2	0.986	0.988	0.968	1.018	1.010	1.032	1.054	1.010	1.032	1.010	1.054	
H2-O2	1.854	1.829	-	1.592	-	-	-	-	-	-	-	
O4-O2	2.714	2.684	-	2.528	-	-	-	-	-	-	-	
O4-C1	1.436	1.438	1.458	1.462	1.438	1.444	1.456	1.438	1.444	1.438	1.456	
H2-O5	-	-	-	-	1.581	1.484	1.420	1.581	1.484	1.581	1.420	
O4-O5	-	-	-	-	2.572	2.501	2.462	2.572	2.501	2.572	2.462	
O5-H3	-	-	-	-	0.978	0.981	0.971	0.978	0.981	0.978	0.971	
O5-O3	-	-	-	-	2.820	2.799	2.960	2.820	2.799	2.820	2.960	
H3-O3	-	-	-	-	1.850	1.822	1.994	1.850	1.822	1.850	1.994	
O5-C2	-	-	-	-	1.428	1.432	1.447	1.428	1.432	1.428	1.447	
∠O1-Al-O2	99.7	98.6	94.1	94.2	100.6	99.6	94.5	100.6	99.6	100.6	94.5	
∠O1-H1-O4	162.8	163.4	178.4	156.9	178.1	178.9	174.5	178.1	178.9	178.1	174.5	
∠O4-H2-O2	143.9	142.9	-	150.4	-	-	-	-	-	-	-	
∠O4-H2-O5	-	-	-	-	165.7	167.4	168.4	165.7	167.4	165.7	168.4	

Table 5 Adsorption energies of methanol cluster in Faujasite zeolite (kcal/mol).

Adsorption energies (ΔE , kcal/mol)	FAU/CH ₃ OH				FAU/(CH ₃ OH) ₂			
	5T		7T		5T		7T	
	Bare cluster	Bare cluster	Embedded cluster	Embedded cluster	Bare cluster	Bare cluster	Embedded cluster	Embedded cluster
B3LYP/6-31G(d,p)	N.C.	N.C.	N.C.	N.C.	N.C.	N.C.	I.P.	I.P.
	-23.82	-24.86	-23.34	-28.41	-19.22	-19.52	-23.57	-23.57
Mixed basis set*								
[B3LYP/6-311+G(3df,2p) :B3LYP/6-31G(d,p)]	-	-23.87	-20.07	-23.36	-	-17.25	-19.46	-19.46
BSSE	-	-20.57	-19.27	-24.34	-	-14.56	-18.84	-18.84
B3LYP/6-311+G(3df,2p) //B3LYP/6-31G(d,p)	-17.17	-20.48	-17.05	-21.07	-25.71	-14.10	-17.95	-17.95

*see text

1.3 Effects of basis set

The effects of basis set in our calculations have also been studied by performing the single point calculation at B3LYP/6-311+G(3df,2p) and using the counterpoise method to estimate the BSSE correction at B3LYP/6-31G(d,p) level of theory. The corresponding adsorption energies of each system are documented in Table 5. As a result, the BSSE correction showed quite similar values of adsorption energies to those with the high basis set correction. In the embedded cluster model, obtained from BSSE calculations the differences of these values were within 3 kcal/mol. These effects might be affected by the Madelung potentials or the large orbital in the single point calculation. In addition, the effects of artificial capped atoms (H) to the adsorption energies were demonstrated. The Mixed-basis set was used to investigate this point. Two types of basis set, 6-311+G(3df,2p) and 6-31G(d,p) were used, the latter was used for the terminated H atoms and the former was used for the remaining atoms of the systems. From the single methanol adsorption system, these energies were found to agree favorably with the results obtained from BSSE corrections, except for the adsorption energies of the two methanol system in the bare cluster calculation. As a result, the adsorption energy obtained from the counterpoise calculations are compared well with that of at high basis set.

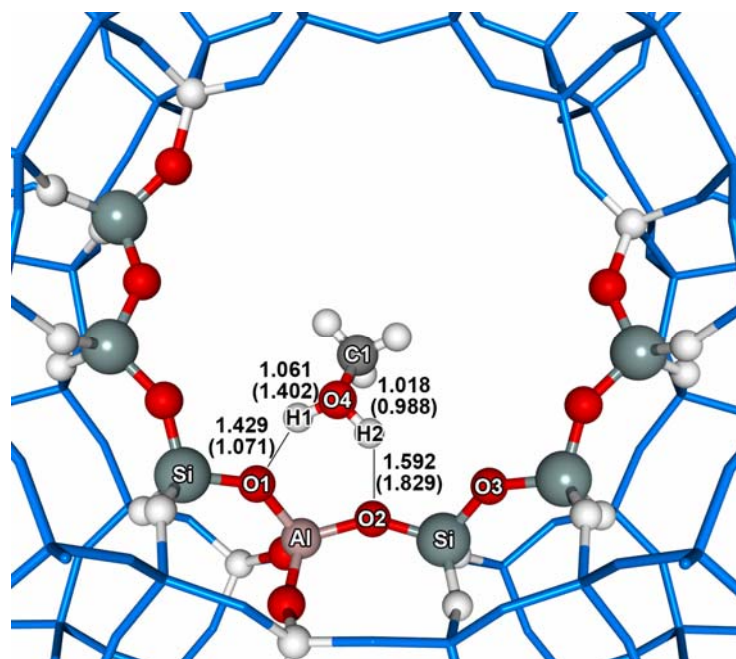
2. Mode of adsorption

In this part, we mainly discuss the best model of our study, the 7T embedded cluster of the methanol adsorption system. We focus on the mode of adsorption and the effects of the number of coverage molecules.

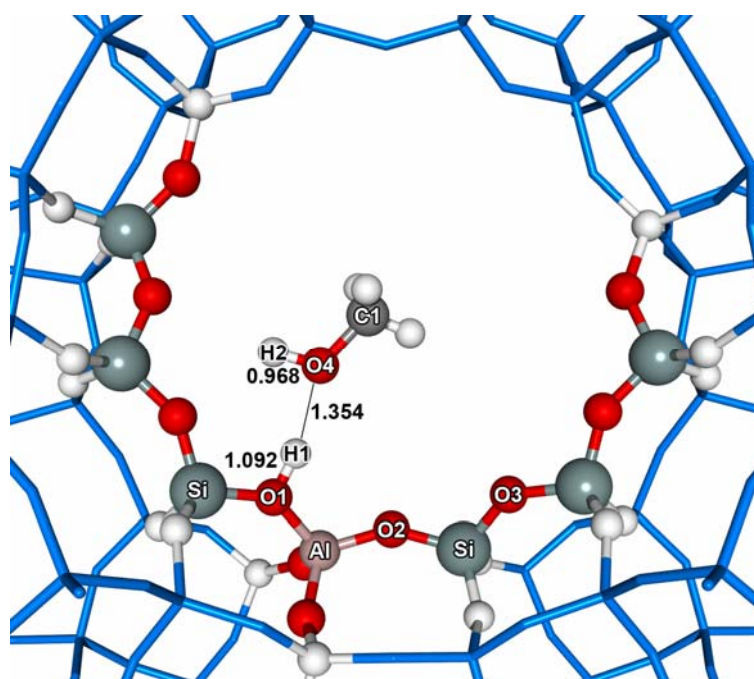
2.1 Low coverage

Using the embedded cluster approach, the fully optimized structural parameters of the single methanol adsorption in Faujasite zeolite were summarized in Table 4 and illustrated in Figure 14. Two types of equilibrium structure, methoxonium cation and neutral methanol complexes, were observed and showed similar results to previous studies (Haase *et al.*, 1997; Mihaleva *et al.*, 2001; Shah *et al.*, 1996a). However, the methoxonium cation was found to be a more favorable structure than the physisorbed methanol complex by 4 kcal/mol and was not predicted to be a transition state for the hydrogen exchanged reaction that was reported by recent theoretical study (Haase and Sauer, 1995; Gale *et al.*, 1993). The stable methoxonium cation was stabilized by the strong ionic interaction between asymmetric OH bond distances and the anionic deprotonated framework. It should be noted that there are significant structural deviations between the isolated CH_3OH_2^+ and those for CH_3OH_2^+ in the Faujasite/methanol system. These differences are due mainly to the fact that the methoxonium cation is stabilized by interacting with the anionic framework (Boronat *et al.*, 2001).

On the other hand, the physisorbed methanol complex was observed only when the adsorption took place at the adjacent Si site (see Figure 14b) and was stabilized by two hydrogen-bond interactions, forming one strong hydrogen bond with the acid site proton and a weaker bond with the adjacent framework oxygen, which is similar to that observed by recently studied (Shah *et al.*, 1996a). The corresponding adsorption energies for the physisorbed and chemisorbed complexes were calculated to be -17.05 and -21.07 kcal/mol respectively and comparable to literature [-17.38 and -19.52 kcal/mol (Shah *et al.*, 1996a)] derived from the full periodic density functional methodology on chabazite zeolite and the experimental values of the heat of adsorption of methanol in HZSM-5 zeolite are -15.0 and -27.38 kcal/mol.



(a)



(b)

Figure 14 Modes of adsorption: a) chemisorbed, and b) physisorbed complexes. Values in parenthesis are represented the configurations obtained from bare cluster calculation.

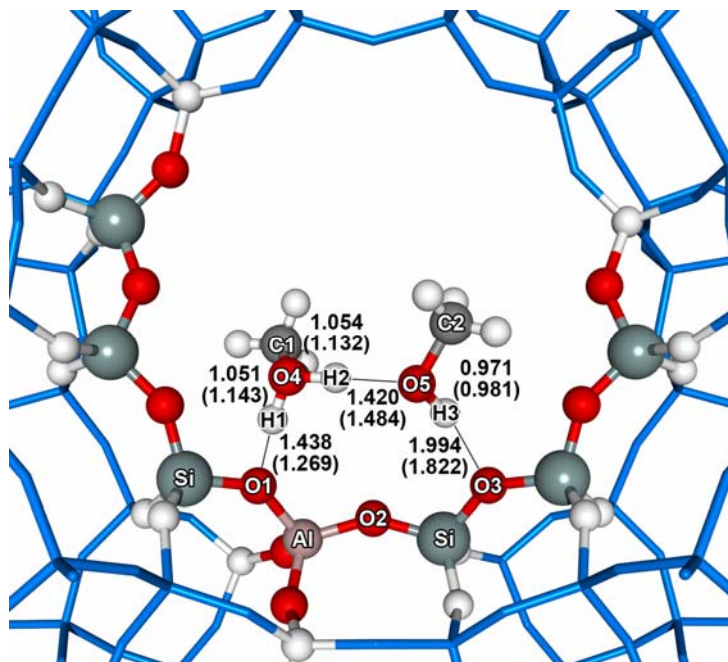


Figure 15 Methanol adsorption in embedded 7T-FAU/[CH₃OH]₂ system. Values in parenthesis are represented the configurations obtained from bare cluster calculation.

2.2 High coverage

The high coverage of two methanol molecules per Brønsted acid site was also investigated (see Figure 15) and similar findings were observed, i.e., the chemisorbed methanol complex was predicted to be the more favorable structure. One of the methanol molecules became a methoxonium cation, which was stabilized by a strong ionic interaction with the deprotonated zeolite and a strong hydrogen-bonded interaction with the second methanol molecule. In this case, high coverage molecules have a significant role on the H-bonded dimers. The second methanol showed a strong influence on the H-bonded dimers by forming an eight-membered ring hydrogen-bonded to enhance the system stability. This was better than the six-membered ring formed in the single adsorbed methanol (Gale, 1996). Our studies agreed favorably with the results reported in the literature (Gale, 1996; Sinclair *et al.*, 1996), which reported that the second methanol molecule was expected to increase the probability of proton transfer in the methanol adsorption system and reduce the activation energy for the methyl oxonium ion mechanism respectively in comparison to the single methanol system respectively. As a result, the adsorption energy was calculated to be -14.10 kcal/mol and was reasonably in agreement with the recent results obtained from 3T (Limtrakul, 1995) and 4T (Gale, 1996) cluster fragments calculations of -10.95 and -14.18 kcal/mol, respectively.

3 Vibrational frequency analysis

The calculations of the harmonic vibrational frequencies at the B3LYP/6-31G(d,p) level of theory for chemisorbed and physisorbed methanol complex are listed in Table 6 and Table 7, respectively.

Experimentally (Mirth *et al.*, 1990; Zecchina *et al.*, 1996b; Kotrla *et al.*, 1998), three broad bands are observed in range of 2900-2700 cm^{-1} , 2440-2360 cm^{-1} and 1730-1680 cm^{-1} , which is represented as an ABC triplet for asymmetric stretching modes of short, long OH bonds and HOH bending modes of methoxonium cation, respectively. For the protonated methanol complex, the asymmetric stretching modes of methoxonium OH bonds were calculated to be 2970 and 2314 cm^{-1} , respectively and compared well with the IR (Mirth *et al.*, 1990) spectra obtained experimentally from chemisorbed methanol complexes. The splitting of 656 cm^{-1} is significantly larger than the value of 400 cm^{-1} from the experimental result, but similar to the values reported in the chabazite zeolite system (Shah *et al.*, 1996a; Mihaleva *et al.*, 2001). The methyl group of methoxonium cation is bound directly toward the framework oxygen adjacent to the aluminum site with OH_2^+ moiety. Our calculations indicated that the methoxonium OH stretch modes were slightly higher than the calculations from the small unit cell zeolite (Shah *et al.*, 1996a; Mihaleva *et al.*, 2001) and close to the experimental data. This means that the extended framework and the topology of the zeolite environment play a significant role in stabilizing the methoxonium cation. The bending mode of the methoxonium cation at 1743 cm^{-1} agrees favorably with other results obtained theoretically and experimentally. The second configuration, physisorbed methanol, has not been observed directly in our study. Attempting to demonstrate this configuration, some parameters of the methanol molecule were constrained as shown in Figure 14b. The stretching modes of Brønsted OH and methanol hydroxyl were calculated to be 1814 and 3816 cm^{-1} , respectively. The methanol hydroxyl mode was comparable with the recent study using the 8T cluster (Mihaleva *et al.*, 2001) and showed a lower wave number as compared to the other small cluster system (Haase and Sauer, 1995; Gale, 1993; Blaszkowski and van Santen, 1995). However, the OH stretch mode of the Brønsted site was observed in a

longer wave number than the other calculations due to the constraint of some parameters and the weak interaction of the adjacent zeolite framework as compared to the acid site. The OH bending modes (1558, 1351 and 1094 cm^{-1}) and CH stretching modes (3223, 3158 and 3073 cm^{-1}) indicated quite identical results to those reported in other theoretical studies (Haase and Sauer, 1995; Gale, 1993; Blaszkowski and van Santen, 1995; Mihaleva *et al.*, 2001). Additionally, the observation band at 978 cm^{-1} was attributed to the CO stretching mode and showed the same trend as that compared with the band that was observed in the chemisorbed system, a slightly red-shift wave number. It is found that the methyl group seemed to be largely unaffected by the zeolite environment, and the stretching CH modes reported were consistent with the experimental data of the methanol molecule (Hehre *et al.*, 1986).

Table 6 Vibrational frequencies (cm^{-1}) of the chemisorbed adsorption modes.

Vibrational frequency mode (cm^{-1})	This work (FAU)	Shah <i>et al.</i> ^a (CHA)	Mihaleva <i>et. al.</i> ^b (CHA)	Expt. ^c (ZSM-5)
OH stretch	2970	2757	2716	2900
	2314	2009	2004	2440
HOH bend	1743	1583	1696	1687
CO stretch	998	1015	1030	-
CH stretch	3207	3120	-	2993
	3187	3090	-	2958
	3088	3000	-	1856

^aShah *et al.*, 1996a

^bMihaleva *et al.*, 2001

^cMirth *et al.*, 1990; Zecchina *et al.*, 1996b; Kortrla *et al.*, 1998

Table 7 Vibrational frequencies (cm^{-1}) of the physisorbed adsorption modes.

Vibrational frequency mode (cm^{-1})	This work	Haase <i>et al.</i> ^a	Gale <i>et al.</i> ^b	Blaszkowski <i>et al.</i> ^c	Mihaleva <i>et al.</i> ^d
OH stretch	3816	3276	2963	3237	3669
	1814	2548	2378	2398	2358
OH bend	1558	1421	1392	1496	1508
	1351	1353	-	1372	1370
	1094	1015	-	1055	1063
CO stretch	978	1049	-	-	1032
CH stretch	3223	3084	3167	3086	-
	3158	3043	3088	3054	-
	3073	2948	3046	1972	-

^aHaase and Sauer, 1995: 3T cluster at MP2 level

^bGale *et al.*, 1993: 3T cluster at NLSD approximation

^cBlaszkowski and van Santen, 1995: 3T cluster at NLSCF level

^dMihaleva *et al.*, 2001: 8T CHA cluster at B3LYP/6-31G**

4. Conclusions

Two types of adsorption complexes have been observed, physisorbed and chemisorbed complexes. The results obtained from the density functional theory quantum cluster of [5T-FAU/CH₃OH] and [7T-FAU/CH₃OH] systems indicated the hydrogen-bonded complexes are the preferred structure. Increasing the quantum cluster size from the 5T to the 7T model has the effect of lengthening the acidic OH bond distance and shortening the intermolecular interaction distances (H1...O4 and the H2...O2) which increase the adsorption energies from -17.17 to -20.48 kcal/mol. The chemisorbed structure for the single methanol adsorption complexes on Faujasite are only observed when the Madelung potential is taken into account. The corresponding adsorption energy of the chemisorbed complex is predicted to be -21.07 kcal/mol at B3LYP/6-311+G(3df,2p)//B3LYP/6-31G(d,p) level of theory which is in good agreement with the full periodic DFT results (-19.52 kcal/mol for chabazite zeolite). The physisorbed methanol complex was also observed only when the adsorption took place at the adjacent Si site (see Figure 14b) and stabilized by a very strong hydrogen-bonded interaction between the zeolitic proton and the methanol oxygen atom.

It is found that the second methanol molecule enhances the capability of the proton transfer to the first adsorbed methanol molecule. The second methanol investigated had a strong influence on the H-bonded dimers of FAU/[CH₃OH]₂ by lengthening the Brønsted OH bond distance (O1-H1), shortening the H1-O4 bond distance and increasing hydrogen-bonded angles close to the ideal strong hydrogen-bonded interaction (180 degree). The chemisorbed methanol complexes are observed in this high coverage system both the quantum and embedded cluster calculations. The calculations of the harmonic vibrational frequencies for chemisorbed and physisorbed methanol complex were investigated. For the protonated methanol system, the asymmetric stretching modes of methoxonium OH bonds and the HOH bending were calculated to be 2970, 2314 and 1743 cm⁻¹, respectively. These bands compared favorably with the IR spectra obtained experimentally from chemisorbed methanol complexes. These findings showed a significant influence on the cluster size

and the number of loading molecules. Finally, it is concluded that the local structure of the active site, $\equiv\text{Si-OH-Al}\equiv$, is not only sensitive to the high coverage but also to the quantum cluster size and the inclusion of the Madelung potential.

Chapter III. Structural and Electronic Properties of Rh/MgO(001) Systems

1. Bulk MgO and bulk Rh - reference systems

Optimization of the bulk MgO gave a lattice constant of 4.25 Å, in reasonable agreement with experimental data [4.21 Å (Wyckoff, 1964)]. As for Rh, the calculated lattice constant was found to be 3.85 Å which, again, reasonably agreed with the value obtained from experiment [3.80 Å (Singh, 1968)]. Our results suggest that the GGA + PAW approach used here, in combination with the cut-off energy and other computational parameters set in the current calculations, may be a suitable method to study the Rh/MgO(001) interface system.

The density of states (DOS) of bulk MgO and bulk Rh, obtained from spin-polarized calculations, are shown in Figures 16 and 17, respectively. The DOS plots for MgO are in good agreement with literature (Baltache *et al.*, 2004; Pandey *et al.*, 1991; Schönberger and Aryasetiawan, 1995). The O 2s states appear at 15.7 eV below the top of the valence band, comparing well with the values reported in literatures [17.1 (Baltache *et al.*, 2004), 15.5 (Schönberger and Aryasetiawan, 1995) eV]. The Mg s states and O p states appear in the conduction band region whereas the lowest unoccupied atomic orbital is contributed to 3p states. Our calculated energy gap is 5.32 eV which agrees well with both theoretical and experimental values reported in the literature. The theoretical values lie in the range between 4.36 to 8.21 eV (Baltache *et al.*, 2004; Pandey *et al.*, 1991; Schönberger and Aryasetiawan, 1995), while the experimental values obtained from photoemission data (Bortz *et al.*, 1990) and from thermoreflectance spectra (Whited *et al.*, 1973) are 6.7 and 7.8 eV, respectively. As for Rh bulk, four dominant peaks can be observed which are similar to the features reported in literature (Eichler *et al.*, 1996). The d states show the major contributions to the TDOS curve below the Fermi level which is in good agreement with the large d states bandwidths reported for 4d and 5d transition metals (Kirsch and Harris, 2004). It can be observed that only small features of s states and d states appear both above and below the Fermi level (Figure 17).

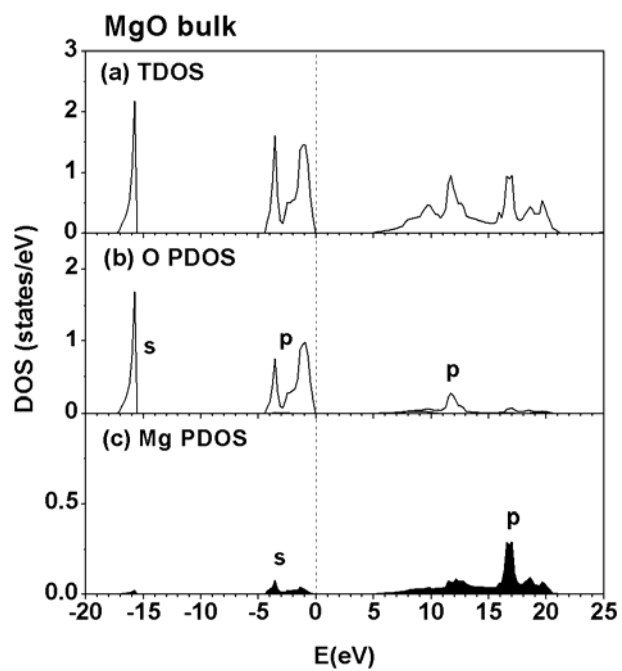


Figure 16 The density of states for the MgO bulk system; TDOS of MgO (a) and PDOS of O (b) and Mg (c).

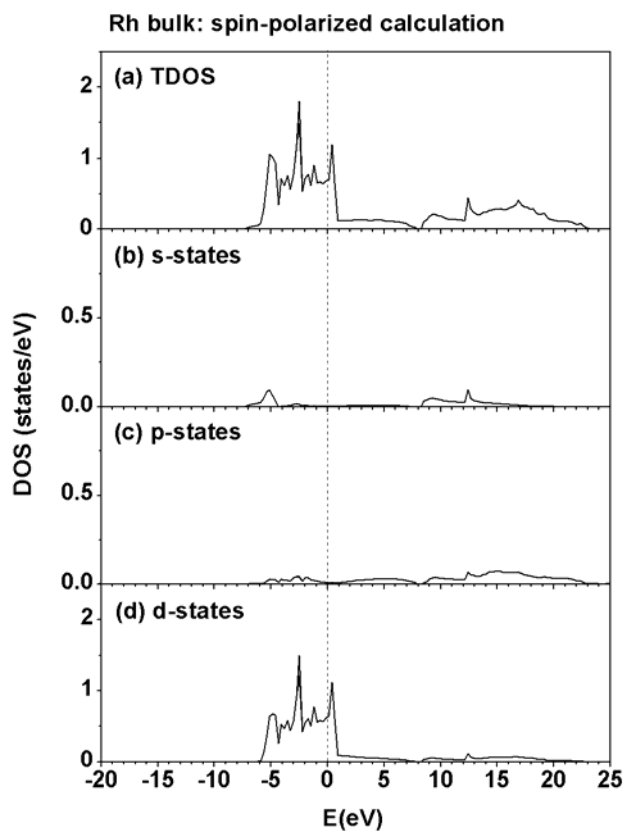


Figure 17 TDOS and PDOS of Rh bulk. The s , p and d states of Rh are shown in (a), (b) and (c), respectively.

2. The clean MgO(001) surface - a reference system

The clean MgO(001) surface exhibits a small relaxation compared to the ideally terminated bulk structure. The resulting surface rumpling for the 8-layer slab is such that, in the outermost layer, O atoms moved outward from the ‘ideal’ surface by about 0.014 Å, whereas Mg moved inward by 0.037 Å. which mean that the oxygen atom center lies “outside” the cation by 0.05 Å (or 2.4 % of the bulk interlayer distance). This structural feature is referred to as “buckling” (see Figure 18). These values are in good agreement with the experimental studies (Rieder, 1982; Urano *et al.*, 1983; Nakamatsu *et al.*, 1988).

The surface energies are reported in our study to investigate the surface stability, the more stable surface the lower the surface energy. The surface energy (E_{surf}) can be calculated by

$$E_{surf} = \frac{1}{2S}(E_{slab} - E_{bulk})$$

where E_{slab} is the total energy for the slab model, E_{bulk} is the energy of bulk system consisting of the same number of atoms as in the slab model and S is the surface area of the slab model.

Our surface energy was calculated to be 0.89 J/m², approximately 0.2 J/m² lower than the experimental values reported in the literature, 1.04 (Jura and Garland, 1952) and 1.12 (Tosi, 1964) J/m², whereas theoretical values in literature lie in the range of 0.98 – 1.53 J/m² (Tasker and Duffy, 1984; Watson *et al.*, 1996; Goniakowski and Noguera, 1995; Causa *et al.*, 1986; Birkenheuer *et al.*, 1994; Evarestov and Bandura, 2004). The total density of states (TDOS) and layer-projected density of states (LPDOS) of MgO clean surface can be seen from Figures 19b-19f. The TDOS shows quite similar features compared to MgO bulk. Figure 19c shows the LPDOS of the surface layer which is shown somewhat differently to the TDOS bulk system, this can be explained by the structural relaxation of the topmost layer. The more bulk-like

behaviors are clearly seen from the sub-surfaces to the center of the slab (Figures 19d-19f), which confirm that the four-layer slab is sufficient to investigate the interaction of Rh/MgO(001) interface system as mentioned previously (Nokbin *et al.*, 2004). For the MgO(001) surface, the energy band gap is reduced from the bulk value to 3.41 eV, which is rather small compared to the literature value of 6.2 eV (Henrich *et al.*, 1980; Cox and Williams, 1986).

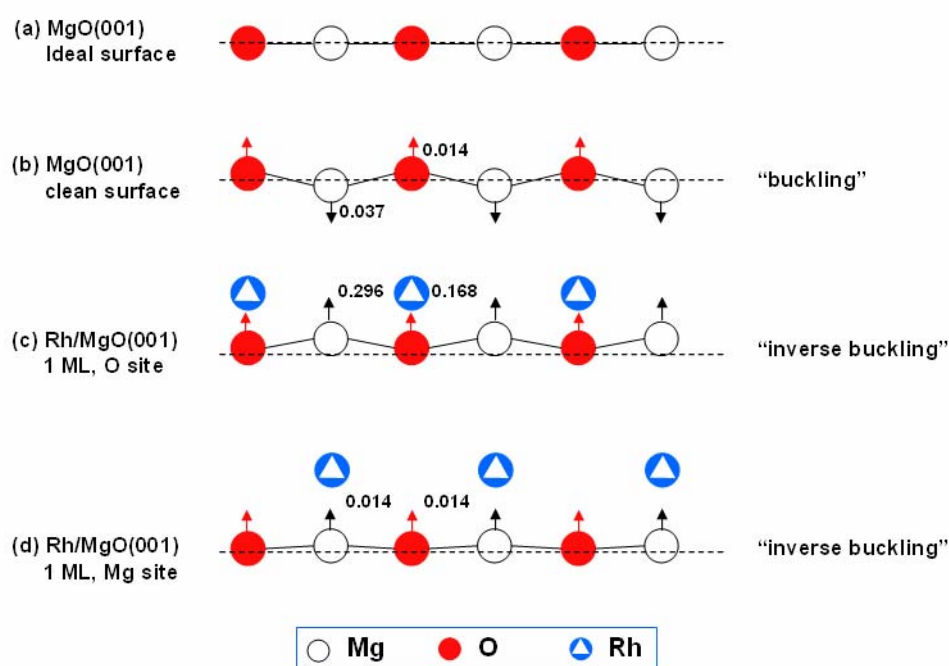


Figure 18 The structural relaxations for the clean surface of MgO(001) and the Rh/MgO(001) systems: (a) ideal clean surface, (b) optimized clean surface, (c) 1 ML Rh/MgO(001) for the O site and (d) 1 ML Rh/MgO(001) for the Mg site.

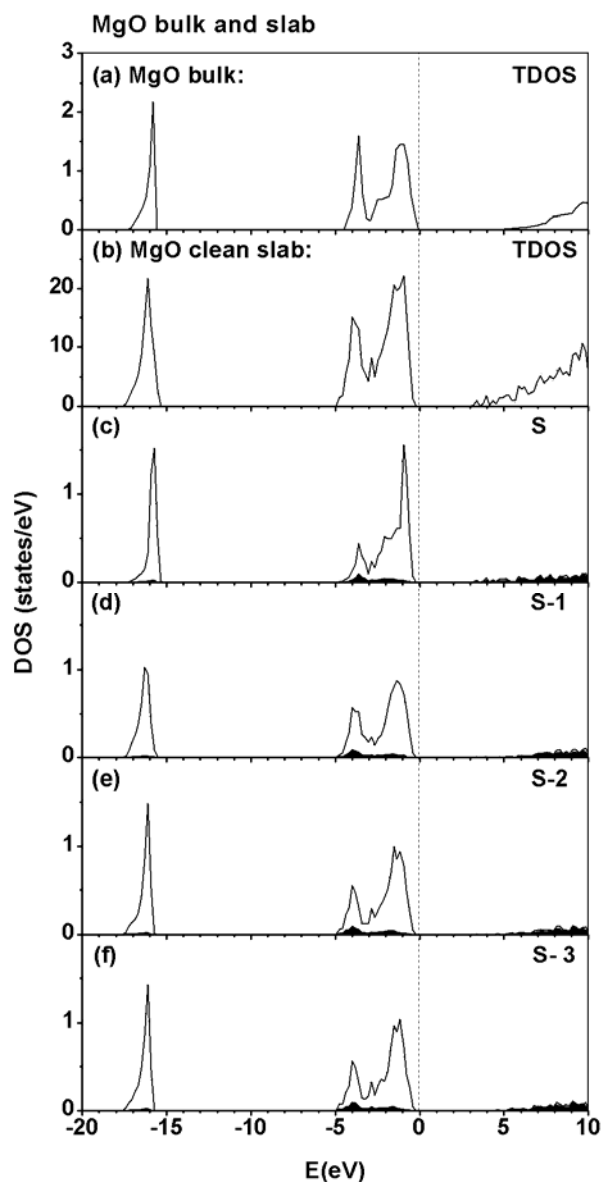


Figure 19 TDOS and LPDOS of the 8-layer MgO(001) slab. White and black areas represent LPDOS of O and Mg, respectively. The TDOS for bulk MgO is included for reference. “S”, “S-1”,..., and “S-3” represent the surface layer, the sub-surface layer,..., and the center layer of the slab, respectively.

3. The Rh/MgO(001) systems

3.1 Structure

The atomic positions of the Rh/MgO(001) system were fully optimized for three different coverages (1/8, 1/2 and 1 ML) of Rh over three different adsorption sites (on top of O, Mg and hollow). The optimized Rh-surface distances are reported in Table 8.

An “*inverse buckling*” (inverse rumpling) of the oxide surface when a Rh overlayer was placed either on top of O or Mg atoms compared to the relaxed clean surface structure that was found (see Figure 18c-18d). The O and Mg atoms on the topmost layer lie outward from the surface which is not similar to the observation of a clean surface as mentioned in the previous section. The more outward displacements of O and Mg atoms can be seen in the case of 1 ML coverage, when Rh atoms were placed epitaxially on top of surface O, the Mg atoms on the surface were displaced more outward from the surface than O atoms by approximately 0.13 Å, this inverse rumpling behavior is in agreement with the optimized structures reported by Wu et al. (Wu and Freeman, 1995). In the case of the Mg adsorption site, a small inverse rumpling was observed in which Mg atoms lie more outward by than O atoms by less than 0.005 Å. At the 1/2 ML coverage, the same rumpling behaviors can be observed for both O and Mg adsorption sites, the corresponding displacement values are 0.013 and 0.002 Å, respectively, and show quite smaller values compared to that of the 1 ML cases.

Table 8 Interaction energies per Rh atom (in eV) and vertical Rh-surface distance (in Å) for the optimized Rh/MgO(001) system at different Rh coverages. The adhesion energy (E_{adh}) is the energy gained when the pre-formed Rh layer adheres to the MgO slab and the adsorption energy (E_{ads}) also includes the energy gained when the Rh-layer is formed from Rh atoms (E_{form}).

Coverage	Adsorption site							
	O			Mg				
	R	E_{form}	E_{adh}	E_{ads}	R	E_{form}	E_{adh}	E_{ads}
			E_{form}	E_{adh}	E_{ads}			
1/8 ML								
Non-Spin	1.99	0.00	2.05	2.05	1.80	0.00	1.91	1.91
Spin	2.00	0.00	1.98	1.98	1.93	0.54	1.18	1.72
1/2 ML								
Non-Spin	2.07	0.55	1.69	2.24	1.96	0.61	1.16	1.77
Spin	2.10	0.61	1.50	2.11	1.96	0.61	1.16	1.77
1 ML								
Non-Spin	2.10	2.88	1.12	4.00	2.45	2.88	0.35	3.23
Spin	2.10	2.86	0.94	3.80	2.52	2.86	0.28	3.14

$E_{\text{ads}} = E_{\text{form}} + E_{\text{adh}}$, where $E_{\text{ads}} = -\Delta E_{\text{adsorption-of-atoms}}$, $E_{\text{form}} = -\Delta E_{\text{formation-of-Rh-layer}}$ and $E_{\text{adh}} = -\Delta E_{\text{adhesion-of-Rh-layer}}$ (see text).

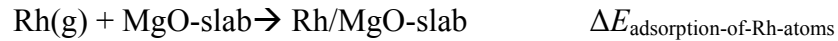
3.2 Adsorption energy

In order to study the interaction energies of the Rh/MgO interface system, the effect of Rh coverage to the system studied is essentially addressed in the discussion. The interaction energies related are defined as described below:

The formation of the metal/oxide interface, $\text{Rh(g)} + \text{MgO-slab} \rightarrow \text{Rh/MgO-slab}$, can be defined as a stepwise process according to:



(3) *Sum of adsorption processes 1 and 2:*



Here the MgO slabs are considered as an existing system. Thus, only the adsorption of Rh in processes (1)-(3) are determined. Hence, first the isolated metal atoms combine to form a metal layer of desired sparseness (here 1/8, 1/2 and 1 ML) in process (1) and the layer deposits on the MgO slab surface in process (2). When the same geometry is used in (1) and (2), then the total adsorption process of Rh atoms on a MgO surface in process (3) is identical to the sum of (1) and (2). Energies (2) and (3) are commonly presented in the literature and are then conventionally given as positive numbers and without the Δ sign. The same conventional representatives will also be stated in terms of E_{adh} , E_{ads} and E_{form} defined as: $E_{\text{adh}} = -\Delta E_{\text{adhesion-of-Rh-layer}}$, $E_{\text{ads}} = -\Delta E_{\text{adsorption-of-Rh-atoms}}$, and $E_{\text{form}} = -\Delta E_{\text{formation-of-Rh-layer}}$, respectively.

The adsorption energy, adhesion energy and energy of metal formation of Rh/MgO interaction at different adsorption sites with different coverages are summarized in Table 8. It is noted that all of the values mainly reported in text

obtained from spin-polarized calculations. The $\Delta E_{\text{formation-of-Rh-layer}}$ shows constant values for each coverage and is seen to be increased by coverage from less than 0.001 eV for 1/8 ML, equal to 0.61 eV for 1/2 ML and 2.86 eV for 1 ML which is referred to as the Rh layer itself is stabilized by the increasing of the number of Rh coverages and the Rh-Rh interactions.

From our results, of all different coverages, the O site is predicted to be the most preferable adsorption site reported for both the adsorption and adhesion energies. The adhesion energy is found to decrease as the number of coverage; 1.98, 1.50 and 0.94 for 1/8, 1/2 and 1 ML coverage, respectively. The adsorption energy, however, is increased as a function of coverage as well as the metal-metal interaction energy as shown from 1.98, 2.11 and 3.80 eV for 1/8, 1/2 and 1 ML coverage, respectively (see Figure 20 and Table 8).

The results at the most stable O site compared to the other literatures are summarized here. At low coverage 1/8 ML, the calculated E_{adh} is 1.98 eV and gives very similar results to low-coverage studies, i.e. 1.82 eV (1/8 ML) (Stirling *et al.*, 1997) and 1.93 eV (1/18 ML) (Bogicevic and Jennison, 2002). In case of 1/2 ML, to the best of our knowledge, there is no reported value available. As for 1ML, our result 0.94 eV reasonably agrees with the 0.84 eV reported in the literature (Wu and Freeman, 1995).

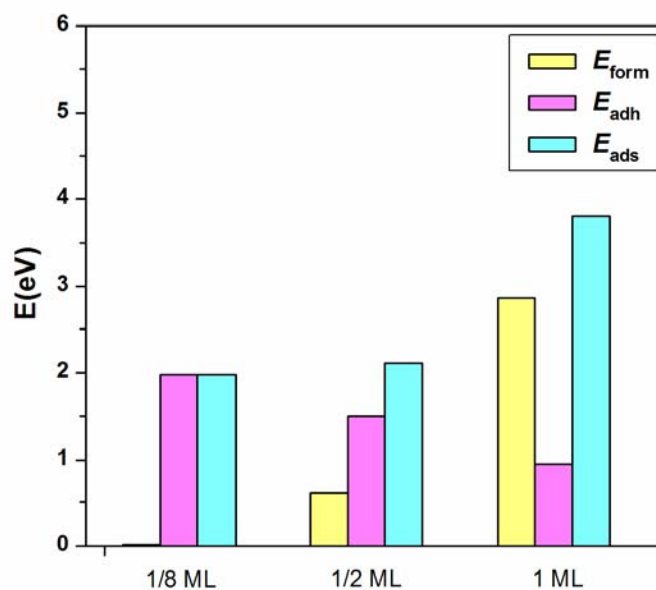


Figure 20 An interaction energetic chart for the Rh/MgO(001) interface system for the O adsorption site as a function of coverages.

As for the other adsorption sites, the hollow site is shown to be a fairly good adsorption site, whereas the Mg site is not. It is mentioned here that the spin polarized calculations for 1/8 ML coverage at the Mg and the hollow sites were neglected since it will not be a main part of discussion and the small changes of such results compared to non-spin polarized ones are expected. The results show that the weakest interactions at the Mg site are both the weaker interaction energies and the longer Rh...Mg distances compared to the other sites. However, the trends of E_{ads} and E_{adh} , depending on the number of coverages, are similar to the observations reported before for the O site.

3.3 Electron density difference

In order to identify interaction bonding behaviors, correlated to interaction energies, the charge density distributions for the Rh/MgO(001) system were calculated and illustrated as the quantity plotted, namely, “electron density difference” to clarify bonding characters. The electron density difference is obtained from $\Delta\rho(\mathbf{r}) = \rho_{\text{Rh/MgO}}(\mathbf{r}) - [\rho_{\text{Rh-layer}}(\mathbf{r}) + \rho_{\text{MgO-slab}}(\mathbf{r})]$, which is the electron redistribution occurring when an isolated Rh layer and an isolated MgO slab combine to form the interface system. Figure 21 shows the plots of $\Delta\rho$ obtained from spin-polarized calculations for 1/8, 1/2 and 1 ML coverage at the O site. As for 1 ML case, a strong electron rearrangement induced by Rh to the surface was found. Obviously, electron density accumulates at Rh and surface O while in the interstitial region electrons are depleted and “spill over” to the region above the Mg, giving more stabilizing effect. This can be explained as the coulomb repulsive interaction which is induced by the “*inverse buckling*” behavior at the topmost surface in this system. However, one can see some influences of Rh to the MgO sub-surface layers which are decreased by the depth of surface. As expected, at 1/2 and 1/8 ML, the quite similar features of electron contributions at the topmost surface were observed for all cases. However, the lower Rh coverage obviously shows a small effect to the sub-surface layers.

As for the other sites (Figure 22), at the Mg site, less electron density contributions on the surface were related to less stabilization of interaction energies as compared to the O site. The electrons gained in the inter-region between Rh and Mg which enhance the strong repulsive interaction and push the Rh and Mg far away from each other as shown by the long Rh...Mg distances. In the surface slab, small features, for this contour level, were observed due to the small effect of Rh to the oxide substrate. The coverage dependence effects are similar to the discussion of those O sites. Owing to the fact that more electrons polarized in the region between Rh and Mg atoms, one might expect the existence of a covalent bond between Rh and Mg because such features are not clearly demonstrated using the plots here. Thus, the bonding characters of Rh and Mg will be discussed in greater details later in the “electron localization function, (ELF)” section.

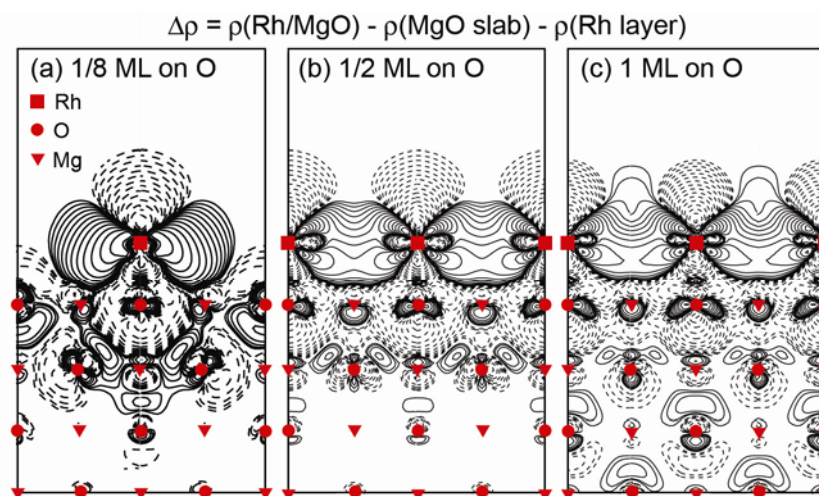


Figure 21 Electron density difference plots for the optimized interface system when Rh binds over surface O for difference coverages. Solid and dashed contour lines represent electron excess and electron loss, respectively. The contour lines start at $\pm 0.0005 \text{ e/a.u.}^3$, increasing by a factor of $10^{0.2}$ for every contour line, i.e. the contours are at ± 0.0005 , ± 0.0008 , ± 0.0012 , ± 0.0020 , ± 0.0031 , ± 0.0050 , ... e/a.u.^3

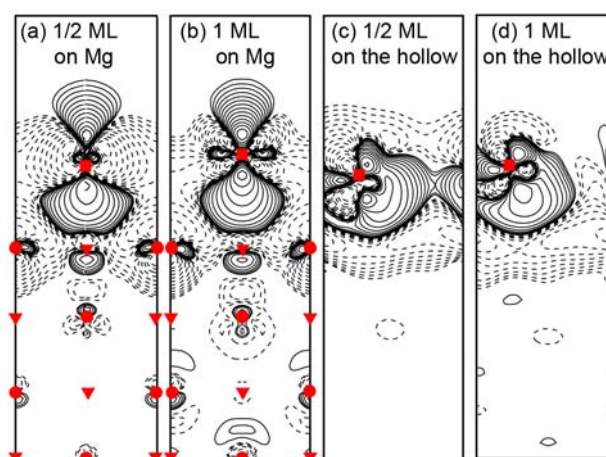


Figure 22 Electron density difference plots for the optimized interface system when Rh binds over Mg and the hollow site at difference coverages. Contour intervals are the same as in Figure 21.

For the hollow site, the electron contributions depend on the oxide environment region (Mg and O). As can be seen, from this hollow plane plotted, electrons accumulate around the Rh atoms and spread out to the area above the hollow oxide surface whereas the region at the hollow site and below the surface show the lack of electron density. Very small features are found in the layers below the topmost surface as a results of the lower coverage.

3.4 The electron localization function (ELF)

The electron localization function (ELF) is a useful tool to gain insight in to chemical bonding behavior of molecules and solid. In this study, the ELF plots were investigated as well. For a single wavefunction built from the Hartree-Fock or Kohn-Sham orbital φ_i , the ELF is defined by $ELF(r) = [1+(D_p/D_0)^2]^{-1}$ where D_p is the excess local kinetic energy due to Pauli repulsion and D_0 is the kinetic energy of a free-electron gas with density equal to $\rho(r)$. ELF has values between 0 and 1, where 1 corresponds to perfect localization. More details of ELF can be found elsewhere (Becke and Edgecombe, 1990; Silvi and Savin, 1994).

In Figure 23, the ELF plots for the 1/2 and 1 ML coverage are illustrated. As for the MgO substrate, very strong ionic interaction between Mg and O is clearly shown. The small changes of ionic characters are made at the surface due to the effect of Rh atoms. At 1 ML coverage, obviously, there is no feature of bonding characters between Rh and surface atoms of MgO can be seen, Rh binds neither to the O nor the Mg sites. This can be clearly explained by the resulting features of the charge density plots where the main contributions of the Rh-MgO bonding are the polarization of Rh electron induced by the MgO substrate (Giordano *et al.*, 2003).

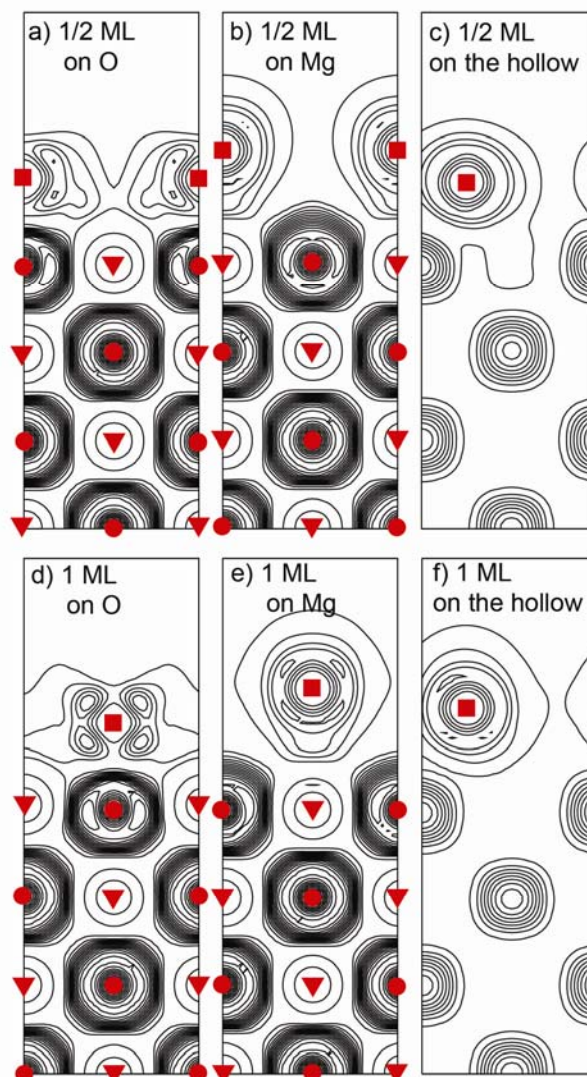


Figure 23 The ELF plots for the optimized interface system when the Rh binds over O, Mg and the hollow sites at the 1/2 and 1ML coverages. The ELF contours represent values between 0 to 1 (see text) and the increment for every contour line is 0.05 e/a.u.³.

3.5 Density of states (DOS)

To obtain a better understanding of the bonding character in solid materials, the density of states is a very useful tool to demonstrate such behavior. The DOS for 1/8, 1/2 and 1 ML coverages at different adsorption sites of Rh/MgO systems are presented in our study. The isolated systems of Rh and MgO are also discussed in details.

The total density of states (TDOS) of isolated Rh monolayer systems are shown in Figure 24 to clarify the DOS features compared to the reference isolated Rh atom and bulk Rh systems. The TDOS features obtained from spin polarized calculation show the non-magnetic properties for the Rh bulk system. It is clearly that the splitting of DOS plots are presented by the majority spin components which lie below the minority ones in all cases. The narrow band widths and sharp peaks are found when the coverage decreases from the Rh bulk to the isolated Rh atom, related to the less forming interactions of Rh atoms in the Rh layer. This can be explained from the trend of the $\Delta E_{\text{formation-of-Rh-layer}}$ that the smaller the $\Delta E_{\text{formation-of-Rh-layer}}$ the smaller the DOS peaks.

In order to study the electronic structure of the surface, layer-projected densities of states (LPDOS) of Rh/MgO were also investigated for each layer starting from the surface toward the slab center. At the most stable adsorption O site, the DOS of 1/8, 1/2 and 1 ML obtained from spin-polarized calculation are illustrated in Figure 25. The interactions of Rh and O atoms are due to the contributions of Rh $4d$ and O $2p$ states. These states are overlapped as can be seen in the TDOS plots (Figures 25). The stronger interaction is the result of more contributions of Rh $4d$ and O $2p$ states hybridization in the 1 ML coverage system. At the MgO surface layer, the LPDOS demonstrated the change of electronic properties induced by the strong interaction of the Rh monolayer to the surface oxygen. (compared to the LPDOS for a clean MgO surface in Figure 19c). Moreover, for small coverages, i.e. 1/8 and 1/2 ML, the different DOS behaviors for two types of O atoms can be observed (one of which is bound to Rh atom). Very much smaller changes of LPDOS features are shown in the

sub-surface layer and can not be seen in the center of the slab which confirmed that the layer slab model is thick enough to use for this interface system.

The TDOS and LPDOS for the Mg adsorption site are shown in Figure 26. The TDOS of Rh/MgO shows very similar features to those of the MgO clean surface. This can be explained by the weak interaction of Rh to surface Mg as stated under the interaction energy. Moreover, the LPDOS for each layer shows quite identical plots, referred to as a very weak interaction at the Mg site compared to the O site.

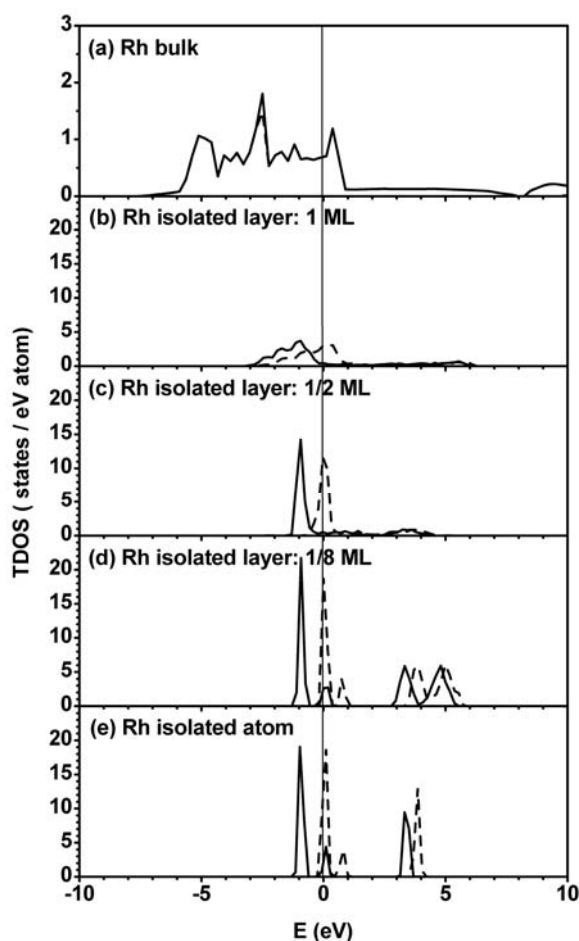


Figure 24 DOS for bulk Rh and different geometries (related to different coverages) of isolated Rh ML systems. The solid and dashed lines represent the majority and minority spin components, respectively.

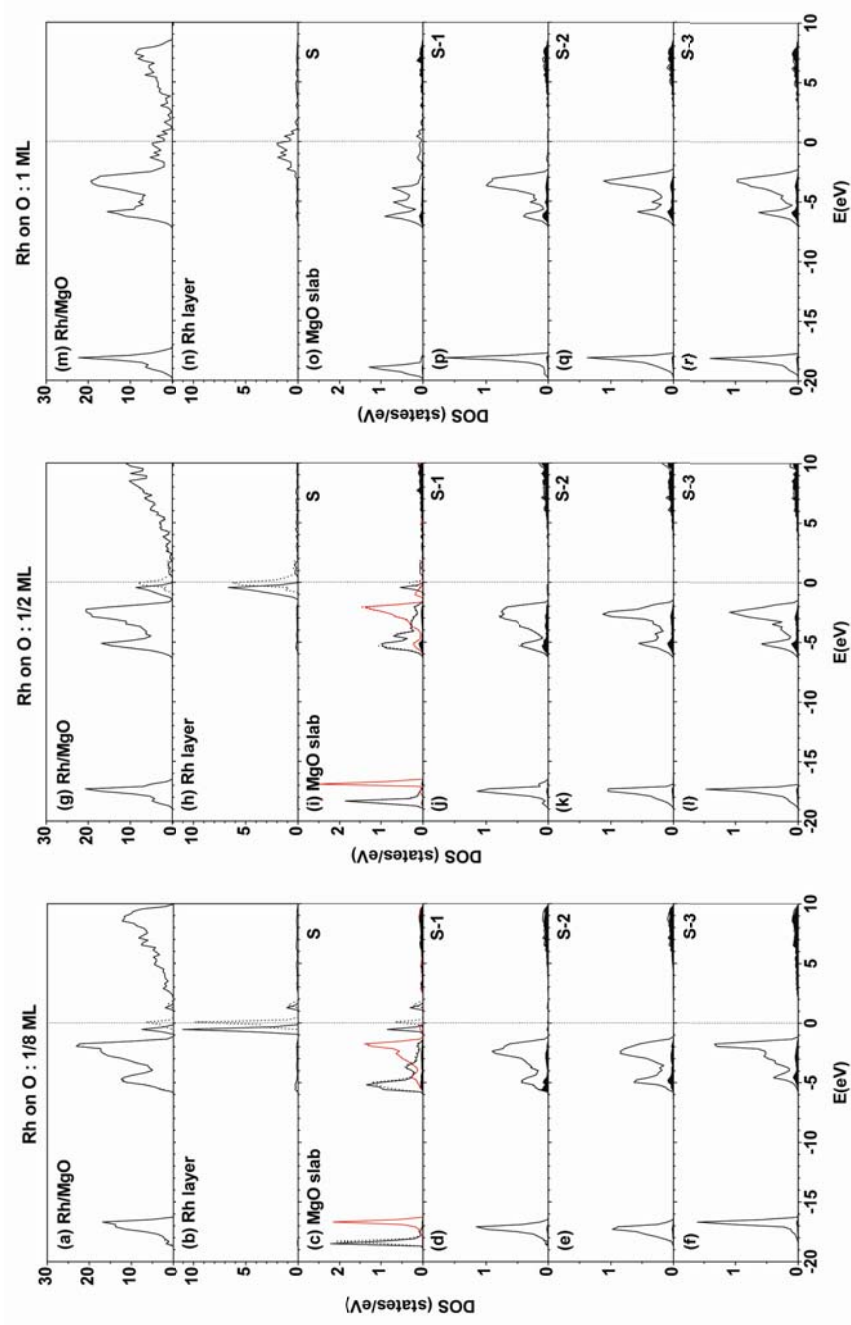


Figure 25 TDOS and LPDOS for Rh/MgO at the O adsorption site with difference coverages of Rh. Solid and dashed lines represent the majority and minority spin components, respectively. In (c) and (i), the light color line shows the $2p$ states of surface oxygen without Rh bound to it.

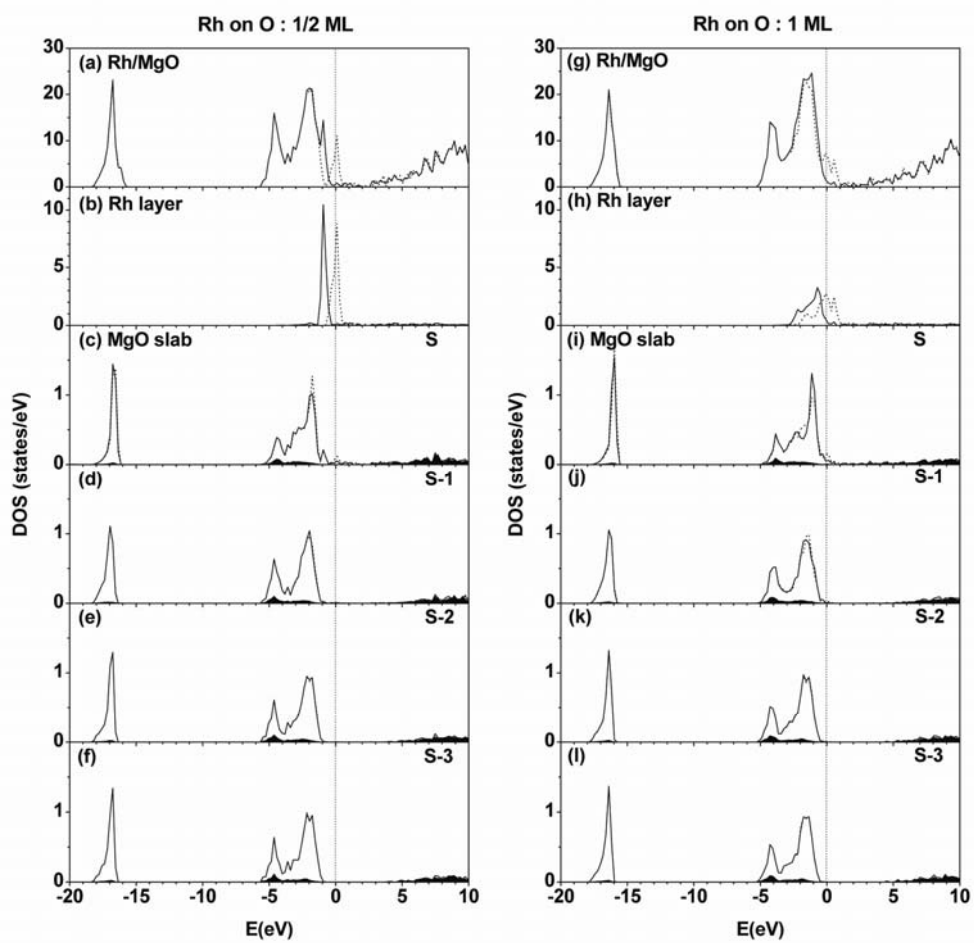


Figure 26 TDOS for Rh/MgO at the Mg adsorption site with difference coverages of Rh. Solid and dashed lines represent the majority and minority spin components, respectively.

3.5 The spin density and the magnetization

To determine the magnetic properties of solid materials, the spin-polarized calculations can provide these by giving the spin magnetic moment of each atom in the system studied. The magnetic moment of surface Mg, surface O and Rh atoms are reported here and we mention that all the values reported are the projected magnetic moments on the specific Wigner-Seitz sphere for Rh, Mg and O. It is found that the main effect of spin polarization is on the Rh atoms for all cases, while small effects are observed at the surface of MgO (see Table 9).

For the O site, the magnetic moment for Rh for 1/8, 1/2 and 1 ML are 0.88, 0.93 and 0.00 μ_B , respectively. The only case for which we do not get a magnetic moment is for 1 ML at the O site. This is confirmed by the plot in Figure 27, which shows the energy as a function of total magnetic moment. This result does not agree with the previously reported value, 1.21 μ_B (Wu and Freeman, 1995). To verify this controversy, the magnetic moment as a function of Rh-surface distance r is examined (see Figure 28). This is done by taking the relaxed atomic positions for both the MgO slab and the Rh layer, then the Rh is at the optimized distance r_o above the slab, and then rigidly moving the Rh layer relative to the MgO surface with no further relaxation. For all of the sites, and at all coverages, the Rh layers start out with magnetic moments the same as those of the isolated layers when $r \approx 5 \text{ \AA}$. In most cases, this rolls over for $r \approx 2\text{-}3 \text{ \AA}$, as the Rh layer starts to interact with the surface, before dropping to zero at some shorter distance. The details of the curves vary with the adsorption site, indicating the sensitivity of the Rh magnetism to details of the environment around the adsorbed atom. They also vary strongly with coverage, indicating the sensitivity to the weakening of the intra-layer d - d hybridization – in effect, sensitivity to the dimensionality. However, in almost all cases the optimal distance r_o happens to be before the moment falls to zero. The exception is for 1 ML at the O site, where $r_o = 2.10 \text{ \AA}$, with the moment having fallen to zero between 2.25 and 2.20 \AA . Wu and Freeman obtained an optimal distance of $r_o = 2.34 \text{ \AA}$. On our plot this would result in a moment of $\sim 1.4 \mu_B$ which is rather closer to the moment they

obtained. Indeed, we find a lower energy structure than theirs, with rather stronger interaction energy than they reported (0.94 eV vs 0.84 eV).

The magnetic moment plotted against estimates of the $d-d$ and $d-p$ interaction strengths detailed in Table 9 is plotted in Figure 29. The $d-d$ interaction strength is estimated by the formation energies of the isolated layers and the $d-p$ interaction strength by the adsorption energies. Moments are plotted for the isolated layers and for all three adsorption sites, at all coverages calculated, at the optimal distances for simplicity. The trend is that increasing either the $p-d$ or $d-d$ interaction strength leads to reduced magnetic moments and increasing the $d-d$ interactions drives the system from localized to itinerant magnetism. Hence, in the search for magnetic $4d$ and $5d$ thin films and monolayers one has to examine the systems in which the adlayer and the surface only interact weakly and preferably with a low but ordered coverage. In the case of Rh on the MgO (100) surface, it is certainly necessary to go to coverages below 1 ML.

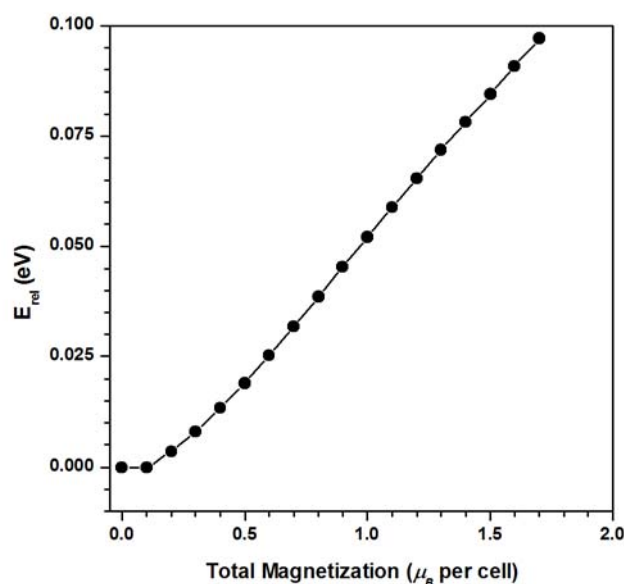


Figure 27 The relative energy as a function of the magnetization of Rh/MgO(001) at the O site for 1 ML coverage, a non magnetic state is defined by a zero energetic curve.

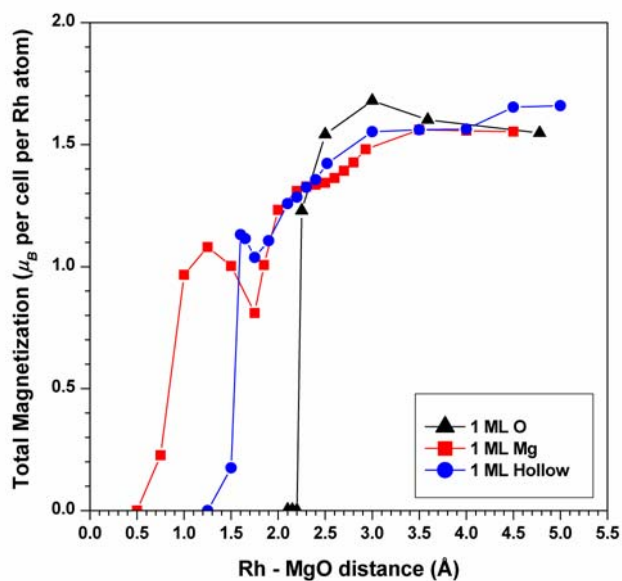


Figure 28 Total magnetization of the Rh/MgO system as a function of the interlayer distance of the Rh overlayer and surface for different adsorption sites of 1ML coverage.

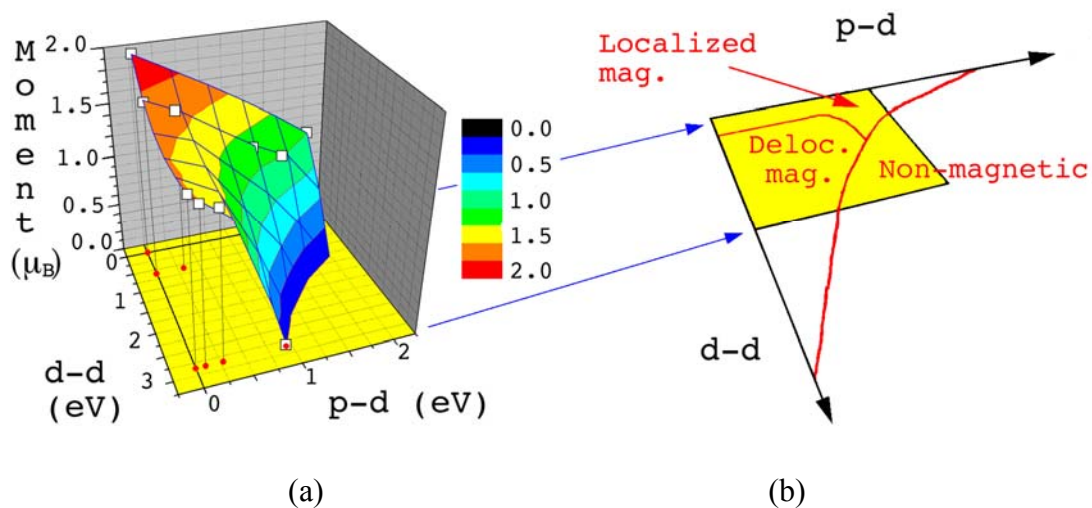


Figure 29 The illustration of localized and itinerant magnetism as well as non-magnetic regions as a function of the $d-d$ and $d-p$ interaction strength.

Table 9 Total and projected spin magnetic moments (in μ_B) for the Rh/MgO(001) system for different Rh coverages at the optimized Rh-surface distances. The values for the spin magnetic moments given here were calculated with spheres of the standard Wigner-Seitz spheres with radii of 1.402, 1.058 and 0.820 Å for Rh, Mg and O, respectively.

Coverage and adsorption site	Spin magnetic moment in Rh/MgO (μ_B)			Total magnetization for isolated Rh layer per atom
	Proj. on Rh (overlayer) per atom	Proj. on Mg (top layer) per atom	Proj. on O (top layer) per atom	
Rh atom	1.393			1.959
1/8 ML	1.398			1.966
on O (2.00 Å)	0.882	-0.001	0.049	0.999
1/2 ML	1.398			1.685
on O (2.10 Å)	0.933	-0.002	0.003	0.999
on Mg (2.77 Å)	1.310	-0.001	0.018	1.575
on Hollow (1.96 Å)	0.998	-0.003	0.034	1.134
1 ML	1.463			1.566
on O (2.10 Å)	0.000	0.000	0.000	0.008
on Mg (2.93 Å)	1.357	-0.001	0.027	1.480
on Hollow (2.52 Å)	1.286	-0.002	0.049	1.423

4. Conclusions

The interactions of the Rh/MgO(001) have been reported by means of DFT periodic calculations. Three adsorption sites as well as three coverages were investigated. From our calculations, Rh prefers to bind above O rather than the other sites supported by the strong interaction energies as well as the short Rh...O distances. At O site, the reverse buckling structure of Rh/MgO(001) was observed compared to the clean MgO(001) for 1 ML coverage. The stability of each system is determined in terms of the interaction energies, namely, adsorption energy, adhesion energy and formation energy. Our adhesion energies over O are in good agreement with those reported in the literature. The adsorption energy is found to increase with coverage whereas the adhesion energy decreases with coverage due to the increasing Rh formation of energy. The electronic properties, such as charge density difference contour plots, magnetic moment, DOS and ELF to clarify the bonding behaviors, are plotted. At the O site, more electrons are localized in the interstitial region between Rh and Mg, enhancing the stability of the system. Moreover, at the O site, more electron density rearrangement is introduced in the oxide slab than the adsorption at the Mg site. From spin polarized calculations, the Rh/MgO(001) systems are found to be magnetic in most cases, except for the 1ML coverage at the O site. The nonmagnetic observation here might occur due to the sensitivity of magnetism from the environment of the Rh/MgO structure as well as the interaction in the system. The ELF plots clearly show the bonding characters of the Rh/MgO system. The strong ionic interaction of MgO is shown and no bonding character between Rh to the surface can be observed.

Chapter IV. Interactions of Rhodium on (110) and (111) Surfaces of CeO₂

1. Bulk system

The calculated lattice constant for ceria bulk system is 5.47 Å, in agreement with the literature (see Table 10).

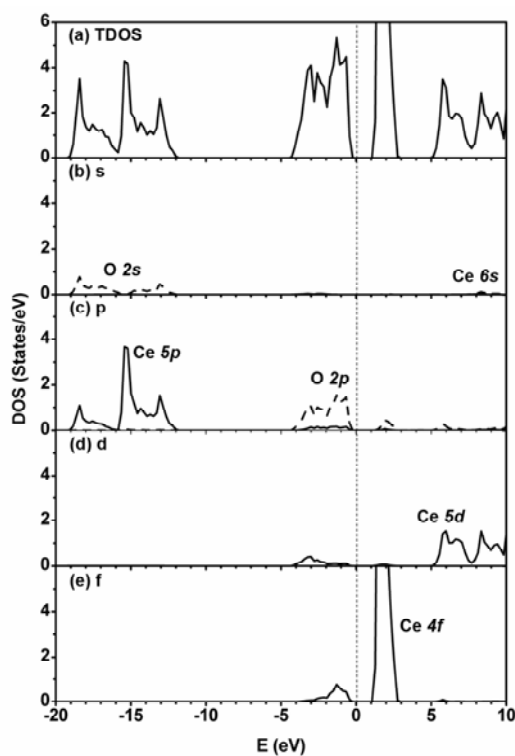


Figure 30 The total (TDOS) and partial (PDOS) densities of states of bulk CeO₂. In the PDOS panels, solid and dashed curves represent the PDOS of Ce and O, respectively. The Fermi energy is shown by the vertical dotted line.

Total (TDOS) and partial (PDOS) densities of states of bulk CeO₂ are depicted in Figure 30. It is clearly shown that CeO₂ is an insulator. The highest valence band is exhibited by O 2*p* states with some mixing states from Ce 4*f* and Ce 5*d*. The occupied states lie below further apart from the Fermi level are O 2*s* and Ce 5*p*. The states located above the Fermi level are Ce 4*f* states and two states situated above the empty Ce 4*f* states are Ce 6*s* and Ce 5*d*. The calculated energy gaps of O 2*p* - Ce 4*f* states and O 2*p* - Ce 5*d* states are 1.0 and 4.9 eV, respectively, these reported results reasonably agree with both the experimental values [3.0 and 6.0 (Wuilloud *et al.*, 1984)] and the theoretical calculations [i.e., 1.0 and 5.0 eV(Nolan *et al.*, 2005); 1.8 and 5.7 eV(Yang *et al.*, 2004b); 2.5 and 5.5 eV(Skorodumova *et al.*, 2002); 2.8 and 5.5 eV(Koelling *et al.*, 1983)].

Table 10 The calculated lattice constants and the surface energies for (110) and (111) ceria surfaces. All presented values are taken from the CeO₂(110)*p*(1×1) and CeO₂(111)*p*(1×1) models.

	Lattice constant (Å)	Surface energy (J/m ²)		
		(111)	(110)	(100)
This work	5.47	0.68	1.00	1.40
Z. Yang ^a	5.45	0.60	1.01	1.43
N.V. Skorodumova ^b	5.47	0.68	1.05	1.41
M. Nolan ^c	5.47	0.68	1.01	1.41

^aYang *et al.*, 2004b

^bSkorodumova *et al.*, 2004

^cNolan *et al.*, 2005

2 Clean surfaces

2.1 Surface energy

The calculated surface energies for (111), (110) and (100) ceria orientations are reported to be 0.68, 1.00 and 1.40 J/m², respectively, indicating that the (111) surface is the most stable surface followed by the (110) and (100), respectively. As a result, the surface stability is predicted in the order of (111) > (110) > (100). Our DFT-GGA results are in agreement with previous DFT studies (Yang *et al.*, 2004b; Skorodumova *et al.*, 2004; Nolan *et al.*, 2005) as shown in Table 10.

2.2 Structural relaxation

The structural relaxations for the clean surfaces of the low index surfaces of ceria for CeO₂(110) and CeO₂(111) are illustrated in Figures 31-32. The positive and negative values in each plot present the outward and inward displacements compared to the optimized bulk positions.

For the relaxation of the (110) surface (Figure 31a), it can be seen that both the O and Ce atoms at the topmost surface layer are moved inward to the slab center. There is no significant change for O atoms (0.04 Å) while the displacement of Ce atoms is remarkable (0.18 Å). The Ce-O distance in the surface layer is 2.33 Å, which is shorter than the observation in the optimized bulk system (2.37 Å). This is due to the lateral change of O atoms in the surface layer. As for the subsurface, the Ce atoms are shifted upward to the surface by about 0.1 Å and no notable change can be seen for the other surfaces close to the slab center. These results compare well with previous DFT studies (Nolan *et al.*, 2005). As for the (111) surface (Figure 32a), the most stable surface, the relaxations are rather small where a few topmost layers are moved slightly inward to the center of the slab model. The surface O atoms show more displacement than those of the Ce atoms. This is a reverse trend compared to the (110) surface. The Ce-O_s and Ce-O_{ss} bond distances are shown to be 2.39 and 2.35 Å, respectively. Furthermore, there is no lateral movement of such atoms in each layer.

The differences of slab layers as well as the differences of surface area of the models were also compared. It was found that the 5 atomic layers of the $\text{CeO}_2(110)p(1\times 2)$ and the 12 atomic layers of the $\text{CeO}_2(111)p(\sqrt{3}\times 1)$ can represent very well the 9 and 21 atomic layers of $\text{CeO}_2(110)p(1\times 1)$ and $\text{CeO}_2(111)p(1\times 1)$, respectively. The resemblance of the relaxation behaviors for such smaller layer thickness models can be seen in Figures 31b and 32b.

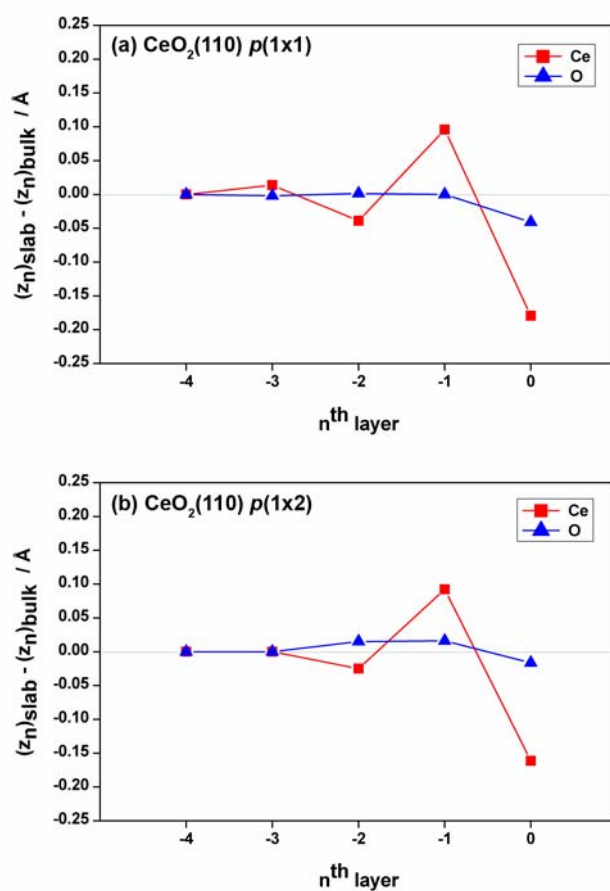


Figure 31 Inter-planar displacement of $\text{CeO}_2(110)$ of (a) $p(1\times 1)$ and (b) $p(1\times 2)$ supercells. The outward and inward displacements compared to bulk are represented by positive and negative values, respectively.

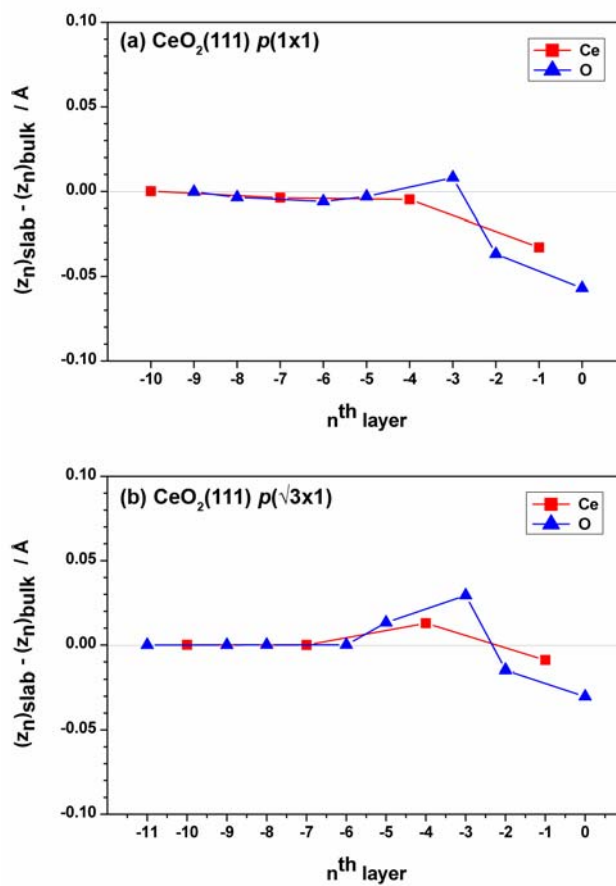


Figure 32 Inter-planar displacement of $\text{CeO}_2(111)$: (a) $p(1 \times 1)$ and (b) $p(\sqrt{3} \times 1)$ supercells. The outward and inward displacements compared to bulk are represented by positive and negative values, respectively.

3 Rh/CeO₂ interface systems

In this section, the structural, energetic and electronic properties of the Rh/CeO₂ interface systems, depending upon the adsorption site and the coverage number, are discussed. It is noted that all values reported in texts are taken from the calculations for Rh/CeO₂(110)*p*(1×2) and Rh/CeO₂(111)*p*($\sqrt{3}\times 1$) models.

3.1 Adsorption energy

3.1.1 Adsorption site dependence

The adsorption sites dependence was explored for the selected 1 ML coverage of Rh on (110) and (111) surfaces. The optimized Rh-surface distances and the interaction energies of the Rh/CeO₂(110) and Rh/CeO₂(111) systems are reported in Table 11.

For the (110) surface, the surface oxygen site is the most preferable adsorption site, indicated by the very strong interaction compared to that of the Ce site as shown by more adsorption energy and the shorter Rh-surface distance. The adsorption energies for the O_s and Ce sites are 4.07 and 1.30 eV, respectively. The adsorption energy of the O_s site is approximately three times more than that of the Ce site. For the O_s site, the formation energy of Rh atoms show more contribution than the adhesion energy to form the total process of adsorption system. This can be explained by the fact that the greater stabilization on O_s was mainly due to the Rh-Rh interactions in the Rh overlayer than the interactions between the Rh overlayer and CeO₂ substrate. On the other hand, the E_{form} and E_{adh} for the Ce site are shown in another trend, the adhesion energy is predicted to be rather higher than the formation energy. This is due to the lack of Rh-Rh interaction in the Rh overlayer as compared to that of at the O_s site. The structural topology of the O_s and Ce atoms on the (110) surface play very important roles in the interactions between the Rh overlayer and CeO₂(110) surface.

Table 11 The optimized Rh-surface distances and the interaction energies for Rh/CeO₂ systems.

Adsorption site	model	R (Å)	E_{form} (eV/Rh atom)	E_{adh} (eV/Rh atom)	E_{ads} (eV/Rh atom)
(110)					
O _s	$p(1\times 1)$	1.97	2.56	1.51	4.06
	$p(1\times 2)$	1.96	2.56	1.51	4.07
Ce	$p(1\times 1)$	2.37	0.54	0.77	1.31
	$p(1\times 2)$	2.37	0.54	0.77	1.30
(111)					
O _s	$p(1\times 1)$	1.92	1.26	1.94	3.20
	$p(\sqrt{3}\times 1)$	1.93	1.26	1.94	3.19
Ce	$p(1\times 1)$	2.32	1.26	1.78	3.04
	$p(\sqrt{3}\times 1)$	2.32	1.26	1.75	3.00
O _{ss}	$p(1\times 1)$	2.72	1.26	1.92	3.17
	$p(\sqrt{3}\times 1)$	2.72	1.26	1.92	3.17

For the (111) surface, the adsorption energies for O_s, Ce and O_{ss} sites are 3.19, 3.00 and 3.17 eV, respectively. These results agree well with the scarce literatures available for Pt/CeO₂(111) and Pd/CeO₂(111) systems (Alfredsson and Catlow, 2002). The E_{form} of the Rh overlayer for each adsorption site is identical, since the neighbor atoms for each adsorption site are located in the same pattern. The difference of the interactions among these sites was found to be rather small, even the difference of Rh-surface distances for each system are notably large (1.93, 2.32 and 2.72 Å for the O_s, Ce and O_{ss} sites, respectively). It is shown that the high mobility of Rh atoms on the surface might be expected. The corresponding structure relaxations for the Rh/CeO₂(110) and Rh/CeO₂(111) systems are illustrated in Figures 33-34 to explore the structural behavior for each system.

From Figure 33, the different structural relaxation for the O_s and Ce sites can be observed. For the O_s adsorption site, the O and Ce atoms at the topmost surface are moved slightly upward from the optimized positions in the clean surface by about 0.08 Å because of the interaction of Rh atoms. As for the Ce adsorption site, the structural relaxations are rather small (almost unchanged), this can be explained by the weaker interactions between the Rh overlayer and ceria substrate as reported in Table 11.

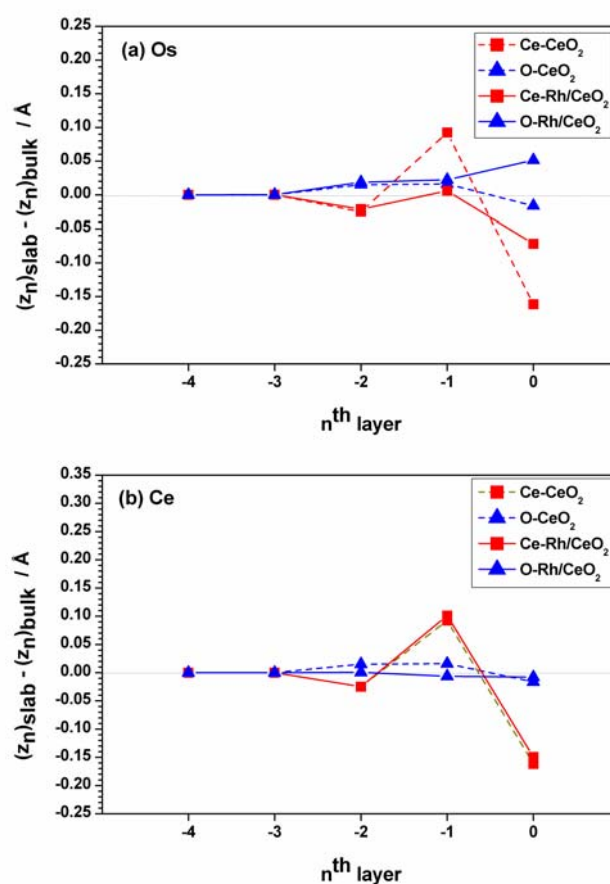


Figure 33 Inter-planar displacement for Rh/CeO₂(110)*p*(1×2) system. (a) O_s and (b) Ce adsorption sites. The outward and inward displacements compared to bulk are represented by positive and negative values, respectively.

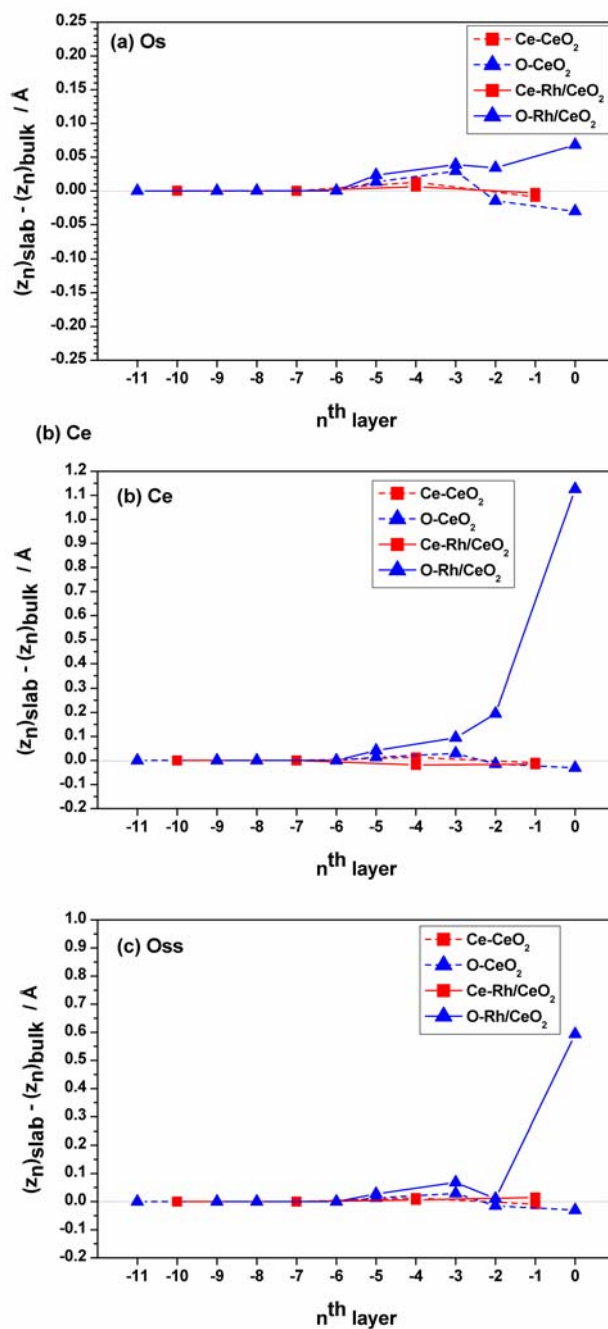


Figure 34 Inter-planar displacement for Rh/CeO₂(111)*p*($\sqrt{3} \times 1$) system. (a) O_s, (b) Ce and (c) O_{ss} adsorption sites. The outward and inward displacements compared to bulk are represented by positive and negative values, respectively.

For the (111) surface, the small change of structural relaxation of surface oxygen is illustrated for the O_s adsorption site system (0.1 Å). For the Ce and O_{ss} adsorption sites, on the other hand, the remarkable change of the surface relaxation can be observed. The surface oxygen atoms are moved significantly upward from the clean surface by about 1.1 and 0.6 Å for the Ce and O_{ss} sites, respectively. As a result, the adsorption energies among three adsorption sites are very similar due to the fact that the Rh overlayer is stabilized by the extra binding interactions from the displaced surface oxygen atoms (O_s) as illustrated in Figure 35. From such behaviors, one might expect that this is due to the use of the small layer thickness of slab models, however, it is noted that the same behaviors are also found for the larger slab thickness, Rh/CeO₂(111)*p*(1×1) system. Thus, it can be concluded that the number of layer of the slab thickness does not play a significant role in such observed behaviors; it depends only upon the interactions of Rh. A more comprehensive discussion related to surface reconstruction is given here. For the Ce site, from Figure 35b, the Rh atom is bound to a Ce atom and three O_s atoms with the corresponding distances of 2.32 and 2.26 Å, respectively. The O_s atoms are moved upward relatively to the optimized clean surface positions by the elongation of Ce-O distance from 2.35 Å to 2.95 Å. As for the O_{ss} site, the O_s atoms are displaced upward from the surface with the increment of the Ce- O_s distance from 2.35 Å to 2.62 Å. Thus, the Rh overlayer is stabilized via the strong interactions of Rh with the three nearest O_s atoms in cooperation with the weaker interactions with the O_{ss} atom and the three nearest Ce atoms where the corresponding distances were found to be 2.31, 2.72 and 2.95 Å, respectively. As a result, it was found that more adsorption energy for the O_{ss} site than that of the Ce site owing to the more cooperative effects with neighboring atoms. Moreover, it might be concluded here that Rh atoms could be immersed into the ceria surface due to the deformations of topmost surface oxygen atoms. This suggests a metal growth difficulty in the forming layer-by-layer of the Rh overlayer on CeO₂(111).

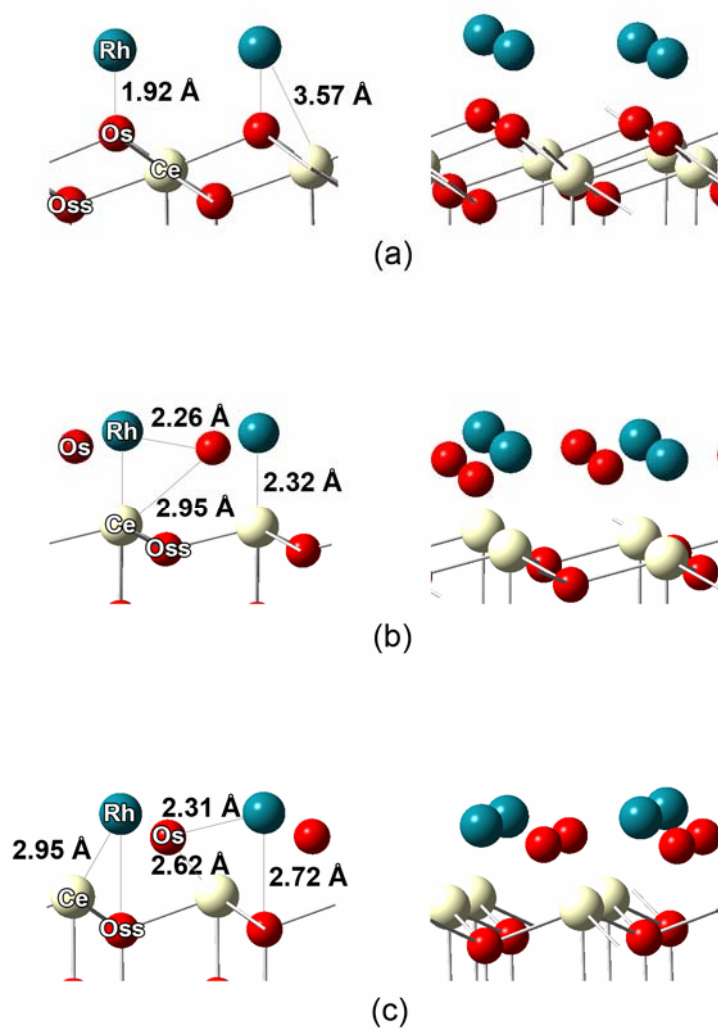


Figure 35 The structural relaxation for Rh/CeO₂(111)*p*($\sqrt{3} \times 1$) system. (a) O_s, (b) Ce and (c) O_{ss} adsorption sites.

3.1.2 Coverage dependence

The coverage dependence calculations for the (110) and (111) surfaces of ceria are summarized in Table 12. All the results are simulated only for the O_s adsorption site. As the coverage is increased, from 1/2 to 1 ML, the adsorption energies for both surfaces are increased owing to the more metal-metal interactions within the Rh overlayer, giving more contributions to the stabilization of the Rh/CeO₂ interface. On the other hand, the adhesion energies are decreased, which indicate that the Rh-oxide interaction dominates at low coverage. It has been well known that the growth modes of metal on substrate are relevant with adsorption and diffusion processes in the system. From the coverage dependence as well as adsorption site results, the growth modes of Rh/CeO₂ interface systems could be discussed.

Table 12 The optimized Rh-surface distances and the interaction energies for Rh/CeO₂ systems as the function of coverages. All calculations performed here are simulated for the O_s adsorption site.

Model	Coverage	R (Å)	E_{form} (eV/Rh atom)	E_{adh} (eV/Rh atom)	E_{ads} (eV/Rh atom)
(110)	1/2 ML	1.92	0.30	2.27	2.57
	1 ML	1.96	2.56	1.51	4.07
(111)	1/2 ML	1.90	0.50	2.16	2.66
	1 ML	1.93	1.26	1.94	3.19

3.2 Growth modes

Basically, the growth modes of metal on surfaces have been classified in three types: (i) *the Layer-by-Layer or Frank – van der Merwe* mode which involves a deposition of one monolayer at a time and results in a very smooth epitaxial film. This growth mode occurs when the cohesive energy between the film and the surface atoms is greater than the cohesive energy of the film atoms. It is indicated by the fact that the $E_{\text{form}} < E_{\text{adh}}$ in this case. The cohesive energy will decrease monotonically as each film layer is added. In the opposite case, where the deposit atoms are more strongly bound to each other than they are to the substrate ($E_{\text{form}} > E_{\text{adh}}$), (ii) *the Island, or Volmer-Weber* mode occurs, an intermediate case, and (iii) *the Layer-plus-Island, or Stranski-Krastanov* growth mode, which is much more common than one might think, where the layers form first, then for some reason or other the system gets tired of this, and switches to islands.

The growth modes for Rh deposited on $\text{CeO}_2(110)$ and $\text{CeO}_2(111)$ for the O_s adsorption site as a function of coverages are predicted here. For the (110) case, at low coverage, (1/2 ML), the calculated E_{form} and E_{adh} are 0.30 and 2.27 eV, respectively, indicating that the Frank – van der Merwe mode is expected to form. When the coverage increases, on the other hand, the Volmer-Weber mode is predicted, as can see from the calculated E_{form} and E_{adh} for the 1 ML (2.56 and 1.51 eV, respectively). For the (111) surface, only the Frank – van der Merwe is predicted to occur for both the 1/2 ML and 1 ML coverage. The increment of Rh coverage seems to reduce the possibility in forming the van der Merwe mode and the Stranski-Krastanov growth mode might exist. However, the interpretation of metal growth data is quite complicated since it is controlled by thermodynamic and kinetic factors. In this work, only the thermodynamic part in terms of E_{form} and E_{adh} was included. Therefore, the additional term of kinetic control must be considered to determine the growth modes of metal/metal oxide systems. The metal wetting on the surface might help to get more insight into the investigation of growth modes of such systems. For that reason, this theoretical technique might be reported later on.

3.3 Electron density difference

From Figure 36, the electron density difference, $\Delta\rho(\mathbf{r}) = \rho_{\text{Rh/Ceria}}(\mathbf{r}) - [\rho_{\text{Rh-layer}}(\mathbf{r}) + \rho_{\text{Ceria-slab}}(\mathbf{r})]$, is investigated for the Rh/CeO₂(111) systems. For the 1 ML coverage, $\Delta\rho$ plots for the O_s, Ce and O_{ss} sites are shown the different electron redistributions at Rh overlayers as well as the surface layers. For the O site (Figure 36b), electrons are depleted from the interstitial region between Rh and O_s, they are accumulated in the space over the Ce and O_{ss} sites. Moreover, more electron redistribution in the Rh overlayer can be observed due to the strong Rh-Rh interactions. These results compared well with previous theoretical work for the Rh/MgO(001) system (Nokbin *et al.*, 2004). On the other hand, the $\Delta\rho$ plots for the Ce and O_{ss} sites are shown somewhat differently than that of the O_s site. It is evident that electrons are lost in the space region between each Rh atom in the layer because of the much more electron localization in the region between Rh and the neighboring atoms on the ceria surface (dislocated O_s, Ce and O_{ss}) (see Figures 36c-36d). This can enhance the stabilization of the Rh atom. It is noted that the features observed for the Ce and O_{ss} sites are dependent upon the structural displacement of O_s at the surface. Since the interaction energies for all cases are very similar as previously mentioned, in the order of the O_s > O_{ss} > Ce site, thus, the electron redistributions for the slabs underneath the surface are quite similar as well.

As for the 1/2 ML coverage (Figure 36a), very similar features of $\Delta\rho$ plots compared to the 1 ML case (Figure 36b) can be observed. Owing to the lack of Rh-Rh interaction, electrons are more localized close to the Rh atom instead of the Rh-Rh interstitial region. The smaller features of $\Delta\rho$ can be observed in the slab layers below the surface compared to that of the 1 ML, in this case due to the smaller interaction.

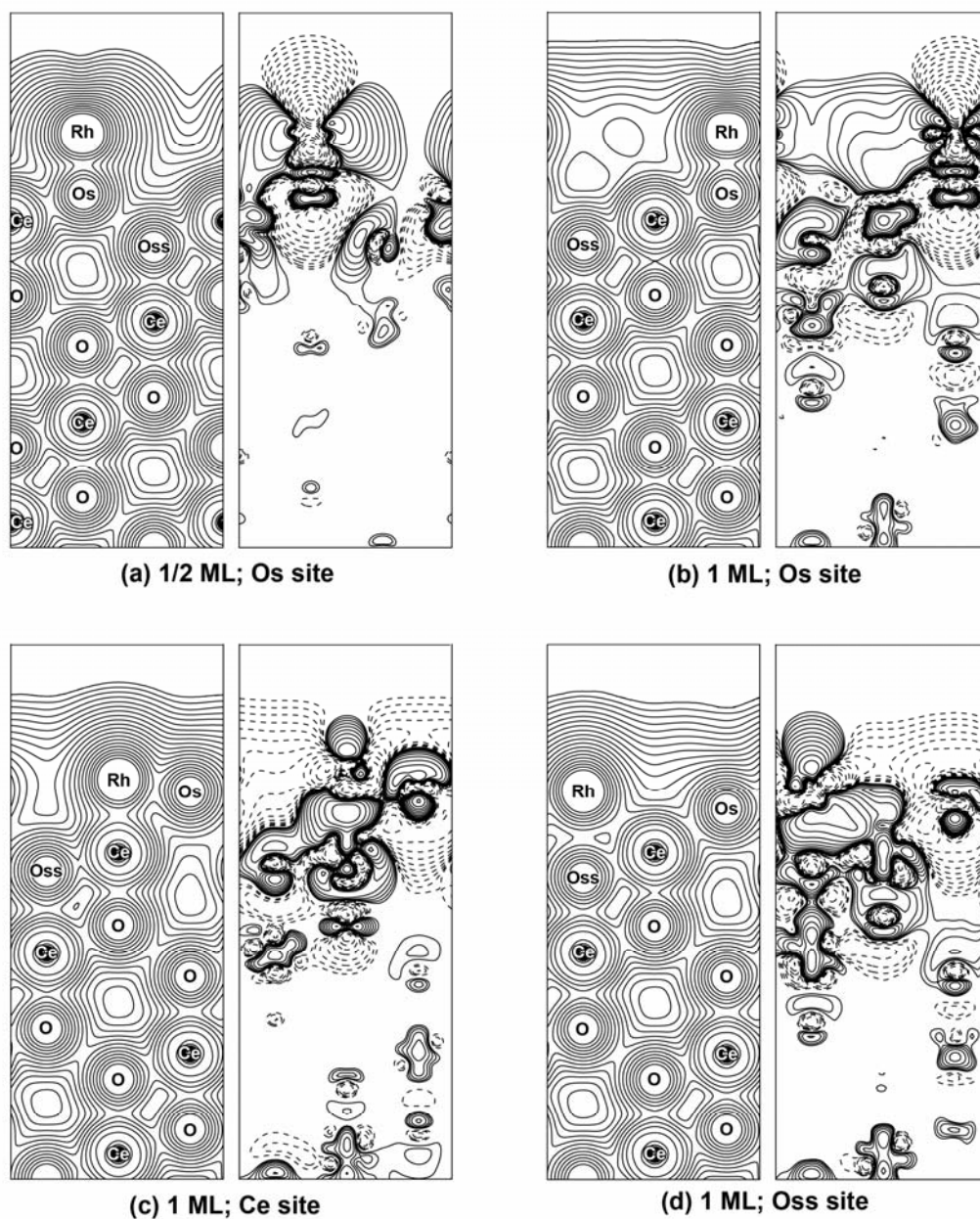


Figure 36 Electron density difference plots for the optimized interface system for Rh/CeO₂(111) at different coverages and adsorption sites: (a) 1/2 ML O_s, (b) 1 ML O_s, (c) 1 ML Ce and (d) 1 ML O_{ss}. Solid and dashed contour lines represent electron excess and electron loss, respectively. The contour lines start at ± 0.0005 e/a.u.³, increasing by a factor of $10^{0.2}$ for every contour line. In each figure, the total charge density is also plotted and shown in the left panel.

3.4 The electron localization function (ELF)

In order to understand the bonding in the interested system, the electron localization function plots can classify the main difference between ionic and covalent bonding characters. The ionic character is clearly shown in the case of the Rh/MgO(001) system, as previously mentioned, by the electrons of Mg and O atoms being localized around their atomic centers and no share electron contours between any pair of atoms (Mg and O) can be seen (see Figure 23). From Figure 37, for the CeO₂ substrate, the almost triangular shapes of the ELF contours are for O atoms while the round contours represent Ce atoms. It is clear that there is no shared electron between any Ce-O pair. Thus, the bonding characters in CeO₂ can be identified as polarized ionic which are in agreement with the literature (Skorodomova *et al.*, 2001).

For the Rh/CeO₂ system, the change of ELF plots at the surface compared to the center of the slab is rather small. At the O_s site, the Rh-O bonding is presented by the polarized ionic behavior. As for the Ce and O_{ss} sites, the bonding features also show less ionicity than that of the O_s adsorption site. As a result, the more covalent characters come from the interactions of Rh and the nearest neighboring atoms on the surface (Rh-Ce and Rh-O_s for the Ce site; Rh-O_{ss}, Rh-Ce and Rh-O_s for the O_{ss} site) which cause more electron redistributions induced by the Rh overlayer and the O_s atoms as shown in the electron density difference plots in Figure 36.

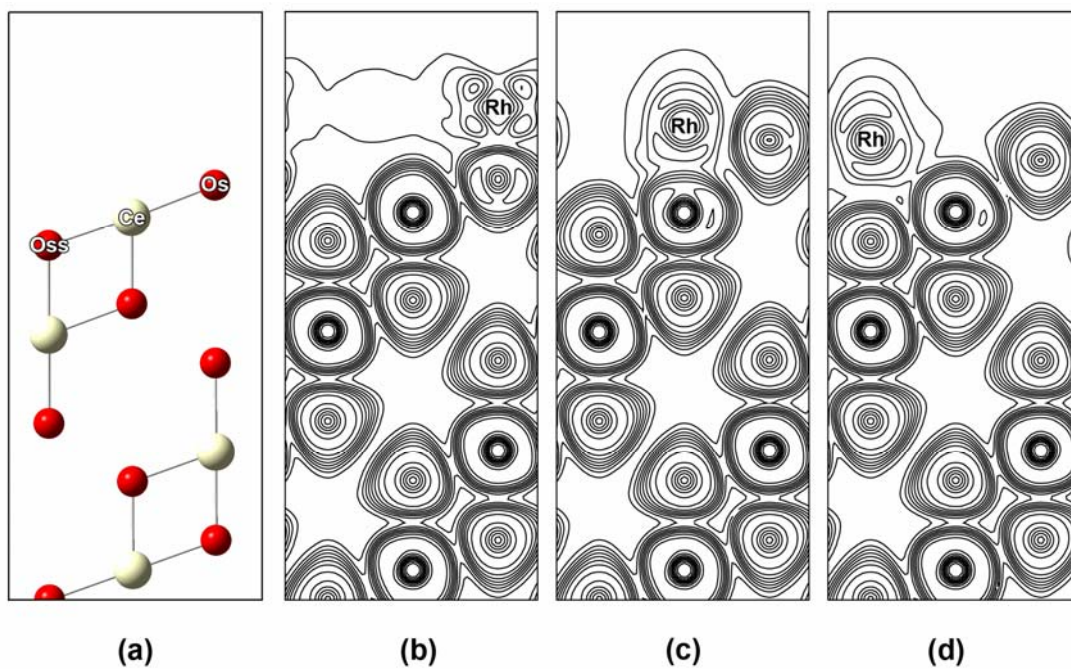


Figure 37 The electron localization function (ELF) plots for the optimized interface system for 1 ML coverage of Rh/CeO₂(111) at different adsorption sites: (a) atomic species in the selected cutting plane for the (b) O_s , (c) Ce and (d) O_{ss} adsorption sites. The ELF contours represent values between 0 to 1 (see text, page 69, for ELF definition) and the increment for every contour line is 0.1 e/a.u.³.

3.5 CO/Rh/CeO₂(111) and NO/Rh/CeO₂(111): preliminary results

In order to understand the catalytic functionality of the Rh/CeO₂ system, it is beneficial to study the adsorption of small adsorbed molecules with such combined interface. Here, the CO/Rh/CeO₂ and NO/Rh/CeO₂ systems were studied to explore the fundamental knowledge of these systems. It is noted that all results shown here are taken from the 1/2 ML Rh/CeO₂(111) model at the O_s site. Two types of adsorption models for each system were explored, depending on the directions of the adsorbed molecule. For CO adsorptions, the C-bound and O-bound models are reported when either the C or O atom bind to the surface. The NO adsorptions, N-bound and O-bound models are investigated as well by the N being directly bound to the surface for the former case and O is bound to the surface for the latter case. The optimized geometries of such systems are reported in Table 13 and Figure 38. In addition, the isolated CO and NO molecules were also calculated and used as reference systems which the corresponding optimized bond distances were found to be 1.14 and 1.17 Å, respectively, in agreement with the experimental observation (CO = 1.13 Å: Chackerian, 1976; NO = 1.15 Å: Perdew *et al.*, 1996).

In all cases, NO molecule binds to the Rh/CeO₂ interface more strongly than that of CO. Moreover, the interactions of such systems when either C or N atoms bound to the surface (C-bound and N-bound systems) are more stable than these of their counterpart structures (O-bound systems) [CO: -3.98 and -1.95 eV and NO: -5.72 and -3.81 eV]. In the case of CO, the stronger interaction of C-bound is represented by the shorter Rh-C and the longer O_s-Rh distances as compared to the Rh-O and O_s-Rh in the O-bound system. For NO case, the same features reported for the CO case can be observed. Due to the scarce studies of CO/Rh/CeO₂ and NO/Rh/CeO₂ systems in literature, all the results reported here can be compared to very similar systems such as CO/Rh/MgO(001) (Giordano *et al.*, 2003; Judai *et al.*, 2003) and NO/Rh/MgO(001) (Stirling *et al.*, 1997). The NO is also reported to be more stable than CO in the Rh/MgO(001) systems. When comparing the interactions of CO and NO adsorptions on the Rh/CeO₂ and Rh/MgO(001) surfaces, the interactions of CO and NO for Rh/CeO₂ interface systems are predicted to be more stable than those of

Rh/MgO(001) systems. Since the Rh-C and Rh-N distances in such systems are almost the same, the stronger interactions observed for CO/Rh/CeO₂ and NO/Rh/CeO₂ can be considered as the shorter O_s-Rh distance in the Rh/CeO₂ interface system resulting in stronger interactions of Rh and O_s atoms. In view of the fact that this section is reported just for the preliminary results, there are further more discussions related to experimental and theoretical studies that should be addressed, a more intensive discussion will be published in the future.

Table 13 The selected structural parameters and the corresponding adsorption energies for the CO/Rh/CeO₂(111) and NO/Rh/CeO₂(111) systems at O_s for the 1/2 ML Rh coverage.

X/Rh/CeO ₂ (111) X = CO or NO	Structural parameters (Å)				Adsorption Energy (eV)
	O _s -Rh	Rh-C	Rh-O	C-O	
CO				1.14	
C-bound	2.01	1.85	-	1.16	-3.98
	2.16 ^a	1.85 ^a	-	1.15 ^a	2.74 ^a
O-bound	1.93	-	2.01	1.16	-1.95
	O _s -Rh	Rh-N	Rh-O	N-O	
NO				1.17	
N-bound	1.92	1.74	-	1.17	-5.72
	2.00 ^b	1.73 ^b	-	1.16 ^b	-3.76 ^b
O-bound	1.90	-	1.82	1.18	-3.81

^aCO/Rh/MgO(001) system (Giordano *et al.*, 2003; Judai *et al.*, 2003).

^bNO/Rh/MgO(001) system (Stirling *et al.*, 1997).

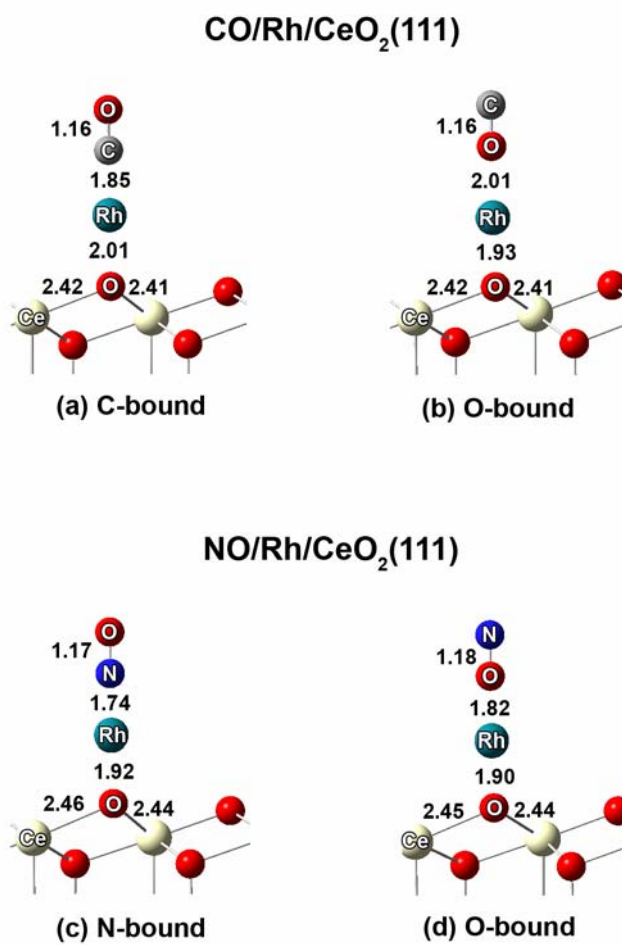


Figure 38 The optimized structural geometries for (a) C-bound, (b) O-bound models of CO/Rh/CeO₂(111), (c) N-bound and (d) O-bound models of NO/Rh/CeO₂(111) systems. All values are given in Å.

4. Conclusions

The interactions of Rh/CeO₂(110) and Rh/CeO₂(111) systems have been studied by means of periodic plane-wave density functional calculations using the VASP code and PAW method. The adsorption site dependence as well as the coverage dependence of such surfaces has been studied. Three types of interaction energies have been calculated to help characterize the metal-oxide interaction: the energy of adsorption of Rh atoms (E_{ads}), the energy of adhesion of a Rh overlayer (E_{adh}) and the formation-of-the-Rh-layer energy (E_{form}). As for the adsorption site dependence, the 1 ML coverage of the Rh overlayer was selected to study for all cases. Two adsorption sites, the surface oxygen (O_s) and the surface cerium (Ce) sites, were explored for (110) orientation and three adsorption sites for (111) surfaces, i.e., the surface oxygen (O_s), the subsurface cerium (Ce) and the subsurface oxygen (O_{ss}), were investigated as well. As a result, we found that the adsorption site preferences are in the order O_s > Ce and O_s > O_{ss} > Ce for (110) and (111) orientations, respectively. In case of coverage dependence, the 1/2 and 1 ML coverages of Rh were studied at O_s adsorption site for both (110) and (111) surfaces. It was found that, at the high coverage, the metal-metal interactions within the Rh overlayer give the largest contribution to the stabilization of the Rh/CeO₂ interface, giving rise of adsorption energy with the increasing surface coverage, while, naturally, the Rh-oxide interaction dominates at low coverage. The electron density difference plots are presented in this study. Moreover, the preliminary results for CO and NO adsorption on Rh/CeO₂(111) interface system are in comparative agreement with the scarce studies in the literature.

CONCLUDING REMARKS

The interactions of adsorbing molecules, H₂O and CH₃OH, on zeolites have been investigated by means of both the density functional theory quantum cluster and the embedded cluster methods. The embedded clusters are treated for the environmental effect of zeolites by using a set of point charges derived by the SCREEP method. The zeolite framework plays significant role in distinguishing the type of zeolites and also in enhancing the proton transfer from zeolite to adsorbed molecules. For the water cluster system, the ion-pair complex ZO(H₃O⁺)(H₂O)₃ can be observed when at least four water molecules exist in the finite cluster model. When the zeolite framework is taken into account, the protonated form is found when at least three water molecules appear in the system. The zeolite framework effect has also been observed in methanol cluster system, the methoxonium ion is found for the single methanol atom per acid site in Faujasite. However, these studies were carried out in the year 2002, to improve these works, the bigger zeolite framework and the use of a better method must be considered since nowadays the computational ability to do this is very efficient.

As for the surface systems, MgO(001) and CeO₂, it was found that Rh prefers to bind above the O site rather than the other sites for both types of metal oxide substrates as evidenced by the strong interaction energies as well as the short Rh...O distances. The stability of each system is determined in terms of the interaction energies, namely, adsorption energy, adhesion energy and formation energy. The adsorption energy is found to increase with coverage, whereas the adhesion energy decreases with coverage due to the increasing of Rh formation of energy. As a result, at the high coverage, the metal-metal interactions within the Rh overlayer give the largest contribution to the stabilization of the Rh/metal-oxide interface, giving rise to adsorption energy with the increasing surface coverage, while, naturally, the Rh-oxide interaction dominates at low coverage. Moreover, the electronic properties such as the density of states (DOS), the electron density difference plot, spin density plots and the electron localization function (ELF) are presented to clarify the chemical bonding behavior of the Rh/metal-oxide interface system.

LITERATURE CITED

- Alfredsson, M. and C. R. A. Catlow. 2002. A comparison between metal supported γ -ZrO₂ and CeO₂. **Phys. Chem. Chem. Phys.** 4(24): 6100-6108.
- Anderson, M. W. and J. Klinowski. 1990. Solid-state NMR evidence for the strong binding of methanol prior to carbon-carbon bond formation during the synthesis of gasoline on molecular sieve catalysts. **J. Chem. Soc., Chem. Commun.** (13): 918-920.
- _____ and _____. 1990. Solid-state NMR studies of the shape-selective catalytic conversion of methanol into gasoline on zeolite ZSM-5. **J. Am. Chem. Soc.** 112(1): 10-16.
- _____, _____ and P. J. Barrie. 1991. Proton magic-angle-spinning NMR studies of the adsorption of alcohols on molecular sieve catalysts. **J. Phys. Chem.** 95(1): 235-239.
- Baltache, H., R. Khenata, M. Sahnoun, M. Driz, B. Abbar and B. Bouhafs. 2004. Full potential calculation of structural, electronic and elastic properties of alkaline earth oxides MgO, CaO and SrO. **Physica B** 344(1-4): 334-342.
- Baltanas, M. A., J. H. Onuferko, S. T. McMillan and J. R. Katzer. 1987. An examination of a rhodium/magnesia catalyst using x-ray photoelectron spectroscopy. **J. Phys. Chem.** 91(14): 3772-3774.
- Bandiera, J. and C. Naccache. 1991. Kinetics of methanol dehydration on dealuminated H-mordenite: model with acidic and basic active centers. **Appl. Catal.** 69(1): 139-148.
- Bates, S. and J. Dwyer. 1994. Ab initio study of methanol sorption and proton transfer on a zeolite acid site model. **THEOCHEM** 112(1): 57-65.

- Becke, A. D. 1993. Density-functional thermochemistry. III. The role of exact exchange. **J. Chem. Phys.** 98(7): 5648-5652.
- _____ and K. E. Edgecombe. 1990. A simple measure of electron localization in atomic and molecular systems. **J. Chem. Phys.** 92(9): 5397-5403.
- Belzunegui, J. P. and J. Sanz. 2003. Metal particles coverage evidenced by ^1H NMR spectroscopy in high surface Rh/CeO₂ catalysts. **J. Phys. Chem. B** 107(42): 11705-11708.
- Birkenheuer, U., J. C. Boettger and N. Roesch. 1994. Charge separation and covalent bonding in metal oxide surfaces: A local density functional study on the MgO(001) surface. **J. Chem. Phys.** 100(9): 6826-6366.
- Blaszkowski, S. R. and R. A. van Santen. 1995. Density functional theory calculations of the activation of methanol by a Brønsted zeolitic proton. **J. Phys. Chem.** 99(30): 11728-11738.
- _____ and _____. 1997. Theoretical study of the mechanism of surface methoxy and dimethyl ether formation from methanol catalyzed by zeolitic protons. **J. Phys. Chem. B** 101(13): 2292-2305.
- Blöchl, P. E. 1994. Projector augmented-wave method. **Phys. Rev. B** 50(24): 17953-17979.
- Bogicevic, A. and D. R. Jennison. 2002. Effect of oxide vacancies on metal island nucleation. **Surf. Sci.** 515(2,3): L481-L486.
- Bortz, M. L., R. H. French, D. J. Jones, R. V. Kasowski and F. S. Ohuchi. 1990. Temperature dependence of the electronic structure of oxides: magnesium oxide, magnesium aluminum oxide, and aluminum oxide (MgO, MgAl₂O₄, and Al₂O₃). **Phys. Scr.** 41(4): 537-541.

- Bosacek, V. 1993. Formation of surface-bonded methoxy groups in the sorption of methanol and methyl iodide on zeolites studied by carbon-13 MAS NMR spectroscopy. **J. Phys. Chem.** 97(41): 10732-10737.
- Boys, S. F. and F. B. Bernardi. 1970. The calculation of small molecular interaction by the differences of separate total energies: Some procedures with reduced errors. **Mol. Phys.** 19: 553-566.
- Bronnimann, C. E. and G. E. Maciel. 1986. Carbon-¹³NMR study of methanol in HY zeolite. **J. Am. Chem. Soc.** 108(23): 7154-7159.
- Causa, M., R. Dovesi, C. Pisani and C. Roetti. 1986. Ab initio Hartree-Fock study of the magnesium oxide(001) surface. **Surf. Sci.** 175(3): 551-560.
- Chackerian, C., Jr. 1976. Electric dipole moment function of the $X^1\Sigma^+$ state of carbon monoxide: Vibration-rotation matrix elements for transitions of gas laser and astrophysical interest. **J. Chem. Phys.** 65(10): 4228-4233.
- Cox, P. A. and A. A. Williams. 1986. Surface excitons on ionic crystals. **Surf. Sci.** 175(2): L782-L786.
- Delplancke, M. P., P. Delcambe, L. Binst, M. Jardinier-Offergeld and F. Bouillon. 1986. Structure and purity of epitaxial films of copper and rhodium deposited onto magnesia single-crystal substrates by glow discharge sputtering. **Thin Solid Films** 143(1): 43-51.
- Didier, F. and J. Jupille. 1994. Layer-by-layer growth mode of silver on magnesium oxide (100). **Surf. Sci.** 307-309(1-3): 587-590.
- Eichler, A., J. Hafner, J. Furthmüller and G. Kresse. 1996. Structural and electronic properties of rhodium surfaces: an ab initio approach. **Surf. Sci.** 346(1-3): 300-321.

- Emrich, R. J., A. N. Mansour, D. E. Sayers, S. T. McMillan and J. R. Katzer. 1985. An examination of a rhodium/magnesium oxide catalyst using x-ray absorption spectroscopy. **J. Phys. Chem.** 89(20): 4261-4264.
- Evarestov, R. A. and A. V. Bandura. 2004. HF and DFT calculations of MgO surface energy and electrostatic potential using two- and three-periodic models. **Int. J. Quantum Chem.** 100(4): 452-459.
- Forester, T. R. and R. F. Howe. 1987. In situ FTIR studies of methanol and dimethyl ether in ZSM-5. **J. Am. Chem. Soc.** 109(17): 5076-5082.
- Frisch, M. J., G. W. Trucks, H. B. Schlegel, G. E. Scuseria, M. A. Robb, J. R. Cheeseman, V. G. Zakrzewski, J. A. Montgomery, Jr., R. E. Stratmann, J. C. Burant, S. Dapprich, J. M. Millam, A. D. Daniels, K. N. Kudin, M. C. Strain, O. Farkas, J. Tomasi, V. Barone, M. Cossi, R. Cammi, B. Mennucci, C. Pomelli, C. Adamo, S. Clifford, J. Ochterski, G. A. Petersson, P. Y. Ayala, Q. Cui, K. Morokuma, D. K. Malick, A. D. Rabuck, K. Raghavachari, J. B. Foresman, J. Cioslowski, J. V. Ortiz, A. G. Baboul, B. B. Stefanov, G. Liu, A. Liashenko, P. Piskorz, I. Komaromi, R. Gomperts, R. L. Martin, D. J. Fox, T. Keith, M. A. Al-Laham, C. Y. Peng, A. Nanayakkara, C. Gonzalez, M. Challacombe, P. M. W. Gill, B. Johnson, W. Chen, M. W. Wong, J. L. Andres, C. Gonzalez, M. Head-Gordon, E. S. Replogle and J. A. Pople. 1998. **Gaussian 98**, Gaussian, Inc., Pittsburgh, PA.
- Gale, J. D. 1996. A density functional study of molecular adsorption in zeolites. **Top. Catal.** 3(1,2): 169-194.
- _____, C. R. A. Catlow and J. R. Carruthers. 1993. An ab initio study of methanol adsorption in zeolites. **Chem. Phys. Lett.** 216(1,2): 155-161.

- Gennard, S., F. Cora and C. R. A. Catlow. 1999. Comparison of the bulk and surface properties of ceria and zirconia by ab initio investigations. **J. Phys. Chem. B** 103(46): 10158-10170.
- Giordano, L., A. Del Vitto, G. Pacchioni and A. M. Ferrari. 2003. CO adsorption on Rh, Pd and Ag atoms deposited on the MgO surface: a comparative ab initio study. **Surf. Sci.** 540(1): 63-75.
- Goniakowski, J. and C. Noguera. 1995. Relaxation and rumpling mechanisms on oxide surfaces. **Surf. Sci.** 323(1,2): 129-141.
- Greatbanks, S. P., I. H. Hillier, N. A. Burton and P. Sherwood. 1996. Adsorption of water and methanol on zeolite Brønsted acid sites: an ab initio, embedded cluster study including electron correlation. **J. Chem. Phys.** 105(9): 3770-3776.
- Haase, F. and J. Sauer. 1995. Interaction of methanol with Brønsted acid sites of zeolite catalysts: an ab initio study. **J. Am. Chem. Soc.** 117(13): 3780-3789.
- _____, _____ and J. Hutter. 1997. Ab initio molecular dynamics simulation of methanol adsorbed in chabazite. **Chem. Phys. Lett.** 266(3,4): 397-402.
- Henrich, V. E., G. Dresselhaus and H. J. Zeiger. 1980. Energy-dependent electron-energy-loss spectroscopy: Application to the surface and bulk electronic structure of magnesium oxide. **Phys. Rev. B** 22(10): 4764-4775.
- Hill, S. E. and C. R. A. Catlow. 1993. A Hartree-Fock periodic study of bulk ceria. **J. Phys. Chem. Solids** 54(4): 411-419.
- Huang, Y. Y., C. Liu and G. P. Felcher. 1993. Magnetization of ultrathin bcc. iron films on magnesium oxide. **Phys. Rev. B** 47(1): 183-189.

- Ison, A. and R. J. Gorte. 1984. The adsorption of methanol and water on H-ZSM-5. **J. Catal.** 89(1): 150-158.
- Jentys, A., G. Warecka, M. Derewinski and J. A. Lercher. 1989. Adsorption of water on ZSM-5 zeolites. **J. Phys. Chem. B** 93(12): 4837-4843.
- Jobic, H., A. Tuel, M. Krossner and J. Sauer. 1996. Water in interaction with acid sites in H-ZSM-5 zeolite does not form hydroxonium ions. A comparison between neutron scattering results and ab initio calculations. **J. Phys. Chem.** 100(50): 19545-19550.
- Judai, K., S. Abbet, A. S. Woerz, U. Heiz, L. Giordano and G. Pacchioni. 2003. Interaction of Ag, Rh, and Pd atoms with MgO thin films studied by the CO probe molecule. **J. Phys. Chem. B** 107(35): 9377-9387.
- Jura, G. and C. W. Garland. 1952. The experimental determination of the surface tension of magnesium oxide. **J. Am. Chem. Soc.** 74(23): 6033-6034.
- Kirsch, J. E. and S. Harris. 2004. Electronic structure studies of adsorbate-induced surface reconstructions. Oxygen on Rh(1 0 0). **Surf. Sci.** 553(1-3): 82-94.
- Kogelbauer, A., A. A. Nikolopoulos, J. G. Goodwin and G. Marcelin. 1995. Reactant adsorption and its impact upon methyl tert-butyl ether (MTBE) synthesis on zeolites. **J. Catal.** 152(1): 122-129.
- Kondo, J. N., M. Iizuka, K. Domen and F. Wakabayashi. 1997. IR Study of H₂O Adsorbed on H-ZSM-5. **Langmuir** 13(4): 747-750.
- Kotrla, J., D. Nachtigallova, L. Kubelkova, L. Heeribout, C. Doremieux-Morin and J. Fraissard. 1998. Hydrogen bonding of methanol with bridged OH groups of zeolites: Ab initio calculation, ¹H NMR, and FTIR Studies. **J. Phys. Chem. B** 102(14): 2454-2463.

Kresse G., and D. Joubert. 1999. From ultrasoft pseudopotentials to the projector augmented-wave method. **Phys. Rev. B** 59(3): 1758-1775.

_____ and J. Furthmueller. 1996. Efficient iterative schemes for ab initio total-energy calculations using a plane-wave basis set. **Phys. Rev. B** 54(16): 11169-11186.

_____ and J. Hafner. 1993. Ab initio molecular dynamics of liquid metals. **Phys. Rev. B** 47(1): 558-561.

Krossner, M. and J. Sauer. 1996. Interaction of water with Brønsted acidic sites of zeolite catalysts. Ab initio study of 1:1 and 2:1 surface complexes. **J. Phys. Chem. B** 100(15): 6199-6211.

Kubelkova, L., J. Novakova and K. Nedomova. 1990. Reactivity of surface species on zeolites in methanol conversion. **J. Catal.** 124(2): 441-450.

Lee, B., J. N. Kondo, K. Domen and F. Wakabayashi. 1999. FT-IR Study of H₂¹⁶O and H₂¹⁸O adsorption on H-ferrierite. **J. Mol. Catal. A: Chem.** 137(1-3): 269-272.

Li, C. and A. J. Freeman. 1991. Giant monolayer magnetization of iron on magnesium oxide: a nearly ideal two-dimensional magnetic system. **Phys. Rev. B** 43(1): 780-787.

_____, R. Wu, A. J. Freeman and C. L. Fu. 1993. Energetics, bonding mechanism, and electronic structure of metal-ceramic interfaces: silver/magnesium oxide (001). **Phys. Rev. B** 48(11): 8317-8322.

Limtrakul, J. 1995. Adsorption of methanol in zeolite, gallosilicate and SAPO catalysts. **Chem. Phys.** 193(1,2): 79-87.

- _____, P. Khongpracha, S. Jungsuttiwong and T. N. Truong. 2000. Adsorption of carbon monoxide in H-ZSM-5 and Li-ZSM-5 zeolites. An embedded ab initio cluster study. **J. Mol. Catal. A: Chem.** 153(1,2): 155-163.
- _____, P. Treesukol, C. Ebner, R. Sansone and M. Probst. 1997. Structures and potential energy surface of Faujasitic zeolite/water. **Chem. Phys.** 215(1): 77-87.
- _____, S. Jungsuttiwong and P. Khongpracha. 2000. Adsorption of carbon monoxide on H-FAU and Li-FAU zeolites. An embedded cluster approach. **J. Mol. Struct.** 525(1-3): 153-162.
- _____, T. Nanok, S. Jungsuttiwong, P. Khongpracha and T. N. Truong. 2001. Adsorption of unsaturated hydrocarbons on zeolites: The effects of the zeolite framework on adsorption properties of ethylene. **Chem. Phys. Lett.** 349(1,2): 161-166.
- Marabelli, F. and P. Wachter. 1987. Covalent insulator cerium dioxide: optical reflectivity measurements. **Phys. Rev. B** 36(2): 1238-1243.
- Marchese, L., J. Chen, P. A. Wright and J. M. Thomas. 1993. Formation of hydronium at the Brønsted site in SAPO-34 catalysts. **J. Phys. Chem.** 97(31): 8109-8112.
- Meisel, S. L., J. P. McCullough, C. H. Lechthaler and P. B. Weisz. 1976. Gasoline from methanol in one step. **Chem. Tech.** 6(2): 86-89.
- Messow, U., K. Quitzsch and H. Herden. 1984. Heats of immersion of ZSM-5 zeolite in n-alkanes, 1-alkenes and 1-alcohols at 30° C. **Zeolites** 4(3): 255-258.

- Mihaleva, V. V., R. A. van Santen and A. P. J. Jansen. 2001. A DFT study of methanol adsorption in 8T rings of Chabazite. **J. Phys. Chem. B** 105(29): 6874-6879.
- Mirth, G., J. A. Lercher, M. W. Anderson and J. Klinowski. 1990. Adsorption complexes of methanol on zeolite ZSM-5. **J. Chem. Soc., Faraday Trans.** 86(17): 3039-3044.
- Monkhorst, H. J. and J. D. Pack. 1976. Special points for Brillouin-zone integrations **Phys. Rev. B** 13(12): 5188-5192.
- Mortier, W. J., E. Van den Bossche and J. B. Uytterhoeven. 1984. Influence of the temperature and water adsorption on the cation location in Na-Y zeolites. **Zeolites** 4(1): 41-44.
- Munson, E. J., A. A. Kheir, N. D. Lazo and J. F. Haw. 1992. In situ solid-state NMR study of methanol-to-gasoline chemistry in zeolite HZSM-5. **J. Phys. Chem.** 96(19): 7740-7746.
- _____, N. D. Lazo, M. E. Moellenhoff and J. F. Haw. 1991. Carbon monoxide is neither an intermediate nor a catalyst in MTG chemistry on zeolite HZSM-5. **J. Am. Chem. Soc.** 113(7): 2783-2784.
- Nakamatsu, H., A. Sudo and S. Kawai. 1988. Relaxation of the magnesia (100) surface studied by ICISS. **Surf. Sci.** 194(1,2): 265-274.
- Nokbin, S., J. Limtrakul and K. Hermansson. 2004. DFT plane-wave calculations of the Rh/MgO(001) interface. **Surf. Sci.** 566-568(Pt.2): 977-982.
- Nolan, M., S. Grigoleit, D. C. Sayle, S. C. Parker and G. W. Watson. 2005. Density functional theory studies of the structure and electronic structure of pure and defective low index surfaces of ceria. **Surf. Sci.** 576(1-3): 217-229.

- Nusterer, E., P. E. Bloechl and K. Schwarz. 1996. Structure and dynamics of methanol in a zeolite. **Angew. Chem. Int. Ed.** 35(2): 175-177.
- Pandey, R., J. E. Jaffe and A. B. Kunz. 1991. Ab initio band-structure calculations for alkaline earth oxides and sulfides. **Phys. Rev. B** 43(11): 9228-9237.
- Perdew, J. P., J. A. Chevary, S. H. Vosko, K. A. Jackson, M. R. Pederson, D. J. Singh and C. Fiolhais. 1992. Atoms, molecules, solids, and surfaces: applications of the generalized gradient approximation for exchange and correlation. **Phys. Rev. B** 46(11): 6671-6687.
- _____, K. Burke and M. Ernzerhof. 1996. Generalized gradient approximation made simple. **Phys. Rev. Lett.** 77(18): 3865-3868.
- Pelmenschikov, A. G. and R. A. van Santen. 1993. Water adsorption on zeolites: ab-initio interpretation of IR data. **J. Phys. Chem.** 97(41): 10678-10680.
- Rieder, K. H. 1982. Helium diffraction from MgO(100). **Surf. Sci.** 188(1,2): 57-65.
- Rice, M. J., A. K. Chakraborty and A. T. Bell. 1998. A density functional theory study of the interactions of H₂O with H-ZSM-5, Cu-ZSM-5, and Co-ZSM-5. **J. Phys. Chem. A** 102(38): 7498-7504.
- Sayle, T. X. T., S. C. Parker and C. R. A. Catlow. 1994. The role of oxygen vacancies on ceria surfaces in the oxidation of carbon monoxide. **Surf. Sci.** 316(3): 329-336.
- Schönberger, U. and F. Aryasetiawan. 1995. Bulk and surface electronic structure of MgO. **Phys. Rev. B** 52(12): 8788-8793.

- Schiffino, R. S. and R. P. Merrill. 1993. A mechanistic study of the methanol dehydration reaction on γ -alumina catalyst. **J. Phys. Chem.** 97(24): 6425-6435.
- Shah, R., J. D. Gale and M. C. Payne. 1996. Methanol adsorption in zeolites - A first-principles study. **J. Phys. Chem.** 100(28): 11688-11697.
- _____, _____ and _____. 1997. In Situ study of reactive intermediates of methanol in zeolites from first principles calculations. **J. Phys. Chem. B** 101(24): 4787-4797.
- _____, M. C. Payne, M. H. Lee and J. D. Gale. 1996. Understanding the catalytic behavior of zeolites: a first-principles study of the adsorption of methanol. **Science** 271(5254): 1395-1397.
- Silvi, B. and A. Savin. 1994. Classification of chemical bonds based on topological analysis of electron localization functions. **Nature** (London, United Kingdom) 371(6499): 683-686.
- Sinclair, P. E. and C. R. A. Catlow. 1996. Computational studies of the reaction of methanol at aluminosilicate Brønsted acid sites. **J. Chem. Soc., Faraday Trans.** 92(12): 2099-2105.
- Singh, H. P. 1968. Determination of thermal expansion of germanium, rhodium, and iridium by x-rays. **Acta Crystallogr., Sect. A: Found. Crystallogr.** 24(Pt.4): 469-471.
- Skorodumova, N. V., M. Baudin and K. Hermansson. 2004. Surface properties of CeO_2 from first principles. **Phys. Rev. B** 69(7): 075401/1-075401/8.

- _____, R. Ahuja, S. I. Simak, I. A. Abrikosov, B. Johansson and B. I. Lundqvist. 2001. Electronic, bonding, and optical properties of CeO₂ and Ce₂O₃ from first principles. **Phys. Rev. B** 64(11): 115108/1-115108/9.
- Smith, L., A. K. Cheetham, R. E. Morris, L. Marchese, J. Thomas, P. A. Wright and J. Chen. 1996. On the nature of water bound to a solid acid catalyst. **Science** 271(5250): 799-802.
- Stefanovich, E. V. and T. N. Truong. 1998. A simple method for incorporating Madelung field effects into ab initio embedded cluster calculations of crystals and macromolecules. **J. Phys. Chem. B** 102(16): 3018-3022.
- Stich, I., J. D. Gale, K. Terakura and M. C. Payne. 1998. Dynamical observation of the catalytic activation of methanol in zeolites. **Chem. Phys. Lett.** 283(5,6): 402-408.
- Stirling, A., I. Gunji, A. Endou, Y. Oumi, M. Kubo and A. Miyamoto. 1997. G-Point density functional calculations on the adsorption of rhodium and palladium particles on MgO(001) surface and their reactivity. **J. Chem. Soc., Faraday Trans.** 93(6): 1175-1178.
- Sulikowski, B. and J. Klinowski. 1992. trans-But-2-ene is the first hydrocarbon produced in the conversion of methanol to gasoline over zeolite H-ZSM-5. **Appl. Catal. A** 89(1): 69-75.
- Tasker, P. W. and D. M. Duffy. 1984. The structure and properties of the stepped surfaces of magnesium oxide and nickel monoxide. **Surf. Sci.** 137(1): 91-102.
- Termath, V., F. Haase, J. Sauer, J. Hutter and M. Parrinello. 1998. Understanding the nature of water bound to solid acid surfaces. Ab initio simulation on HSAPO-34. **J. Am. Chem. Soc.** 120(33): 8512-8516.

- Tosi, M. P. 1964. Cohesion of ionic solids in the Born model. **Solid State Phys.** 16: 1-120.
- Urano, T., T. Kanaji and M. Kaburagi. 1983. Surface structure of magnesium oxide(001) surface studied by LEED. **Surf. Sci.** 134(1): 109-121.
- Wakabayashi, F., J. N. Kondo, K. Domen and C. Hirose. 1996. FT-IR study of H₂¹⁸O adsorption on H-ZSM-5: direct evidence for the hydrogen-bonded adsorption of water. **J. Phys. Chem.** 100(5): 1442-1444.
- Watson, G. W., E. T. Kelsey, N. H. de Leeuw, D. J. Harris and S. C. Parker. 1996. Atomistic simulation of dislocations, surfaces and interfaces in MgO. **J. Chem. Soc., Faraday Trans.** 92(3): 433-438.
- Whited, R. C., C. J. Flaten and W. C. Walker. 1973. Exciton thermoreflectance of magnesium oxide and calcium oxide. **Solid State Commun.** 13(11): 1903-1905.
- Wu, R. and A. J. Freeman. 1995. Metal-ceramic interfaces: overlayer-induced reconstruction and magnetism of 4d transition-metal monolayers. **Phys. Rev. B** 51(8): 5408-5411.
- Wyckoff, R. W. G. 1964. **Crystal Structures**. 2nd ed. Interscience, New York.
- Yang, Z., T. K. Woo and K. Hermansson. 2004. Strong and weak adsorption of CO on CeO₂ surfaces from first principles calculations. **Chem. Phys. Lett.** 396(4-6): 384-392.
- _____, _____, M. Baudin and K. Hermansson. 2004. Atomic and electronic structure of unreduced and reduced CeO₂ surfaces. A first-principles study. **J. Chem. Phys.** 120(16): 7741-7749.

Zecchina, A., F. Geobaldo, G. Spoto, S. Bordiga, G. Ricchiardi, R. Buzzoni and G. Petrini. 1996. FTIR investigation of the formation of neutral and ionic hydrogen-bonded complexes by interaction of H-ZSM-5 and H-Mordenite with CH₃CN and H₂O: Comparison with the H-NAFION superacidic system. **J. Phys. Chem.** 100(41): 16584-16599.

_____, S. Bordiga, G. Spoto, D. Scarano, G. Spano and F. Geobaldi. 1996. IR spectroscopy of neutral and ionic hydrogen-bonded complexes formed upon interaction of CH₃OH, C₂H₅OH, (CH₃)₂O, (C₂H₅)₂O and C₄H₈O with H-Y, H-ZSM-5 and H-mordenite: comparison with analogous adducts formed on the H-Nafion superacidic membrane. **J. Chem. Soc. Faraday Trans.** 92(23): 4863.

Zygmunt, S. A., L. A. Curtiss, L. E. Iton and M. K. Erhardt. 1996. Computational studies of water adsorption in the zeolite H-ZSM-5. **J. Phys. Chem.** 100(16): 6663-6671.

CURRICULUM VITAE

NAME : Mr. Somkiat Nokbin

BIRTH DATE : October 31, 1975

BIRTH PLACE : Nonthaburi, Thailand

NATIONALITY : Thai

EDUCATION :

1994 - 1998 Kasetsart University B.Sc. (Physics)

SCHOLARSHIPS :

1994 – 2000 The Development and Promotion of Science and Technology Talents Project (DPST) Scholarship, Thailand

2000 – 2005 The Royal Golden Jubilee Ph.D. Program, The Thailand Research Fund, Thailand

2002 – 2003 The Swedish Foundation for International Cooperation in Research and Higher Education (STINT), Sweden

RESEARCH STAY ABROAD

September 15, 2002 Theoretical Inorganic Chemistry,
to Department of Materials Chemistry
August 31, 2004 The Ångström laboratory, Uppsala University,
SWEDEN

April 4, 2005 Theoretical Inorganic Chemistry,
to Department of Materials Chemistry
June 28, 2005 The Ångström laboratory, Uppsala University,
SWEDEN

PUBLICATIONS :

- Nokbin, S.; Limtrakul, J.; Hermansson, K. *Structural and Electronic properties of Rh/CeO₂(110) and Rh/CeO₂(111) : periodic density functional study*. in preparation.
- Nokbin, S.; Limtrakul, J.; Hermansson, K. *Structural and Electronic properties of Rh/MgO(001) : periodic density functional study*. in preparation.
- Nokbin, S.; Limtrakul, J.; Hermansson, K. *DFT plane-wave calculations of the Rh/MgO(0 0 1) interface*. Surface Science (2004), 566–568, 977–982.
- Limtrakul, J.; Nokbin, S.; Chuichay, P.; Khongpracha, P.; Jungsuttiwong, S.; Truong, T. N. *Coverage effects on adsorption of water in faujasite: an ab initio cluster and embedded cluster study*. Studies in Surface Science and Catalysis (2001), 135 (Zeolites and Mesoporous Materials at the Dawn of the 21st Century), 2469-2476.
- Limtrakul, J.; Chuichay, P.; Nokbin, S. *Effect of high coverages on proton transfer in the zeolite/water system*. Journal of Molecular Structure (2001), 560(1-3), 169-177.

CONFERENCES / WORK SHOPS (oral and poster)

- Somkiat Nokbin, Kersti Hermansson and Jumras Limtrakul, “*The interactions of rhodium on (110) and (111) surfaces of ceria: DFT periodic calculation*”, in the Proceeding of 31st Congress on Science and Technology of Thailand, Technopolis, Suranaree University of Technology, Nakhon Ratchasima, Thailand, October 18-20, 2005. (Oral presentation).
- Somkiat Nokbin, Jumras Limtrakul and Kersti Hermansson, “*Structural and electronic properties of the Rh/MgO(001) interface from periodic density functional calculations*”, Abstracts of Papers, the 229th ACS National Meeting, in San Diego, CA, March 13-17, 2005. (Poster presentation).
- Somkiat Nokbin and Kersti Hermansson, “*Structure and electronic properties of Rh/MgO(001): DFT periodic plane-wave calculations*”, Research and Training Network “Surface Active Sites and Emission Control Analysis”, Otto von Guericke University, Magdeburg, Germany, May 12-14, 2004. (Oral presentation).
- Somkiat Nokbin and Kersti Hermansson, “*DFT plane-wave calculations of the Rh/MgO(001) interface*”, Future Trends in Modelling of Nanostructured Materials Systems, Rama Garden Hotel, Bangkok, Thailand, November 9-11, 2003. (Oral presentation).
- Somkiat Nokbin and Kersti Hermansson, “*Bonding and structure in the Rh/MgO(001) interface from DFT plane-wave calculations*”, in the Proceeding of 22nd European Conference on Surface Science, Praha, Czech Republic, September 7-12, 2003. (Poster presentation).
- Somkiat Nokbin and Kersti Hermansson, “*Periodic DFT calculations of Rh/MgO(001)*”, in the Workshop on Application of Density-Functional Theory in Condensed-Matter Physics, Surface Physics, Chemistry, Engineering, and Biology, Fritz-Haber-Institut der Max-Planck-Gesellschaft, Berlin, Germany, July 21-30, 2003. (Poster presentation).

- Somkiat Nokbin and Jumras Limtrakul, “*Coadsorption of Methanol and Ammonia in Faujasitic Petrochemical Catalysts: Quantum cluster and Embedded Cluster Approaches*”, in the Proceeding of 28th Congress on Science and Technology of Thailand, Queen Sirikit National Convention Center, Bangkok, Thailand, 2002. (Here I am just a co-author on the written contribution, since I had already left for my stay in Sweden when the conference took place).
- Somkiat Nokbin, Thanh N. Truong and Jumras Limtrakul, “*Methanol adsorption on faujasitic petrochemical catalysts: an electronic embedded cluster study*”. Abstracts of Papers, the 223rd ACS National Meeting, Orlando, FL, United States, April 7-11, 2002. (I prepared the poster, but I did not go to the conference)
- Somkiat Nokbin and Jumras Limtrakul, “*High loadings of CH₃OH on Faujasitic Petrochemical Catalysts: An Electronic Embedded Cluster Study*”, in the Proceeding of 27th Congress on Science and Technology of Thailand, Lee Gardens Plaza Hotel, Songkla, Thailand, 2001. (Oral presentation).
- Somkiat Nokbin and Jumras Limtrakul, “*Adsorption process of water cluster on Faujasite catalyst*”, in the Proceeding of 26th Congress on Science and Technology of Thailand, Queen Sirikit National Convention Center, Bangkok, Thailand, 2000. (Poster presentation).
- Jumras Limtrakul, Parawan Chuichay and Somkiat Nokbin, “*Effect of high coverages on proton transfer dynamics on the zeolite/water system*”, in the Proceeding of 25th Congress on Science and Technology of Thailand, Amar inlagoon Hotel, Pissanulok, Thailand, 20-22 Oct, 1999. (Poster presentation).